Design and Implementation of Out-of-Plane Thermal Actuators

Shiquan Yao

A Thesis

In

The department of Electrical and Computer Engineering

Presented in Partial Fulfillment of the Requirements

for the Degree of Master of Applied Science at

Concordia University

Montreal, Quebec, Canada

March 2004

Your file Votre référence
ISBN: 0-612-91148-9
Our file Notre référence
ISBN: 0-612-91148-9

ABSTRACT

Design and Implementation of Out-of-Plane Thermal Actuators

Shiquan Yao

The goal of this research is mainly to study the feasibility of using thermal expansion buckle up effect of a microbridge structure to develop a vertical motion, large-force, large-displacement electrical thermal actuator device for micro systems application. Initial results on a prototype system are described in this thesis. The focus of this investigation is to understand the physical properties and performance of an out-of plane deflection microactuator, to develop a preliminary device, and to test the performance of the device including displacement and frequency response.

Five sets of devices with different structural design were fabricated and tested. The functions of devices were characterized both in vacuum and in air ambient. SEM was used to conduct accurate measurement. A device with total length of 500μm, and beams with width of 20 μm ,demonstrated 15.6 μm vertical displacement in vacuum ambient when 3.5 mA input current (4.1V voltage) applied. The observed operational frequency of the devices was less than 103 Hz. A successful application of stiction avoid structure is also documented in this report. It is demonstrated that a 792μm * 20μm double clamped single layer polysillicon beam was successfully fabricated and released without suffering stick down problem.

The physical properties of these micro actuators are modeled. The temperature distribution throughout the structure, the values and the point of maximum temperature are calculated and reported in this thesis. The devices were fabricated using MUMPS technology supported by CMC, following by a post-processing technique.

ACKNOWLEDGMENTS

Most of all, I would like to express my great gratitude to my research advisor Professor Mojtaba Kahrizi, for his support and guidance over the past two years. His high expectation and enlightening advice have helped me stay motivated, and made this thesis possible. I am also grateful to the professor Ion Stiharu and professor Victor Rossokhaty for interesting discussions and their time and help.

I would like to thank, Canadian Microelectronic Cooperation, Natural Science of Engineering Research Council of Canada & Faulty of Electrical and Computer Science Engineering at Concordia University to support this project.

Learning together with other members in Microelectrical Laboratory has greatly enriched my education and life. I would like to thank all of them for their supports and encouragement: Xiaohong Mu, Jun li, Yu fan, Yanxia Zhang, Bowei Zhang, Hong Qu, Lijun Zhang, Zhao Lu, Liwei Sun, and Jun Chan. They have given me many suggestions and made the task of research enjoyable.

Finally, but most importantly, I would like to thank my wife Xin li, my parents, for their great encouragement and supports.

TABLE OF CONTENTS

LIST OF FIGURES

LIST OF TABLES

THESIS OVERVIEW

The definition and a brief history of MEMS are given in Chapter 1. This chapter also covers some application of MEMS, following by a discussion on the basic fabrication techniques and their limitations. Different kinds of MEMS actuators are also discussed in this chapter. The layout design and the operational principle of the different kind of actuator are described in Chapter 2. An important design consideration to avoid stiction is discussed. Multi Users MEMS Process (MUMPs) is also highlighted in Chapter 2. Chapter 3 covers the analytical model of the temperature distribution and the thermal elastic displacement for the double clamped microbridge actuators. Thermal constant, which is used to analysis the devices thermal transient response is discussed also. In Chapter 4, experimental results including experimental setup are given. The experimental and analytical results are compared and discussed. The conclusion and the key findings are highlighted in chapter 5, recommendations for the future work in this area are presented.

CHAPTER 1 INTRODUCTION

This chapter we first give definition and a briefly history of MEMS. Then the basic fabrication techniques and their limitations, which are constrains for design and analysis are discussed, followed by a discussion of two main applications of MEMS devices. After these, a review of silicon micromirror is reported. Then different MEMS actuators are explains and compared.

1.1 Literature Review

The great success of microelectronics technology causes a revolution of miniaturization in many areas, which is the background of micro/nano technology. Functional micro/nano structures, on one hand, can be obtained by self-assembling of atomics and molecular, or on the other hand, by precise micromachining. The former gives rise to interdisciplinaries such as nano biology and nono chemistry, etc., while the latter, causes a revolution in the fabrication of mini mechanical structures and brings up Microelectromechanical System(MEMS).

By the end of the 1960's the invention of the transistor had completely revolutionized the microelectronics industry, allowing for circuits that were much smaller than any of its predecessors [1]. In addition, allowing for circuits that were much smaller than any of its predecessors. The creation of integrated circuits(IC) allowed for a greater number of components to be squeezed in to the same amount of space. Large scale integration (LSI) soon become one of the hottest tops of the 1970's and continued to dominate throughout the 1980's with the invention of very large scale integration (VLSI) designs. Today, designers talk about ultra-large scale integration (ULSI) which has led to microelectronic circuits that are over a million

times smaller and million times faster than those that were available in the early years.[2,3].

By comparison, the history of micromachines has progressed at a much slower pace. In 1965, H.C Nathanson and R.A. Wichstrom first reported the creation of a resonant gate transistor(RGT) using the same lithographic techniques used to create integrated circuits, with gold acting as the structural material and another metal acting as the sacrificial spacer material [4]. The advantage of the RGT was that it used electrostatic force to vary the distance between the gate electrode and substrate, thus allowing the quality factor, Q, of the circuit to be tuned dynamically. Still, despite the appeal of such an element, the RGT never gained much acceptance and was generally regarded as little more than a mechanical curiously [5].

In 1970's a new technique for fabricating micromachines was developed. Instead of depositing additional layer of material using photolithography –a key technique for surface-micromaching processes, anisotropy etching was used to selectively remove material already present on the wafer[6] Since this resulted in devices that were much taller than those produced by surface-micromachining alone, this new technique became essential for bulk-micromachining processes and enabled the creation of a number of other micromechianical devices. For example, thin silicon membranes were developed for use as pressure transducers in a variety of medical and industrial application[7-9]. In addition, microscopic arrays of closely –packed holes were transformed into ink jet nozzles, a technology that is still in use today [10,11]. Aside from these examples, bulk-micromaching techniques were also applied to other devices, such as field emitter arrays, electromechanical switches, and early versions of the integrated accelerometer [12]. Anisotropic etching also proved useful in creating precise V-grooves for the alignment of microscopic optical benches [13,14]

The first impressive review of the applications of silicon as mechanical material, more than electronic material, was published by Kurt Petersen in 1982 [15]. Almost at the same time, Howe [16] first proved the evolution of a very useful method to build micromechanical elements using technologies that were developed first to build microelectronic devices for the integrated circuits in the work done in 1982. R. T. Howe demonstrated techniques to fabricate microbeams from polycrystalline silicon (polysilicon) films [16]. With the encouragement of this demonstration, Howe built the first prototype polysilicon MEMS, a chemical vapor sensor which was a fully integrated micromechanical and microelectronic system [17]. With the development of the micromachining techniques, many complex devices have been produced and some of them are already commercialized. An impressive example of a commercial MEMS that makes use of surface micromachining to build a fully integrated accelerometer is the AD-XL50 microaccelerometer produced by Analog Devices Inc. for use in automobile airbag deployment systems [18].

The impact of MEMS is very wide and deep. The feasibility of MEMS has been proven in the automotive industry. Beside this, MEMS technology has also received the attention of the many of others industry because of its advantages such as low cost, higher performance, reduced size and weight, and increased reliability.

1.2 Micro-machining Techniques

The well-established integrated circuit (IC) industry played an important role in fostering an environment suitable for the development and growth of micromachining technologies. Many tools and processes used in the design and micromachining of MEMS products are borrowed from the IC technology. Not surprisingly, the types of material properties and shapes required for circuitry differ than those for mechanical

structures. Bulk and surface micromachining are two basic and major micromachining techniques.

1.2.1 Surface Micromachining

Surface micro machining is the term used to describe the broad category of fabrication processes that are similar to those used to make IC's. This set of processes starts with a silicon (or other material) substrate and adds layers to the substrate. One major characteristic of surface micro machining is the relatively small maximum height of structures. Layers deposited onto a silicon substrate are typically only 1-5 um thick. Thus the aspect ratio (z-axis to x & y axis dimensions) of surface machined devices is relatively small. This results in a severe limitation in the types of structures that can be realized using this technique.

A simple surface micromachined cantilever beam is shown in figure below. Sacrificial layer of oxide is deposited on the surface of the wafer. A layer of polysilicon is then deposited, and patterned using RIE techniques to a beam with an anchor pad (Figure 1.1a). The wafer is then wet etched to remove the oxide layer under the beam, freeing it (Figure 1.1b). The anchor pad has been under etched, however the wafer was removed from the etch bath before all the oxide was removed from under the pad leaving the beam attached to the wafer.

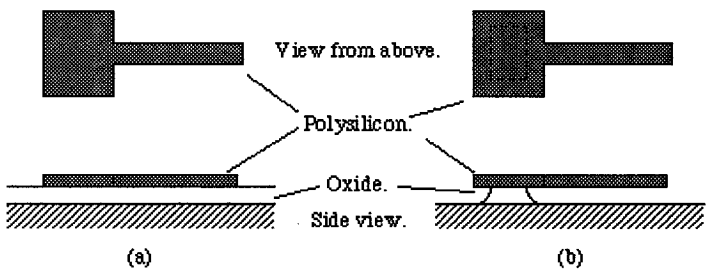

Figure 1.1 Surface micromachining

1.2.2 Bulk Micromachining

Bulk micromachining is a term that refers to another broad category of MEMS fabrication processes. In bulk processes, the silicon substrate is selectively etched away to form structures with relatively large aspect ratios. While tending to enable the fabrication of a larger number of types of structures, bulk micromachining is usually not capable of producing circuit components. Thus a fundamental tradeoff exists between accommodating the electrical and structural needs of a MEMS device. For bulk devices, any electronics are manufactured separately and then integrated to the structure during a subsequent assembly process. Figure 1.2 shows a bulk micromachined pressure sensor. For this device, a cavity is etched into the substrate leaving a thin flexible membrane that deflects under pressure. Deflection is sensed using piezoresistive sense elements located at the edges of the membrane. Surface and bulk micromachining techniques can be combined to gain the benefits of both processes. The design of fabrication processes to best suit the design of various MEMS devices is a topic of considerable research by both academic and industrial organizations.

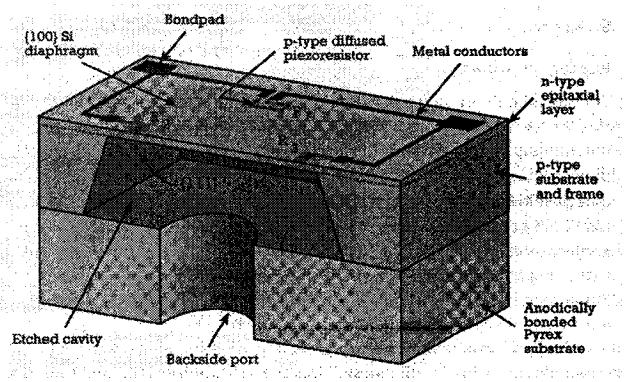

Figure 1.2 Bulk micromachined pressure sensor

1.3 The Applications of MEMS:

The impact of MEMS is very wide and deep. The feasibility of MEMS has been proven in variety industry. In this thesis, we focus on two kinds of important applications of MEMS. They are optic switches and adaptive optics.

1.3.1Optic Switches

The optic switches are used to reconfigure/restore the network, increase its reliability, and /or act as the optical add/drop mutiplexer (OADM). A successful optical switching technology will have to demonstrate superiority in the areas of scalability, serviceability, and long-term reliability. The recent development of free-space optical MEMS technology has shown superior performance for this application. MEMS optical switch not only retained their conventional counterparts advantages of free-space optics such as low losses and low cross talk, but also included additional ones such as small size, small mass, and sub millisecond switching times. Furthermore MEMS fabrication techniques allow integration of micro-optics, micro-actuators, complex micro mechanical structures, and possibly microelectronics structures on the same substrate to realize integrated Microsystems.

1.3.2 2-D and 3-D MEMS Optical Switches

Generally, two approaches are taken in implementing MEMS optical switches.[19] In the two-dimensional or digital approach, an array of micromirrors and the optical fibers are arranged so that the optical plane is parallel to the surface of the silicon substrate. The micromirrors can assume one of two states at any given time.[20] In the cross state, the micromirror moves into the path of the light beam and reflects the light beam, whereas in the bar state, it allows the light beam to pass straight through. Figure 1.3 is a diagram of a simplified two-dimensional 4x4 MEMS optical switch.

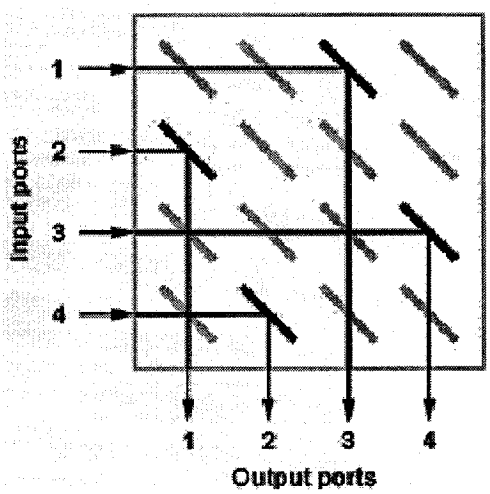

Figure 1.3 A two dimensional 4x4 MEMS optical switch [21]

The short diagonal lines represent micromirrors. The darkened mirrors are in the cross state while the grayed out micromirrors are in the bar state. Input light beams 1, 2, 3 and 4 are directed to output ports 3, 1, 4 and 2 respectively. With individual micromirrors in the cross state or bar state in the array, any input port can be connected to any output port.[21]

In the three dimensional or analog approach, the micromirrors are not limited to just two positions. They are able to vary their position over a continuous range of angles and in two directions, which allows a single micromirror to direct an input light beam to more than one possible output port[22] . In contrast, in the two-dimensional approach, the micromirror in row one, column three for example, is able to direct only input light beam 1 to output port 3. According to Hecht [22], a common three-dimensional micromirror is the two-axis tilting micromirror (see Figure 1.4).

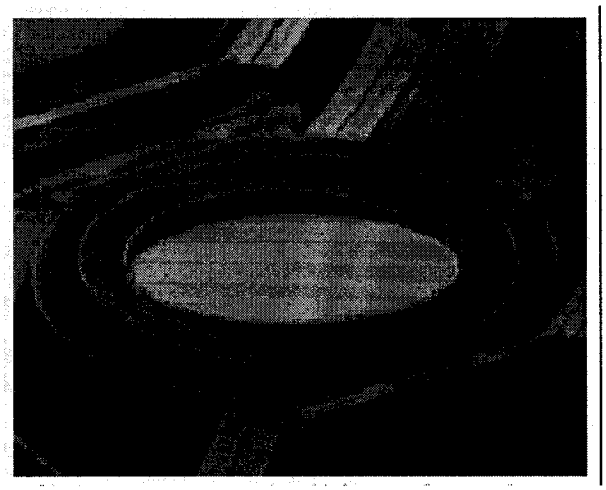

Figure 1.4 Two-axis tilting micromirror [22]

The circular micromirror "pivots on one axis between a pair of posts attached to a surrounding ring. The ring, in turn, pivots on a perpendicular axis on a pair of posts connected to a sur-rounding framework, which is fixed in place above the surface." Figure 1.5 depicts two arrays of these tilting micromirrors, used in an NxN MEMS optical switch. The light beams from an array of input ports fall onto the first array of tilting micromirrors, which reflects

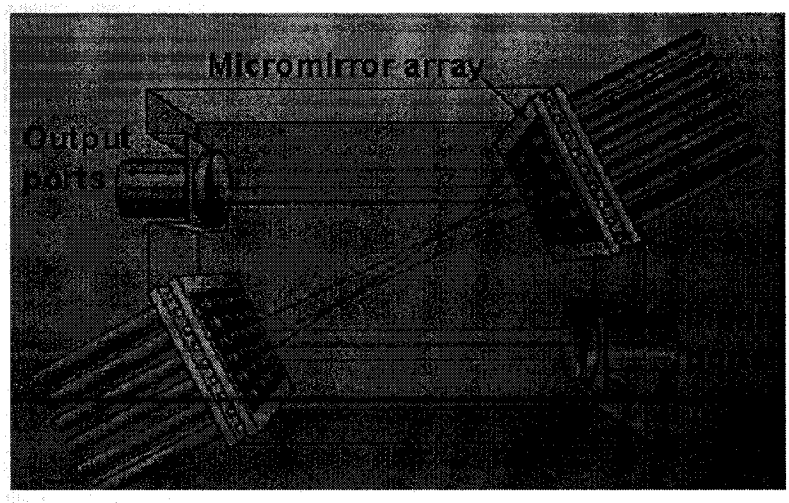

Figure 1.5: Arrays of tilting micromirrors in

action [22]

the light beams onto a second array. The second array then reflects the light beams into an array of output ports. Each micromirror on the first array is able to reach any of the micromirrors on the second array and vice-versa. [22]

For an NxN switch, the two-dimensional approach requires N^2 micromirrors, while the three-dimensional approach requires only 2N micromirrors. The three-dimensional approach scales much better with port count, as it is linear in N. Hence, as port count in-creases, the three-dimensional approach results in more compact designs than the two-dimensional approach. The two-dimensional approach also suffers from an increasing propagation distance for light as port counts grow. When the light beam exits the optical fiber, it begins to spread. The longer the distance traveled, the greater the beam's diameter becomes, resulting in the need for greater collimator (device that makes divergent or convergent rays more nearly parallel) performance. However, the two-dimensional approach has the advantage of being simpler and less sensitive to noise. The micromirrors in the three-dimensional approach have to be very precise. A small amount of noise pre-sent in the control circuit can cause an error in the tilt angle of the micromirror, leading to misdirection to the wrong port. [20]

We look forward to the following parameters in a switch to measure its performance: switching speeds, loses in a switch, and scalability.

There is a performance comparison of some optical switches.

Manufacture	Actuate Mechanism	Switching Time	Insertion loss	Cross talk	More information
Nagaoka, Japan	Electromagnet	0.2 ms	0.36 dB	-70 dB	Cascaded to 1x8 configuration
Hewlett-Packard	Electrothermal	0.77s	5.8dB	-66.5dB	Power > 500mW
Helvetica France	Electrostatic	0.8ms	3-4dB	-30dB	Drive voltage: 55 v
Hitachi, Japan	Electromagnetic	40ms	3.1dB	-40dB	Size 12.4 mm x 13.0 mm

Table 1.1 Performance comparison of some optical switches

1.3.3 Adaptive Optics

MEMS devices have a successful application in Adaptive Optics system also. Adaptive Optics refers to optical systems, which adapt to compensate for optical effects introduced by the medium between the object and its image . Consider a beam of parallel light passing through a vacuum; a slice across this beam will contain some pattern of phases, which will move (uniformly) at the speed of light along the beam. If the beam passes through a uniform medium, its speed is slowed but the pattern of phases still moves together. In a non-uniform medium, however, some parts of the beam are slowed more than others, leading to distortions in the uniform wavefront. [23]

In astronomy, the effects of atmospheric blurring can be avoided by going into space. However, facilities like the Hubble Space Telescope (HST) are extremely costly to build and operate, and despite their expense, space-based telescopes remain relatively small. The figure below shows that the telescope with Adaptive Optics system gives 4- 5 times better resolution than HST.

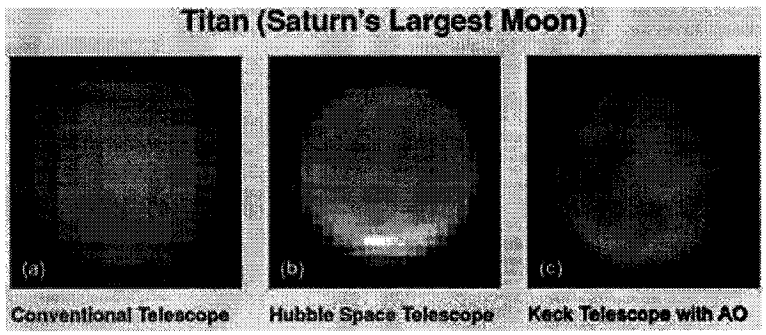

Figure 1.6 Image taken by different kind of telescope.[23]

All AO systems work by determining the shape of the distorted wavefront, and using an "adaptive" optical element -- a deformable mirror -- to restore the uniform wavefront by applying an opposite canceling distortion. Figure1.7 depict the schematic diagram of an Adaptive Optics system. [23]

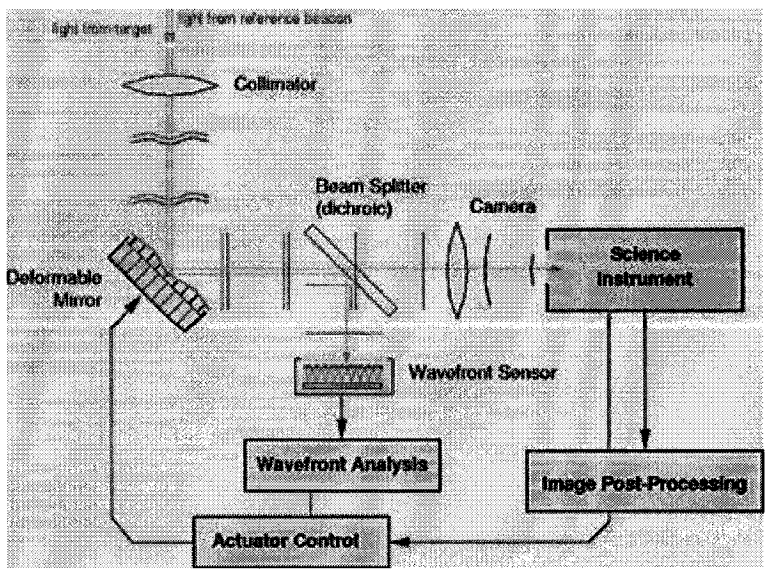

Figure 1.7 Schematic diagram of Adaptive Optics system [23]

The deformable mirror device is a critical component of an adaptive optic system. It is used to apply the correction to the distorted wavefront. In current systems the deformable mirror device is the most expensive component. The recent advent of MEMS technology offers an alternative technology for the construction of cost effective mechanical mirror actuators. The MEMS deformable mirrors have shown the lowest fabrication cost, lowest power consumption, lowest mass, lowest volume, elimination of polarization effects, and lowest non-uniformity of any deformable mirror technology. It offers light weight components, thus making it entirely suitable for ground based, airborne, and even hand held wavefront correction applications.

1.4 Micromirrors

Micromirrors are the centerpieces of many MEMS device for optical purpose. They are tiny mirrors fabricated in silicon using MEMS technology. For an optical switch, the switching function is performed by changing the position of a micromirror to deflect an incoming light beam into the appropriate outgoing optical fiber. Silicon micromirrors can be divided into two categories, depending on the type of motion of the mirror. Mirrors that can move up and down in the vertical direction are called "Piston " Mirrors, whereas mirrors that can rotate along an axis are called "torsion" or "tilt" Mirrors. Piston mirrors are often used to modulate the phase of an incoming beam of light, whereas torsion mirrors are usually used to redirect beam of light. Both types of mirrors have been featured extensively in literature and have found a variety of application industry. The three important properties of micromirrors are reflectivity, light transmission, and surface roughness. [19] [24]

1.5 Actuators

Actuators capable of relatively large linear and angular deflection, consuming less power and easy to fabricate are required for most kind of applications. Research in micro actuators has grown rapidly and several important millstones have been demonstrated, including the successful operations of micro-mirrors[25],electrostatic micro-motors[26] and electrostatic comb resonators[27] . Thermal micro actuators have shown promise for MEMS applications due to their relatively large force and displacement capabilities. It is shown that they can be a valuable complement to electrostatics actuators,[28] which have typically small deflections and require either close dimensional tolerances or high voltages to achieve large deflections.

1.5.1 Comb Drive Actuator

An electrostatic comb drive actuator, consisting of interdigitated capacitors, is one of the most important of MEMS devices. In a typical comb drive, the gap between the fixed and moving fingers is uniform, resulting in an electrostatic driving force that is independent of the position of the moving fingers except at the ends of the range of travel. It is possible, by changing this gap profile, to obtain different force profiles. [29]

$$F_x = \frac{\varepsilon V^2 t}{2g} \qquad (1.2)$$

The deflection is related to the number of fingers on each side of the comb drive, the gap between comb fingers, Young's modulus, folded beam length and beam width, as well as the applied voltage. The displacement as a function of suspension-beam dimensions was calculated for comb drives with a 3- um gap, 150 fingers, and using 175 GPa for Young's modulus [30]. It was found that for suspension beams that

have a width of 3 um and a length of 700um, a driving voltage of 50 V is needed to achieve 50- um displacement.

The designs for linear comb drive actuators shows limited forward displacement due to eletromechnaical side instability. In addition to longitudinal force that moves along comb finger direction, there are also lateral forces between adjacent comb fingers (similar to that of gap closing actuators). Normally, the lateral forces balance out. But at high voltage, the lateral force becomes very large, and with small disturbance, the lateral forces could become unbalanced. The movable comb move laterally and collapse to the fixed comb. Beside this, no linearity in force vs. voltage relationship, and requirement of high driving voltages to compensate for the low force potential are the other shortcoming of comb drive.

1.5.2 Scratch Drive Actuator

Scratch drive actuation is an electrostatic phenomenon that results when a suspended plate with an attached bushing is attracted to a flat plate. The attraction causes snap down and zippering, pushing the bushing forward. When the charge is released, the plates separate, but the bushing remains in position, causing a horizontal displacement. This process can be repeated to generate forward motion.

A full actuation cycle consists of pull-in, zippering, and release. This capability will be demonstrated by considering a polysilicon scratch drive actuator that was developed by researchers at the University of Tokyo. Their findings show that the distances the scratch drives travel in each step are approximately 0.1 μm and depend on the peak voltage, suspended plate length, and bushing height. The advantage of this structure is that it can produce large displacement. But the important shortcomings are high driving voltage and slow moving speed. Experiments which were done by Terunobu Akiyama from University of Tokyo show [31] that the plate

of the SDA is 50μm in length, 70 μm in with and 1.0 μm in thickness. The bushing is 1.5 μm in length, 10μm-30μm in with and 1.0 μm in thickness. A typical velocity of the SDA with buckled beam was 8μm/sec, when the pulse frequency was 50 Hz and the peak voltage was +/_ 140v.

1.5.3 Thermal actuators

Thermal actuation has been extensively employed in MEMS. It includes a broad spectrum of principles such as thermal pneumatic, shape memory alloy (SMA) effect, bimetal effect, mechanical thermal expansion, etc.[32]

The thermal pneumatic microactuator uses thermal expansion of a gas or liquid or the phase change between liquid and gas to create the actuation. Shape memory alloy effect occurs in some alloys in which a reversible thermal mechanical transformation of the atomic structure of the metal happens at a certain temperature. At low temperature, the SMA is kept at the desired deformed shape. When the temperature rises above a threshold value, the deformed SMA is transformed back to the original shape.

1.5.3.1Thermal Bimetallic Actuator

A thermal bimetallic microactuator consists of two different materials that are layered together. Figure 1.8 shows a cantilever bimetallic structure. When it is heated, a deflection is generated by the different thermal expansion between the two materials. The more different between the two materials' thermal expansion coeffients, the more deflection is generated.

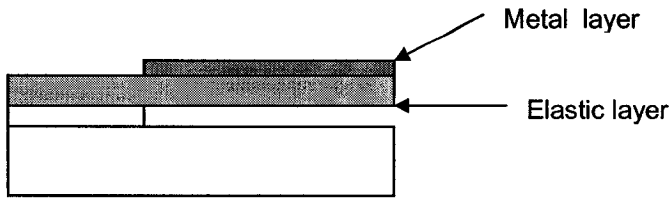

Figure 1.8: The thermal bimetallic microactuator with the cantilever prototype

1.5.3.2 Thermal Expansion Actuator

The principle of the mechanical thermal expansion microactuator is similar to that of the bimetallic microactuator. The only difference is that the mechanical thermal expansion microactuators are made of the same material.

A classic thermal actuator based directly on thermal expansion is shown in the figure below. In this thermal actuator, the hot arm is usually thinner than the cold arm, so the electrical resistance of the hot arm becomes higher than the cold arm. When an electric current passes through the cold and hot arms, the heat generated in the hot arm is much more than that of the cold arm. It causes that the temperature of the hot arm to become much higher than the cold arm. Since the cold and hot arms are made of the same material and same thermal expansion coefficient, the temperature difference causes the hot arm to expand more than the cold arm. This results in the rotation of the actuator.

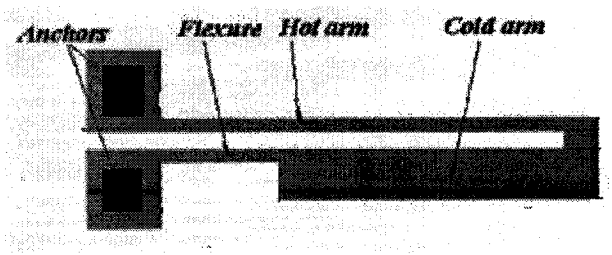

Figure1.9 Schematic top view of thermal flexure actuator.

Thermal actuators can generate relatively large force and displacement at low actuating voltage. The deflection can linearly increase as the control voltage is increased within a large range. Mechanical thermal expansion actuator and bimetallic actuator also can be integrated in a chip easily. In addition, most of thermal micro actuators can be fabricated using conventional integrated circuit (IC) technology and driven by CMOS compatible voltages and currents. [33] However the high power consumption and low switching frequency are concerns for applications of thermal actuators.

In next chapter, the layout design and the operation principle of the five main categories (families) of designs with different mechanical mechanism to realize the out of plane actuation are described. Chapter 3 documents the analytical model of the temperature distribution and the thermal elastic displacement for the microbridge actuator. After this chapter, in Chapter 4, experiments are carried out to evaluate the device performance. The experiment setup as well as the measurement result is reported. Chapter 5 concludes the thesis. The key findings are highlighted and recommendations for the future work in this area are presented.

CHAPTER 2 DESIGN AND FABRICATION

In this chapter the designs implemented using the MUMPs process are described in detail. We first describe the MUMPS process technology. Then we will discuss the design of our devices. We pay particular attention to the actuating system of the device, which is the most essential part. An important design consideration, structure stiction is discussed in this chapter. Two kinds of structure that successfully implemented in tour design to preventing microbridge stiction are also described. Finally, the layout designs and basic actuation mechanism of the devices in each of five families are described in detail. The designs in family A,B,C,D based on a microbridge structure to realize the out-of-plane actuation. Design in family E converts the in-plan deflection generated by V-shape thermal actuator to an out-of-plan displacement

2.1 MUMPs Proscess Technology

The MUMPs process is a three-layer Polysilicon surface micromachining process derived from the work performed at the Berkeley Sensors and Actuators Center (BSAC) at the University of California in the late 80's and early 90's[34].

Figure 2.1 is a cross section of the three-layer Polysilicon surface micromachining PolyMUMPs process. This process has the general features of a standard surface micromachining process: Polysilicon is used as the structural material, deposited oxide (PSG) is used as the sacrificial layer, and silicon nitride is used as an electrical isolation between the Polysilicon and the substrate. The process is different from most customized surface micromachining processes in that it is designed to be as general as possible, and

to be capable of supporting many different designs on a single silicon wafer. Since the process was not optimized with the purpose of fabricating any one specific device, the thicknesses of the structural and sacrificial layers were chosen to suit most users, and the layout design rules were chosen conservatively to guarantee the highest yield possible.

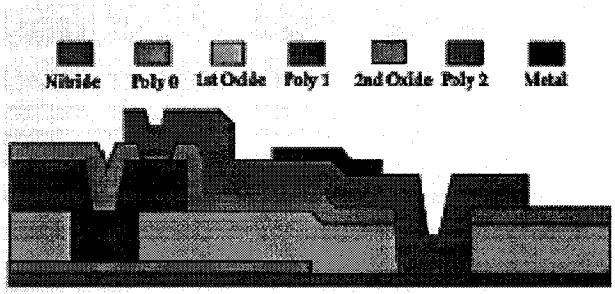

Figure 2.1 Cross sectional view showing all 7 layers of the MUMPs process [34]

Table 2.1 outlines the material layer names, thicknesses and the lithography levels associated with those layers.

Material Layer	Thickness (μm)	Lithography Level Name
Nitride	0.6	--
Poly 0	0.5	POLY0 (HOLE0)
First Oxide	2.0	DIMPLE ANCHOR1
Poly 1	2.0	POLY1 (HOLE1)
Second Oxide	0.75	POLY1_POLY2_VIA ANCHOR2
Poly 2	1.5	POLY2 (HOLE2)
Metal	0.5	METAL (HOLEM)

Table 2.1 Layer names, thickness and lithography levels of MUMPS process.[34]

2.2 The Goal of Design:

The final goal of this project is to use MUMPS process technology to prototype a number of thermal actuators for various applications including optical switches. Actuators capable of relatively large linear and angular deflection and easy to fabricate are required for most kind of applications. To satisfy these requirements, we will design and implement a series of out-of-plan motion thermal actuators in this thesis. The reason why we choice out-of-plane motion is explained in the following part.

The centerpieces of many optical MEMS devices are micrormirrors. They are tiny mirrors fabricated on silicon based devices. For an optical switch, the switching function is performed by changing the position of a micromirror to deflect an incoming light beam into the appropriate outgoing optical fiber. These micromirrors will be formed by Poly1 or Poly2 structure layer in MUPMS process. Since these layers are parallel to the substrate, the only possible motion of the mirror will be up and down. In the MUMPS process description, we can find that the top structure layer, Poly2, has the largest distance from the substrate and is only about 3.25 micrometer. That means if the mirror plane is to move down, the maximum displacement is only 3.25 um before it touches the substrate. Some designs suffer from this limitation [35]. But if we can raise the mirror away from the substrate, there will be more space for motion, then we can realize a high performance optical switch, which might be a 3D optical switch.

2.2.1 Basic Working Principle

To realize the out of plane actuation, we focus on the thermal buckle up phenomenon of a double end clamped beam structure (microbridge). The figure 2.2 shows the basic operation principle.

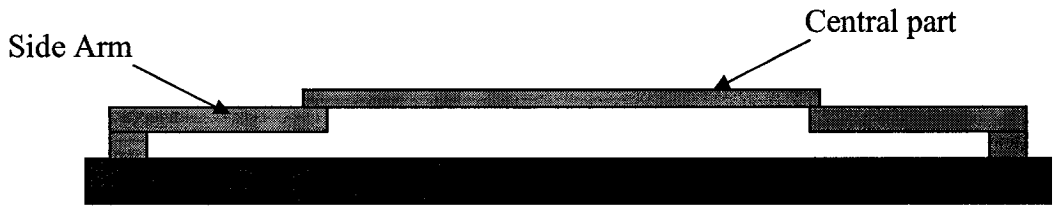

(a)

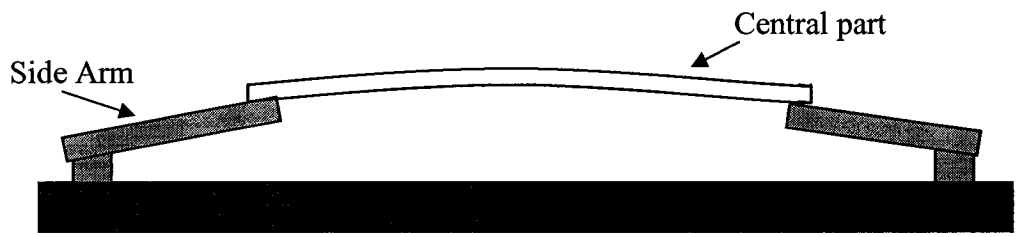

(b)

Figure 2.2 The basic idea of a out-of-plane electrical thermal actuator, (a): microbridge structure before apply voltage. (b): When voltage applied, the thermal expansion caused by joule heating made the bridge structure buckles up

After applying bias at two-fixed end, current through the whole structure will cause joule heating. Seeing that the central part of the bridge is curve up from the side arm, the thermal expansion of the material will induce the whole structure to buckle up from the substrate. Since the bridge is actuated by material thermal expansion, a relative high actuation force and large deflection are supposed to be generated by this structure.

2.2.2 Structure Stiction .

To fabricate a microbridge structure that could buckle up in the operation mode, a important consideration in design is structure stiction. Stiction is a notorious cause of malfunctioning in microdevices. Surface micromachined structures which have been fabricated using the wet sacrificial layer etching technique can be pulled down to the substrate by capillary forces during drying [36], [37] Due to the smoothness of the surfaces in surface micromachining, large adhesion forces between fabricated structures and the substrate are encountered. Once contact is made adhesion forces can be stronger than the restoring elastic forces and even short, thick beams will continue to stick to the substrate.

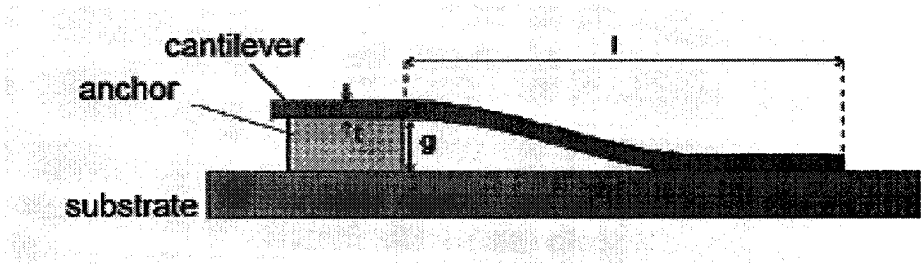

Figure2.3. A cantilever beam stick to the substrate.

Capillary forces are the most important adhesion mechanisms. [38] A thin liquid layer between two solid plates can work as an adhesive. If the contact angle θ_C between liquid and solid is less than 90°C(Figure 2.4), the pressure inside the liquid drop will be lower than outside and a net attractive force between the plates exists.

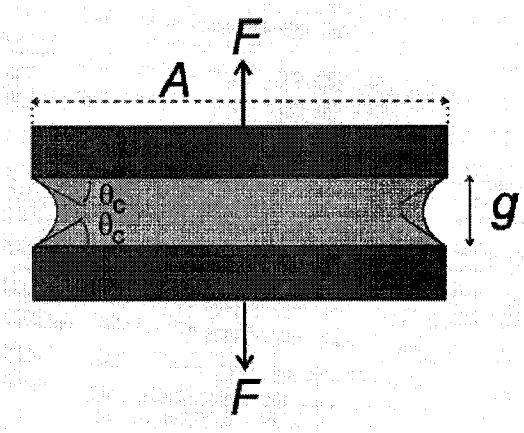

Figure 2.4. A thin layer of liquid working as an adhesive between two plates.

θ_C is the contact angle between liquid and solid in air, g is the liquid layer thickness, and A is the wetted area. A force F is applied to maintain equilibrium. In equilibrium, an external force F separating the plates applied to counterbalance the capillary pressure forces is given by : [38]

$$F = -\Delta p_{la} A = \frac{2A\gamma_{la}\cos\theta_C}{g} \quad (1)$$

where A is the wetted area. where γ_{ta} is the surface tension of the liquid–air interface, g is the gap between substrate and the structure layer, θ_C is contact angle.

In the design of a cantilever beam structure ,the critical length before stick down is (2) [38]

$$l_{crit} = \sqrt[4]{\frac{3}{8}\frac{Et^3g^2}{\gamma_s}}. \quad (2)$$

where γs is the adhesion energy per unit area ,t is the thickness of the structure layer, E is

the Yong's modulus . If we neglect the residual stress and the stiffening due to stretching then equation (2) also could be used for the critical length estimation of doubly clamped beams . Only the numerical constant in (2) should be changed, yielding a critical length of doubly clamped beams that is about 2.9 times larger than the critical length of cantilevers [39].

Assuming an adhesion energy γs 100 mJ m^{-2}, we can evaluate the critical length of cantilever and doubly clamped beams. Figure 5 shows the length of the beams that are just kept down to the substrate, as a function of beam thickness, for three different gap spacings, according to equation (2).

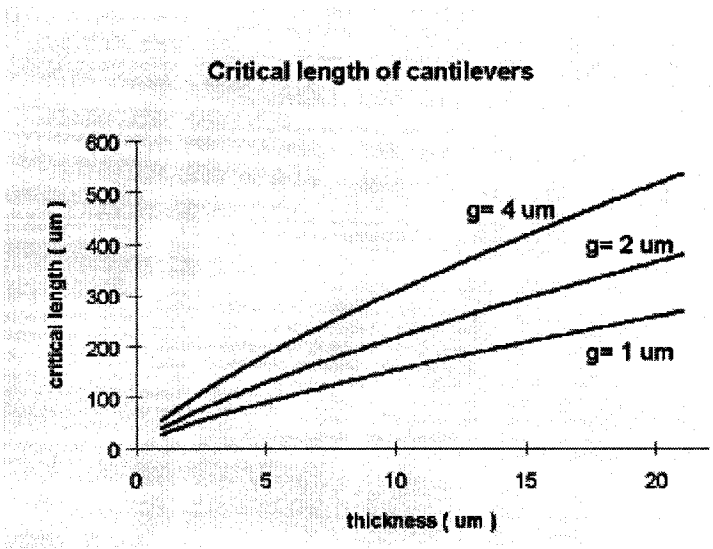

(a)

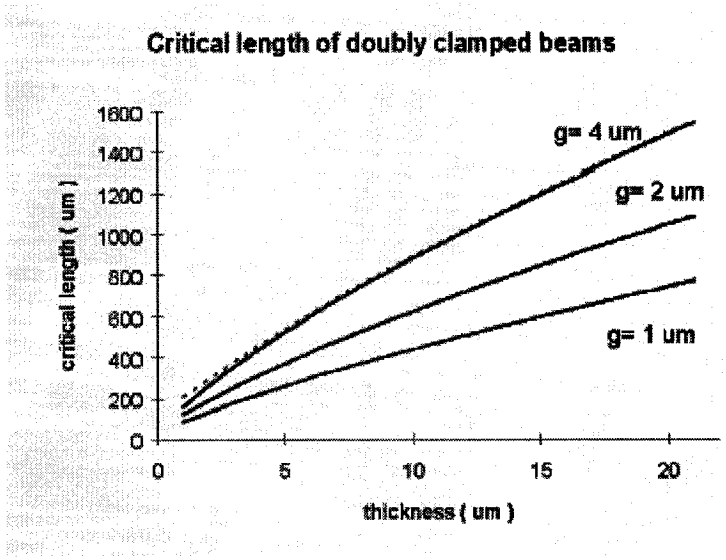

(b)

Figure 2.5.(a) Critical length of cantilever beam as a function of beam thickness

(b)Critical lengths doubly of clamped beams as a function of beam thickness[38]

When it comes to MUMPS process technology, the critical length of each structure layer is listed in the table below.

Structure Layer	Thickness (μm)	Gap (μm)	Cantilever Beam(μm)	Double Clamped Beam(μm)
Poly1	2	2.5	129.5	375.6
Poly2	1.5	3.25	118.9	345.1

Table 2.2 Critical length of Poly1 and Poly2 beam

Unless very thick or short structures and large gap spacing is used, it is not possible to avoid contact during drying by increasing the elastic deformation energy. Structures that stick can sometimes be released mechanically or by generating a repulsive force between the structures [40]. However, these methods do not seem to be suitable for batch processing.

2.2.3 Avoid Stiction

In general, there are two approaches to avoid stiction during the drying process. First one is improving process technology. Theoretical calculations show that the critical length of released structures is proportional to $\gamma_s^{1/4}$ (γ_s is the surface tension of the air/liquid interface). This suggests that to fabricate freestanding microstructures, the air/liquid interface has to be completely eliminated during the final release. In Polysilicon micromachining, a common approach to avoid the air/liquid interface is the use of supercritical CO_2 drying. It is a process begins with rinsing the sample in de-ionized water. Then the de-ionized water is replaced by methanol prior to the drying process. At last, methanol is displaced by liquid CO_2 . CMC has implemented this technology into the MUMPS process, but the result is still not very perfect. The reasons are still under study.

Another way to avoid stiction is to design a support structures to prevent structure layer from touching down to the substrate. The support structure is a piece of polysilicon placed under the main structure. There are two kinds of support implement in our designs. One is permanent support the other is temporary support. Figure 2.6 shows the SEM picture of these support structure. Permanent support is placed underneath the structure layer and will not be removed after releasing. Temporary support is more like a sacrificial layer. It will be removed after releasing. Beside avoid main structure touching down to the substrate, these support will also help to form the shape of the microbridge, which is above them.

In our design, both temporary or permanent support structures are employed. They are working very well. In second design, a 792μm *20μm double clamped structure has

been fabricated and released successfully without suffering from stiction problem. This structure is much more longer than the calculated critical length of 345 μm for the conventional double clamped beam.

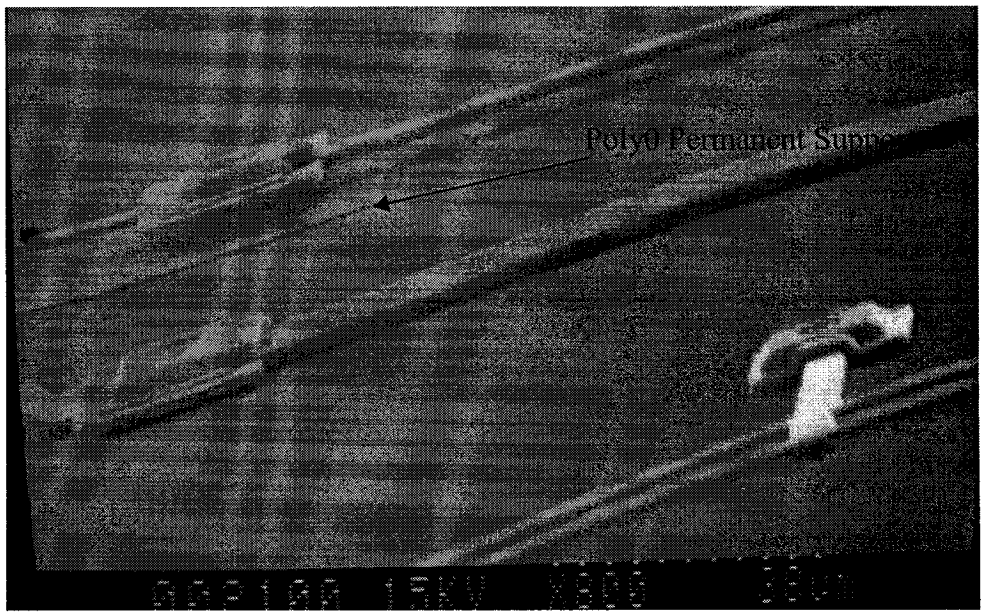

(a)

(b)

Figure2. 6 (a) The Poly0 permanent support helps structure layer lift up from the substrate. (b) The Poly1 temporary support is a sacrificial layer, it will be remove after release.

2.3 Design Implementation:

The first design of thermal actuators (family A) was submitted for fabrication on February 12 2003 for 0301MU MUMPs run provided by CMC (Canadian Microelectronics Corporation) . After some improvement, and optimization, the second design (Family B, C,D,E) was sent out to CMC for 0302 MU MUMPS run on 9 Jul 2003. All together we received 15 dies. And there were 37 devices in each die. We divide these devices into five families based on different fabrication batch and structural design. They are family A,B,C,D,E. In the following section the detail of various designs is given.

2.3.1 The First Batch: (Family A Device)

Two devices were fabricated in the first MUMPs run. The Figure 2.7 shows the schematic diagram and the device's picture of device A2 taken by the optical microscope. This design is an electrothemal actuated optical switch, we try to use microbridge to lift up a mirror plane. The bridge structure is composed of a central beam, two side arms and two rectangular connections. The micro mirror is connected to the bridge structure by a central cantilever arm. The other end of the central cantilever arm is fixed to the substrate. The central beam is made of Poly2, with width of 10 μm, length of 320μm. The four side arms are made of Poly1 with 10 μm wide and 268 μm long. There are one Poly1 square and one layer of Poly0 underneath the central beam. These layers of Poly0 and Poly1 act as a permanent support. These layers influencing the topography and residual stresses of the upper layer in such a way that after joule heating the central part

of the microbridge structure will tend to expand to the upward direction rather than to the downward direction.

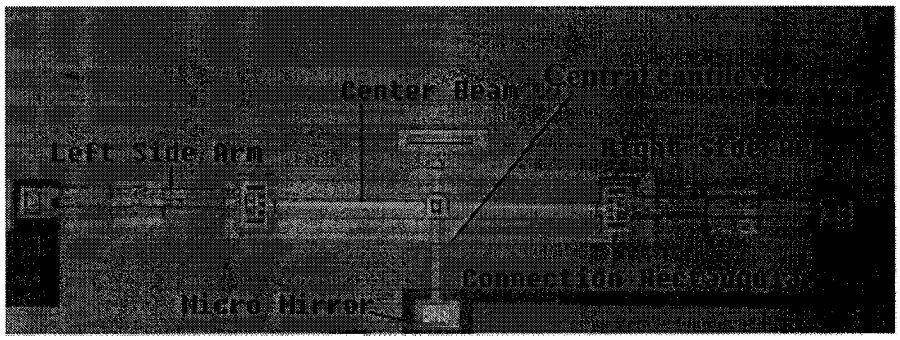

(a)

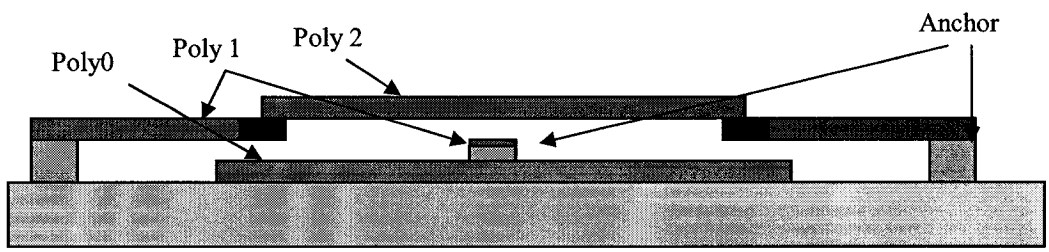

(b)

Figure 2.7 (a) Picture of device A2 taken under microscope (b) Schematic diagram of the device A2.

Another device with short central beam is fabricated to study the geometrical effect on the device performance. Table below gives the geometrical data of the devices in family A.

Device	Total length(μm)	Central Beam(μm)	Central Cantilever Arm(μm)	Side Arm (μm)
Device A1	737	130 *10	48 *8	268 *10
Device A2	737	320 *10	48 *8	173 *10

Table 2.3 The geometrical data of the devices in family A

After testing, we find that the first design suffers from the complex structure design. The large area of the rectangular connection makes this part hard to release. The yield of this design is less 40%.

2.3.2 The Second Batch (Family B,C,D,E)

In the second batch we fixed the problems that we experienced with the device fabricated in the first batch. The structures were modified by reducing or eliminating the connection between Poly1 and poly2. In some devices, instead of a bridge structure composted by Poly1 and Poly2 layer, a simple microbridge structure formed by single poly2 layer is realized. No connection structure involves in these devices. Benefit form this design, the yield of 100% is achieved for the devices in family B. We have four main categories (family) of designs with different mechanical mechanism to realize the out of plane actuation in the second design. Each family has 2 to 7 devices with various designs. The designs in family B,C,D, utilize a microbridge structure to realize the out-of-plane actuation. Design in family E converts the in-plan deflection generated by V-shape thermal actuator to an out-of plan displacement.

2.3.2.1 Family B Device

To test the basic mechanical properties of the bridge structure, the designs in Family B are series of basic bridge structures. Different geometry with variety length width is

implemented. Figure 2.8 shows the layout design and SEM picture of device B2. It is a double clamped Poly2 beam that has 500 μm in length 20 μm in width. To avoid stiction both permanent and temporary support are implemented in this design.

A 70 μm by 200 μm Poly0 square is placed under the central part of the beam. In MUMPs process the Poly 0 is always attached to the substrate. After releasing, this Poly0 structure cannot be removed, and will serve as a permanent support for the bridge structure. Above this Poly0 layer, there is a 30 μm by 180 μm Poly1 square. Since there is no anchor or via designed on this Poly1 layer, the Poly1 square connects to neither Poly0 layer nor Poly2 layer. Therefore, it will be removed during the release process. It serves as a sacrificial structure. We call his Poly1 square a temporary support. Both the temporary support layer and permanent support layer in this design helps to form the shape of the bridge at the central part. It makes the central part of the beam higher than the side beam, and ensures the bridge structure will buckle up rather than buckle down after the structure being heated up.

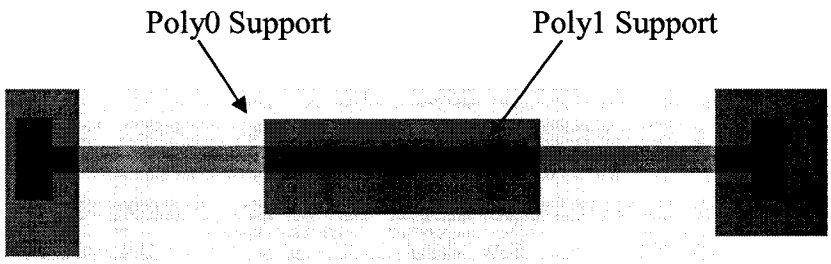

(a)

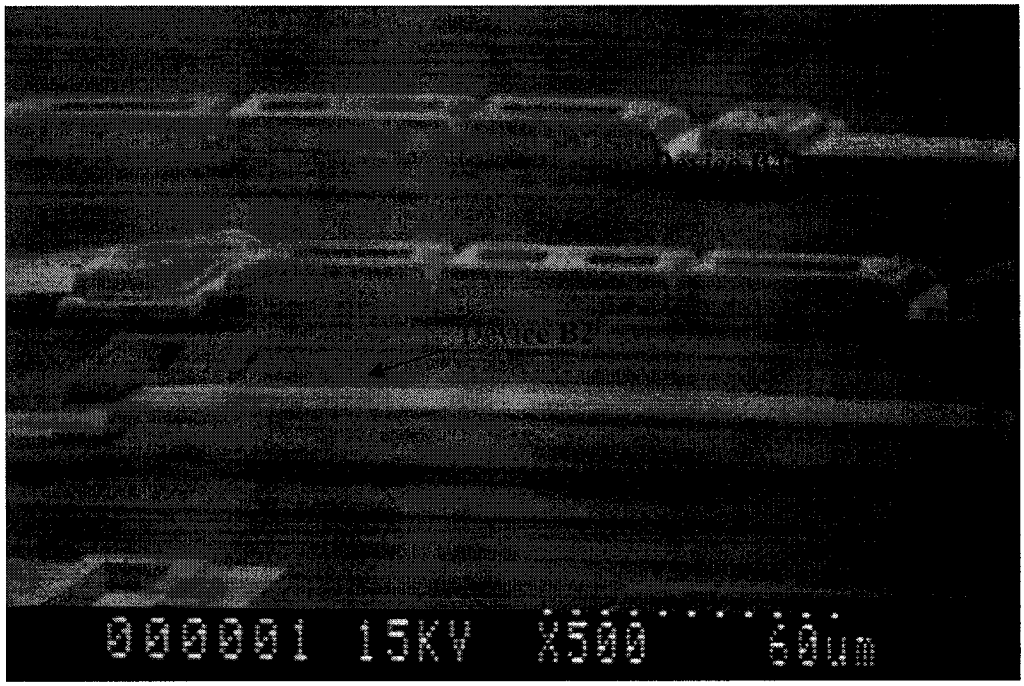

(b)

Figure2.8 (a) layout design of device B2 (b) The SEM picture of B2 and B4.

Some varieties in the structure design are made on other devices in family B. Figure 2.9(a) gives the layout design of device B4. The total length of the device is 792μm. The central part of the microbridge is a 192μm long 20μm wide Poly2 beam. Two 296 μm by 20μm Poly1 side beam is connected to the central beam. Consider that if a whole piece of Poly1 temporary support structure could not be completely removed away from the microbridge, this Poly1 structure would block the movement of the actuator. Therefore, instead of a whole piece of Poly1 square, 3 small pieces of Poly1 are employed as the temporary support in deviceB4. Each of this poly1 square has a dimension about 30μm by 30μm. To help to release the structure, two rectangular etch holes are design at the middle of microbridge structure. The 3D view of B4 generated by MEMES pro is shown in F2.24 b. The SEM image of device B4 can be found in Figure 2.8.

Checking in the SEM picture, we find that a 200μm by 30μm Poly1 temporary support is completely removed from device B2. After inspecting the same device in other 14 dies, we find that this poly1 support structure in 11 dies is completely removed. The rest of them, which does not completely remove from the microbridge is easily moved away by using the probe station. So in the future design, we would consider using a whole piece of Poly 1 for a temporary support structure smaller than 200μm by 30μm instead of breaking them into small pieces.

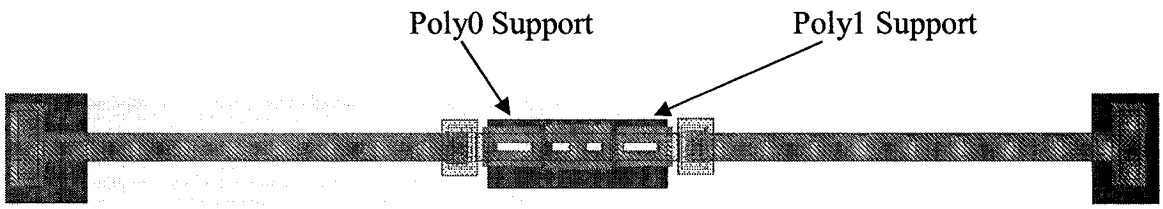

(a)

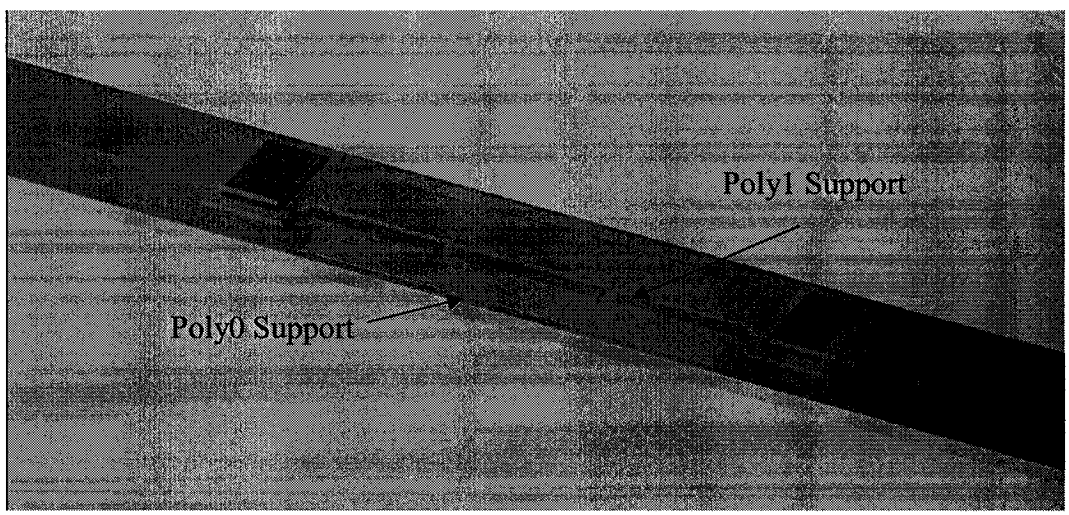

(b)

Figure2.9 (a) layout design of device B4 (b) The 3D view of B4

In device B3 a 25 μm by 25 μm 's micromirror is connected to the middle of the bridge. This micromirror will realize a piston motion which could have an attractive application in Adaptive Optics. A pair of incline anchors is employed in this design. To help to release the structure, two rectangular etch holes are design at the middle of microbridge structure. A 200 μm by 82μm Poly0 permanent support and a 180μm by 45μm Poly1 temporary support are designed under the Poly2 bridge. The SEM picture are shown in the Figure below.

Figure 2.10 The SEM picture of B3

The geometrical data of the devices in family B is list in the table 2.4.

Device	Total length (μm)	Width(μm)	Poly0 Support length(μm)	Poly0 Support Width(μm)	Poly1 Support length(μm)	Poly1 Support Width(μm)
B1	500	10	200	70	180	30
B2	500	30	200	70	180	30
B3	500	20	200	70	180	30
B4	792	20	140	70	120	30

Table 2.4The geometrical data of the devices in family A

2.3.2.2 Family C Device

Devices in family C are some optical switch designs. They originate from the design in family A, but have simpler bridge structure. The cantilever arm with a micromirror is placed at the middle of the bridge. After applying voltage the bridge structure will buckle up because of thermal expansion. And the mirror is lift up. The Figure 2.11 shows the layout design, and the SEM picture of device C4. A 105 μm by 30 μm Poly1 temporary support layer is placed under the central part of the microbridge helping to form the shape of the bridge. For testing purpose some device without mirror plane, device C2 and C3, are fabricated also.

The central cantilever arm in this design has two functions.

1.It connects the micromirror and the bridge structure, and could amplify the vertical displacement of the microbridge. A small upward motion of the microbridge structure will be amplified to a relative large deflection at the end of the arm where the mirror is connected.

2. This beam is also serve as indicator to show the upward force that is generated by the microbridge.

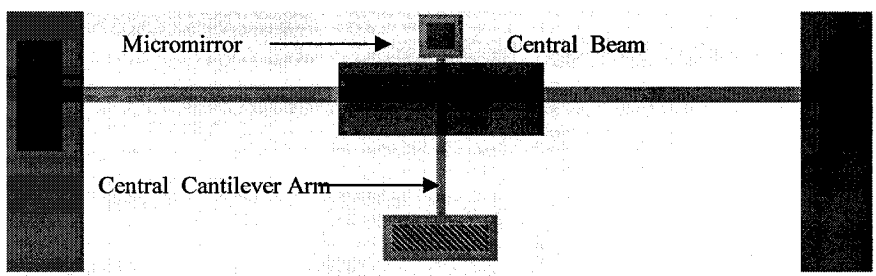

(a)

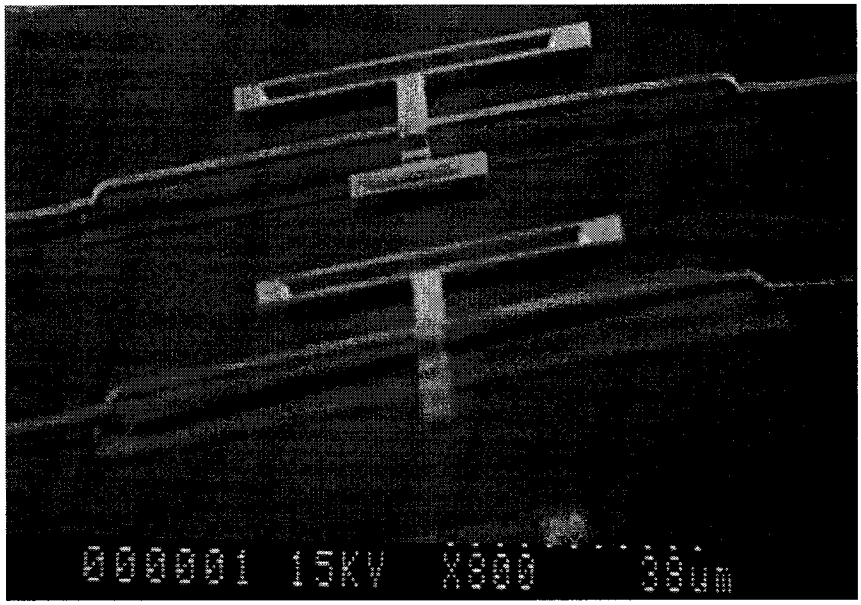

(b)

Figure 2.11 (a) layout design of device C4, (b) The SEM picture of C3,C4

Device C2 and C3 have the similar structure design, but no micromirror is fabricated in these device. Furthermore, the geometry of the microbridge and central cantilever arm is different. Table below list the geometrical data of these devices.

Device	Total Device Length(μm)	Width(μm)	Cantilever Arm Length(μm)	Cantilever Arm Width(μm)	Poly 0 Support Length(μm)	Poly1 Support Length(μm)
C2	300	5	85	5	108	100
C3	400	6	113	5	108	100
C4	400	8	77	5	108	100

Table 2.5The geometrical data of the devices in family C

2.3.2.3 Family D Device

In Family D another kind of lift up mechanism is implemented. We utilize thin-film residual material stress induced structure curvature in our design. The usual practice in MEMS has been to minimize or eliminate residual stresses in thin films. But for our purpose, we view residual stress from the opposite view, as an attractive feature. We deliberately employ differential stresses in two thin films to realize out of plane structure. The metal films are said to be deposited in compression. While the Polysilicon films are deposited in tension. Once the structure is released, the beam length increases slightly, relieving the compression stress so that the free end of the structure will curl up. As a note some other processes have top layer 's film deposited in tension and these films bend down. The residual stress is reduced after the annealing step, but large sheets still show bending due to residual stress. The residual stresses in the MUMPS run can cause about a 4% curl up at the edges of Polysilicon beams. Thus, a beam of 100 μm length will be higher on each end by 4 μm than it is in the center[41].

In family D, a Poly2 central arm covered by metal layer takes the place of the simple Poly2 cantilever arm at the middle of the bridge structure. To achieve more out of plane curvature, the composite central arm has a high ratio of length to width (about 9:1). Compared with the design with conventional central arm, the new design supposes to begin to moving up with lower power input. Because the curled up composite beam will help the bridge structure to raise up, on the contrary the conventional Poly2 cantilever arm will press the structure down when the bridge try to move up.

The curled up central arm would also help the bridge structure to survive from release process. It will lift up the central part of the bridge, and avoid it touching down to the

substrate. In this design the Poly 1 and Poly0 support layers are also engaged to prevent stiction. For testing purpose simple composite central arm without connection to any bridge structure are also fabricated.

Figure 2.12 shows the layout design and SEM picture of the device D1. The composite central beam is a 268 μm by 29 μm Poly2 beam covered by 200 μm by20 μm metal layer. The microbridge structure is 500μm in length and 20 μm in width. The length of Poly0 support is 200 μm, and the length of Poly1 support is 180 μm.

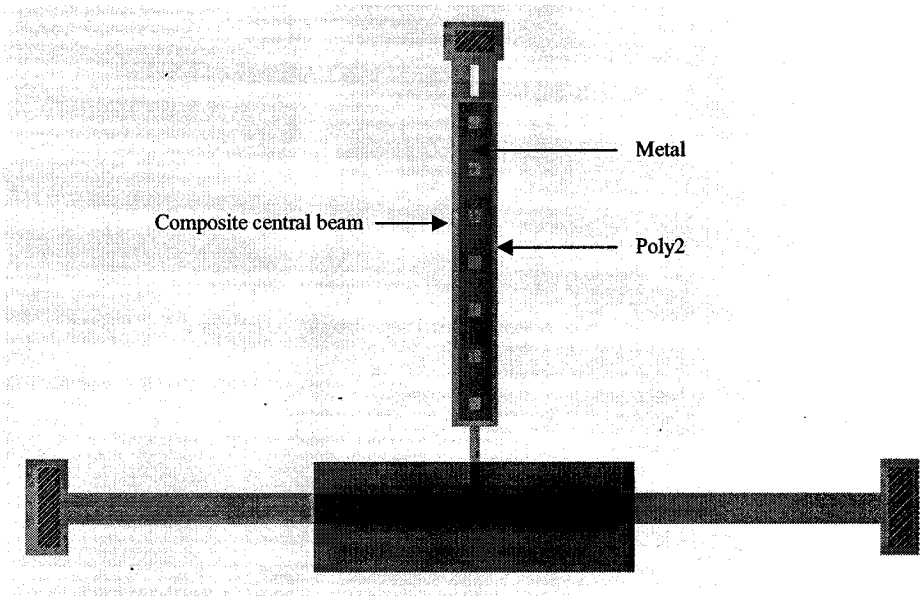

(a)

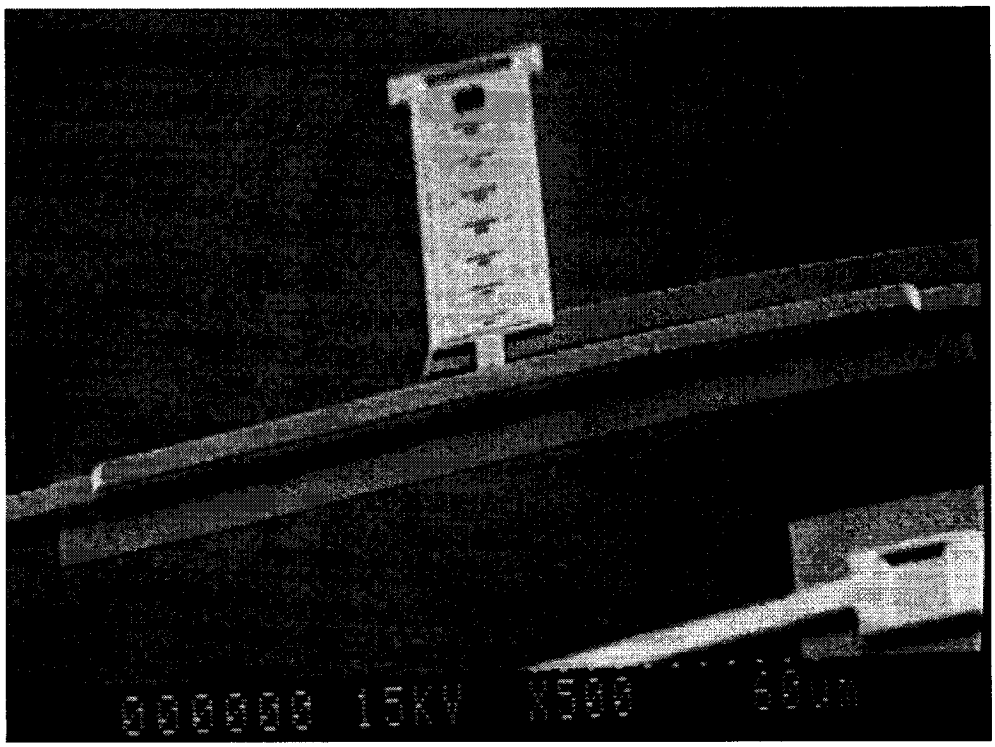

(b)

Figure 2.12 (a) The layout design of device D1 (b) The SEM picture of D1.

2.3.2.4 Family E Device

The designs in family E convert the in-plane displacement to out-of-plane motion .The idea comes from an in-plane motion electrothermal actuator design. [42] .The actuator is a bent-beam suspension (V-shaped structure) that has been studied very successfully for strain sensing. When an electric current passes through a V-shaped beam anchored at it's two ends, thermal expansion caused by joule heating would push the apex outward.

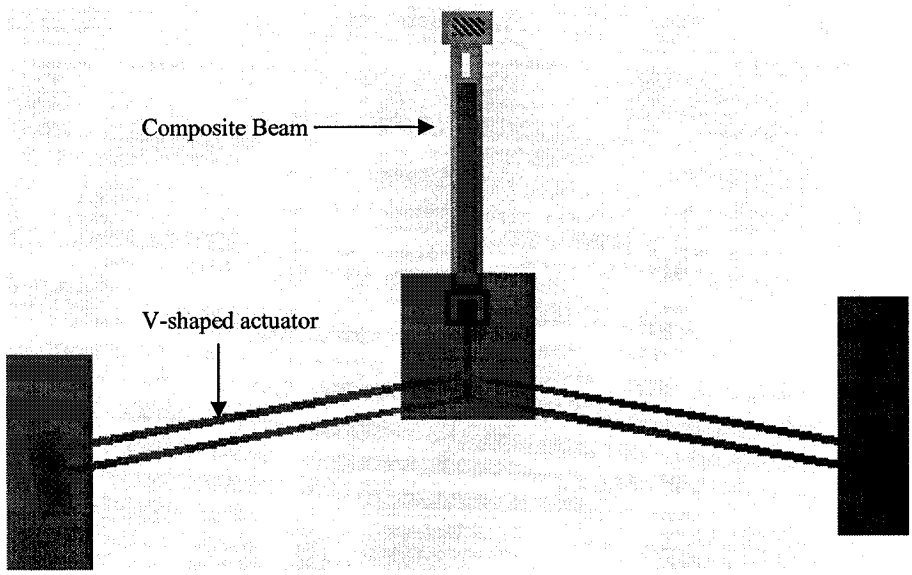

Figure 2.13 layout design of device E3

To achieve out-of-plane motion, we implant the stress induced composite central arm into this design. The composite central arm is a Poly2 cantilever beam covered by metal layer. The free end of the arm is connected to the apex of the V shaped structure. After releasing the residual stresses in films will cause the cantilever beam to bend up. It will lift up the apex of V shaped structure from the substrate. When we apply the voltage to this device, the thermal expansion of the bent-beam structure pushes the apex forward. At the same time the free end of the composite arm will be raised up. It will move up and down with the composite arm. The figure below shows the side view schematic diagram of the device and the its basic operation principle:

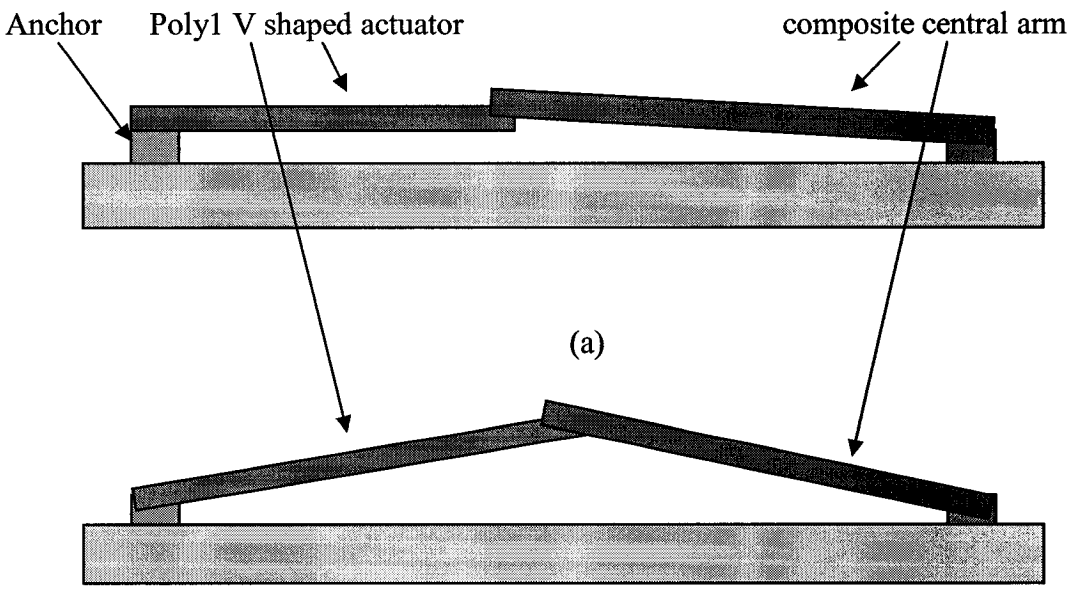

Figure 2.14 schematic diagram of the device E1 (Side view)

(a) No voltage apply to the device E (b) When we apply voltage, thermal expansion of V- shaped actuator will push the composite beam and raise it up from substrate.

In this design, in order to provide enough force to rise up the composite arm, double V shaped structures are utilized. They are parallel to each other. Figure 2.13 shows the layout design of device E1. The composite central beam is a 210 μm by 23 μm Poly2 beam covered by 150 μm by18 μm metal layer. The V-shaped actuator composted by four legs. The dimensions of these legs are 300μm by 4μm. The angle between the legs is 160 °. Poly 0 support structure is used in this design to avoid stiction. Because of the slim legs in the V-shape actuator, stiction problem is serious in this design; even through the poly0 support is employed. The yield of this design is only 50%.

Now the structure design of all the devices in the 5 families that implement in this thesis is outlined. In the following chapter, the analytical modeling of the devices will be discussed in detail.

CHAPTER 3 THEORETICAL MODEL AND ANALYSES

In this chapter, we will discus the device and system modeling. The modeling of the device actuation mechanisms consists of two parts: the electro-thermal response due to the electrical heating [43][44] and the thermal-elastic reaction due to the thermal expansion of the microstructures [45]. To model the thermal transient response, we choose to use electric circuit elements to represent the behavior of devices. Thermal time constant is discussed in this chapter. Implementing the electro-thermal model, the temperature distribution of different devices are calculated and plotted using Matlab software. Geometrical effects are also discussed.

3.1 Thermal Analysis

There are three mechanisms of heat flow: conduction, convection and radiation. According to the finite element analysis, heat dissipation through radiation to air can be neglected in comparison with heat losses through conduction to the anchor substrate. When the heat flow is under steady-state conditions, resistive heating power generated in the element is equal to the heat conduction and convection out of the element.

The heat flow equation is derived by examining a differential element of the microbeam of thickness t, width W, and length dx . [46]

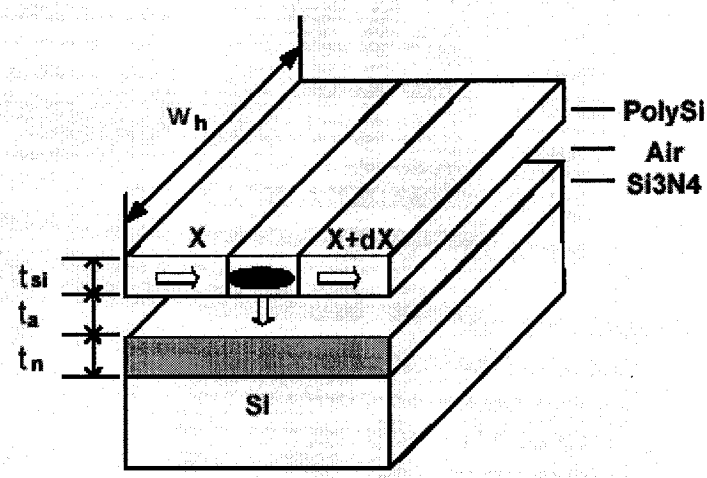

Figure3.1 Diagram of the actuator for the thermal analysis [46]

$$-k_p wt\left[\frac{dT}{dx}\right]_x + J^2 \rho wtdx = -k_p wt\left[\frac{dT}{dx}\right]_{x+dx} + \frac{Sdxw(T-T_s)}{R_T} \qquad (3.1)$$

where T and Ts are the beam and substrate temperatures, respectively; kp is the thermal conductivity of polysilicon, J is the current density, ρ is the resistivity of polysilicon, and S is the shape factor which accounts for the impact of the shape of the element on heat conduction to the substrate . This geometric factor represents the ratio of heat loss from the sides and bottom of the beam to the heat loss from the bottom of the beam only. R_T is the thermal resistance between the polysilicon microbeam and the substrate if the microbeam is wide enough .

The thermal resistance, R_T , is given by:

$$R_T = \frac{t_a}{k_a} + \frac{t_n}{k_n} \qquad (3.2)$$

where t_a and t_n are the thickness of air above the nitride and the thickness of nitride on the substrate, respectively, and k_a and k_n are the thermal conductivity of air and nitride, respectively. The shape factor for heat conduction is given by [46]

$$s = \frac{t_{si}}{w_h}\left(\frac{2t_a}{t_{si}} + 1\right) + 1 \qquad (3.3)$$

where t_{si} is the thickness of the polysilicon and w_h is the width of the arm. Usually, the resistivity ρ is related to the temperature of the polysilicon. The resistivity can be assumed here to have a linear temperature coefficient ξ, so the resistivity becomes a function of temperature

$$\rho(T)= \rho_0[1+ \xi(T-Ts)] \qquad (3.4)$$

where ρ_0 is the resistivity of polysilicon at room temperature. The current density can be written as

$$J= V/\rho L \qquad (3.5)$$

where V is the voltage applied to the actuator, L is the length of the polysilicon that current passes through.

After taking the limit as $dx \rightarrow 0$ in Equation and simplifying the results, the following equation is produced [43]

$$k_p \frac{d^2T}{dx^2} + J^2\rho = \frac{s}{t_{si}} \frac{(T - T_s)}{R_T} \qquad (3.6)$$

The above equation is rewritten as:

$$\frac{d^2 f(x)}{dx^2} - A^2 f(x) = 0 \qquad (3.7)$$

Where

$$f(x) = T(x) - T_\theta \qquad (3.8)$$

$$T_\theta = T_s + \frac{J^2\rho_0}{k_p A^2} \qquad (3.9)$$

$$A^2 = \frac{s}{k_p t_{si} R_T} - \frac{J^2\rho_0\zeta}{k_p} \qquad (3.10)$$

Solving this equation, we get the general solution of the temperature distribution [43]

$$T(x) = T_\theta + C_1 e^{A x} + C_2 e^{-Ax} \tag{3.11}$$

Consider the devices in family A, we separate the whole structure into five segments: two side arms, two rectangular connections and one central beam, as it shows in Figure (3.2) (here we ignore the effect of the cantilever beam at the middle of the micro bridge, which has relatively small volume). Apply this solution to each part of the structure.

Figure 3.2 Schematic diagram of device A2 in design 1

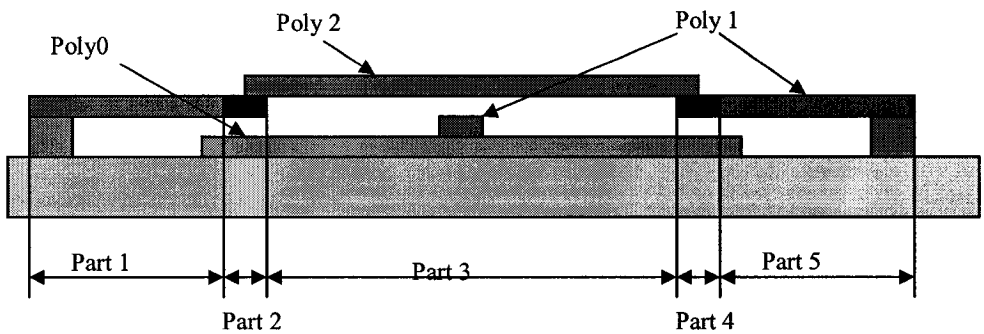

Figure 3.3 Cross-section view of the microbirdge structure in Family A.

In order to get the temperature distribution for each section of the structure, there are ten constants Cj (j =1 to 10) need to be determined. Utilizing the continuity of both the temperature and the rate of heat conduction across the joint point of the central beam, side arms and rectangular connection, we get eight boundary conditions. The other two boundary conditions are taken by assuming the two anchor

pads have the same temperature as the substrate. The following matrix is obtained to solve for the constants.

$$A * C = B \qquad (3.12)$$

$$\mathbf{C}=\begin{bmatrix} c_1 \\ c_2 \\ c_3 \\ c_4 \\ c_5 \\ c_6 \\ c_7 \\ c_8 \\ c_9 \\ c_{10} \end{bmatrix} \qquad \mathbf{B}=\begin{bmatrix} T_s - T_1 \\ T_2 - T_1 \\ 0 \\ T_3 - T_2 \\ 0 \\ T_4 - T_3 \\ 0 \\ T_5 - T_4 \\ 0 \\ T_s - T_5 \end{bmatrix}$$

$$\mathbf{A}=\begin{bmatrix}
1 & 1 & 0 & 0 & 0 & 0 & 0 & 0 & 0 & 0 \\
e^{A_1 L_1} & e^{-A_1 L_1} & -e^{A_2 L_1} & -e^{-A_2 L_1} & 0 & 0 & 0 & 0 & 0 & 0 \\
e^{A_1 L_1} & -e^{-A_1 L_1} & -\lambda_1 e^{A_2 L_1} & \lambda_1 e^{-A_2 L_1} & 0 & 0 & 0 & 0 & 0 & 0 \\
0 & 0 & e^{A_2(L_1+L_2)} & e^{-A_2(L_1+L_2)} & -e^{A_3(L_1+L_2)} & -e^{-A_3(L_1+L_2)} & 0 & 0 & 0 & 0 \\
0 & 0 & e^{A_2(L_1+L_2)} & -e^{-A_2(L_1+L_2)} & -\lambda_2 e^{A_3(L_1+L_2)} & \lambda_2 e^{-A_3(L_1+L_2)} & 0 & 0 & 0 & 0 \\
0 & 0 & 0 & 0 & e^{A_3(L_1+L_2+L_3)} & e^{-A_3(L_1+L_2+L_3)} & -e^{A_4(L_1+L_2+L_3)} & -e^{-A_4(L_1+L_2+L_3)} & 0 & 0 \\
0 & 0 & 0 & 0 & e^{A_3(L_1+L_2+L_3)} & -e^{-A_3(L_1+L_2+L_3)} & -\lambda_3 e^{A_4(L_1+L_2+L_3)} & \lambda_3 e^{-A_4(L_1+L_2+L_3)} & 0 & 0 \\
0 & 0 & 0 & 0 & 0 & 0 & e^{A_4(L_1+2L_2+L_3)} & e^{-A_4(L_1+2L_2+L_3)} & -e^{A_5(L_1+2L_2+L_3)} & -e^{-A_5(L_1+2L_2+L_3)} \\
0 & 0 & 0 & 0 & 0 & 0 & e^{A_4(L_1+2L_2+L_3)} & -e^{-A_4(L_1+2L_2+L_3)} & -\lambda_4 e^{A_5(L_1+2L_2+L_3)} & \lambda_4 e^{-A_5(L_1+2L_2+L_3)} \\
0 & 0 & 0 & 0 & 0 & 0 & 0 & 0 & e^{A_5(2L_1+2L_2+L_3)} & e^{A_5(2L_1+2L_2+L_3)}
\end{bmatrix}$$

Where $\lambda_1 = w_2A_2/2w_1A_1$,

$\lambda_2 = w_3A_3\, h_3 / w_2A_2\, h_2$,

$\lambda_3 = w_4A_4\, h_4 / w_3A_3\, h_3$.

W_n, L_n, H_n are the width, length and thickness of corresponding part n (n=1,2,5). Check in Figurer (3.3). The linear thermal expansion for each section, may be calculated as,

$$\Delta L_n = \alpha \int_0^{L_n} (T_n(x) - T_s)dx = \alpha L_n(\overline{T}_n - T_s) \qquad (3.13)$$

$\overline{T}_n$ stands for the average temperature of part n .They are left side arm ,left connection, central beam ,and right connection, right side beam. They can be expressed as

$$\overline{T}_1 = \overline{T}_5 = T_1 + \frac{c_1}{A_1 L_1}(e^{A_1 L_1} - 1) - \frac{c_2}{A_1 L_1}(e^{-A_1 L_1} - 1) \tag{3.14}$$

$$\overline{T}_2 = \overline{T}_4 = T_2 + \frac{c_3}{A_2 L_2}(e^{A_2(L_1+L_2)} - e^{A_2 L_1}) - \frac{c_4}{A_2 L_2}(e^{-A_2(L_1+L_2)} - e^{-A_2 L_1}) \tag{3.15}$$

$$\overline{T}_3 = T_3 + \frac{c_5}{A_3 L_3}(e^{A_3(L_1+L_2+L_3)} - e^{A_3(L_1+L_2)}) - \frac{c_6}{A_3 L_3}(e^{-A_3(L_1+L_2+L_3)} - e^{-A_3(L_1+L_2)}) \tag{3.16}$$

Figure 3.4 shows the temperature distribution along the location of the actuator with current input from 10.92mA to 13.13 mA . The geometry of the central beams are 10 μm by 132μm, side arms are 10μm by 268μm, and rectangular connections are 35.5μm by 56.5μm.

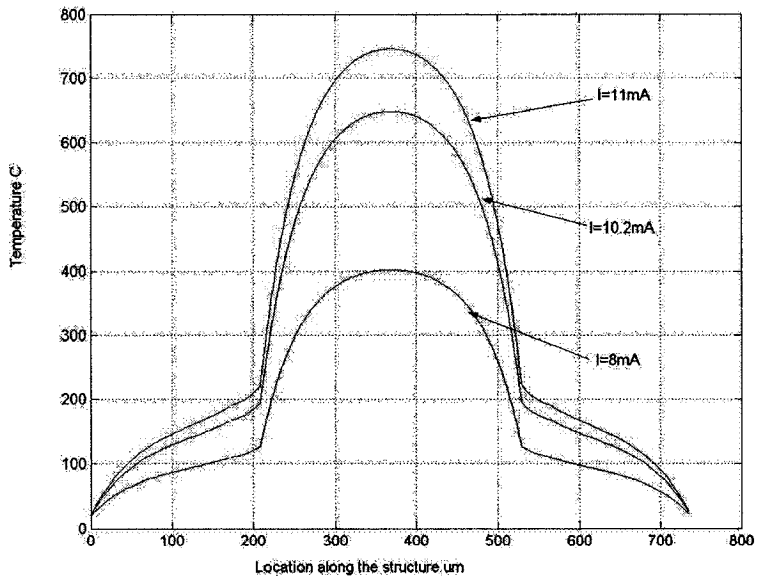

Figure 3.4 Temperature distributions of device A2 with respect to the location along the structure.

The analytical model has also been applied to study the device performance with variable geometrical parameters. In this analysis, the whole structure length is held as constant but the central beam length is variable. Under the same input condition, the longer the central beam, the higher temperature in the whole structure. As a result a larger deflection at the central point of the microbirdge would observed. Figure 3.5 shows the corresponding device temperature distribution when 10 mA input current is applied to the device.

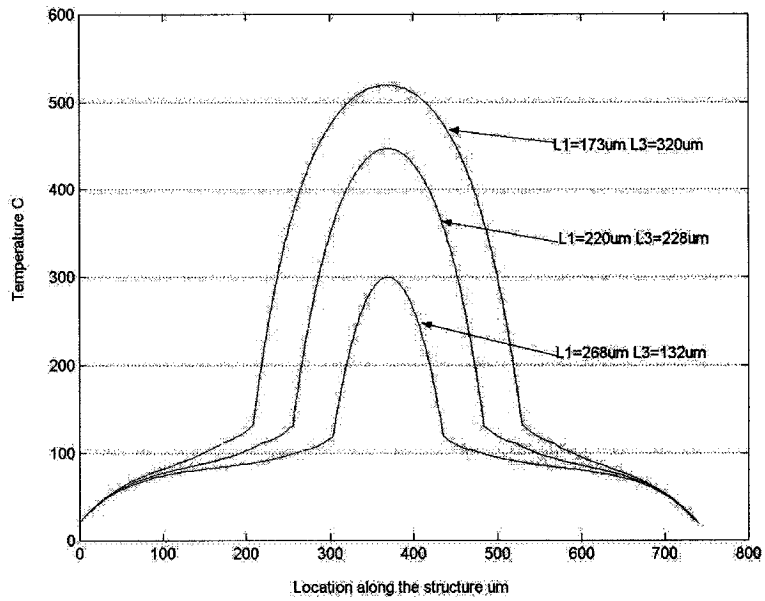

Figure 3.5

Temperature distributions with variation of central beam length at 10 mA input current

The devices in design 2 have a simpler microbirdge structure than devices in design 1. A uniform double clamped poly2 beam form the main actuator structure. The model is applied to device B2 by modifying some boundary conditions. A plot of temperature distribution along location is obtained (Figure 3.7). The geometry of the

device B2 is 500 μm by 20μm. At 7 mA current input, the maximum temperature of 445°C is calculated at the middle of the micro bridge. Figure 3.6 gives the device picture of B2.

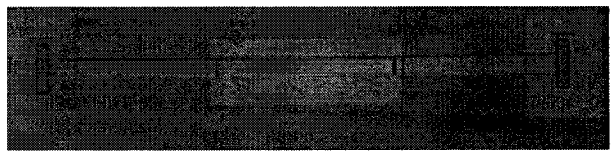

Figure 3.6 Schematic diagram of device B2

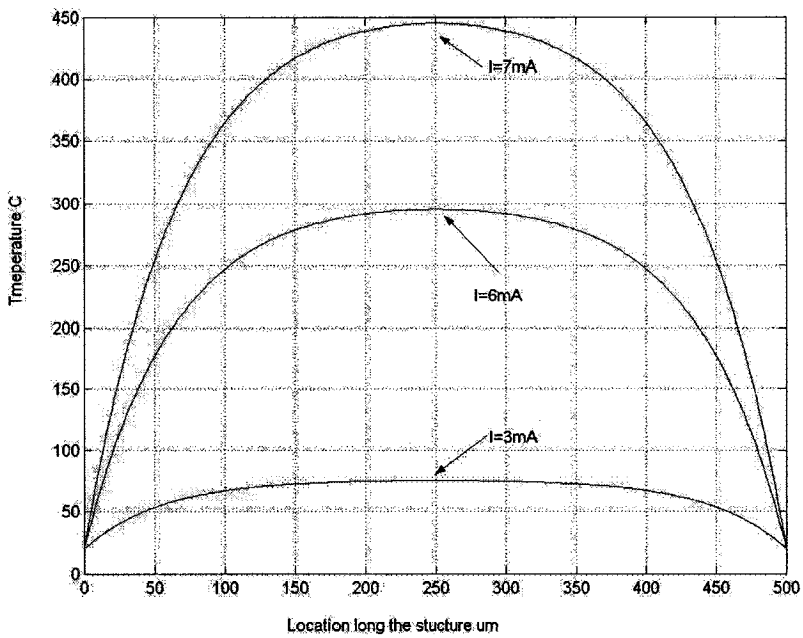

Figure 3.7 Temperature distributions with respect to the location along the structure of device B2.

To show how the geometry affect the devices behavior. Temperature distribution of different devices with various length and width are plotted in the figure below(Figure 3.8). The input current is 4 mA. Device with narrowest bridge structure of 10 um shows the maximum temperature of 503 °C. It is much higher than the temperature on the device with longer and wider microbridge.

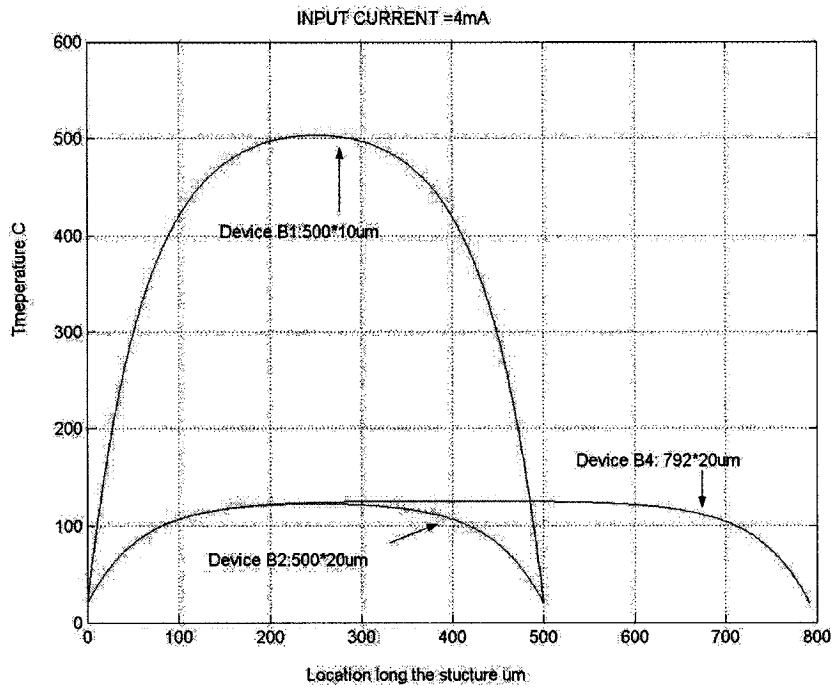

Figure 3.8 Temperature distributions along devices with deferent geometry at 4mA current input.

Table 3.1 list all the material parameter values used in these analyses.

Material Properties	**Value**	**Unit**
Young' Modulus E	$162X10^{9}$	Pa
Poisson' ration v	0.22	
Thermal expansion coefficient K	$2.9X10^{-6}$	C^{-1}
Thermal conductivity of Polysilicon Kp	$32X10^{-6}$	$W\cdot \mu m^{-1}\cdot C^{-1}$
Thermal conductivity of air Ka	$0.026X10^{-6}$	$W\cdot \mu m^{-1}\cdot C^{-1}$
Thermal conductivity of Nitride Kn	$2.25X10^{-6}$	$W\cdot \mu m^{-1}\cdot C^{-1}$
Resistivity of Polysilicon ρ_0	30	$\Omega\cdot \mu m$

Table3.1 Material properties used in the thermal analysis

3.2 Thermal-Elastic Analysis

To simplify the analysis of the microbridge actuator structure as much as possible, while keeping all essential effects, we consider the whole structure as a straight beam with both ends fixed on the substrate [47][48]. It is shown in the schematic diagram below. Temperature rising of the structure causes beams to elongate. Due to the clamped-clamped boundary condition, compressive stress is generated and buckling behavior occurs if the stress exceeds a critical value [48].

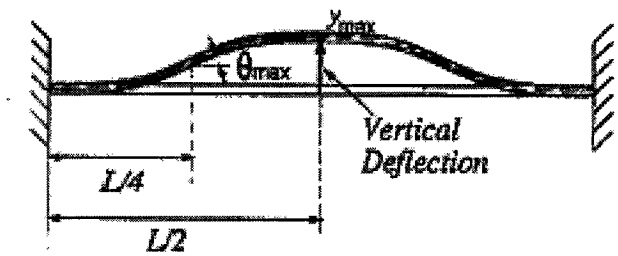

Figure 3.9 Micro Beam with both ends fixed buckles under joule heating [49]

The thermal-elastic problem can be modeled by solving the classical problem of *Elastica* with the governing equations (3.17). [48]

$$\frac{d^2\theta}{ds^2} + \frac{P}{EI}\sin\theta = 0 \quad (3.17)$$

where,θ is the deflection angle with respect to the original axial axis, and S is the coordinate along the deflected beam. E and I are the Young's modulus and moment of inertia of the beam, respectively. P is the thermal loading and y is the lateral deflection that is solved analytically as [48]

$0 < X < (L/4)$

$$Y = \frac{2\beta}{\sqrt{\frac{P}{EI}}}(1-\cos\phi) \quad (3.18)$$

$(L/4) < X < (L/2)$

$$Y = \frac{2\beta}{\sqrt{\frac{P}{EI}}}(1+\cos\phi) \quad (3.19)$$

where

$$\beta = \sin\frac{\theta_{max}}{2} \quad (3.20)$$

$$\phi = \sin^{-1}\left[\frac{\sin\frac{\theta}{2}}{\beta}\right] \quad (3.21)$$

The maximum deflection angle, θ_{max} occurs at one-forth of the beam length due to symmetry and the maximum deflection is at the center that can be derived from

$$Y_{max} = \frac{4\beta}{\sqrt{\frac{P}{EI}}} \quad (3.22)$$

A one-dimensional Duhamel-Neumann constitutive law is then used to relate the thermal stress [50] with respect to temperature changes. This step also connects the electro-thermal analysis to the thermal-elastic problem [48]

$$\frac{-P}{A} = E\varepsilon - \alpha E(T - T_{\infty}) \quad (3.23)$$

where ε is the thermal strain . A is the cross-sectional area of the beam, and α is the thermal expansion coefficient. Temperature differences as well as the strain and the total beam length can be derived in terms of thermal loading and other parameters: [48]

$$\varepsilon = \frac{\Delta L}{L} = \frac{K(\beta)}{2E(\beta) - K(\beta)} - 1 \quad (3.24)$$

$$L = \frac{4[2E(\beta) - K(\beta)]}{\sqrt{\frac{P}{EI}}} \qquad (3.25)$$

where K(β) and E(β) are the first and second kind of complete elliptic integrals . To solve these equations with known geometry and properties, maximum deflection angles are first given from 0 to a small number. The corresponding values of strain are calculated in Eq (3.24), and loading forces are calculated by Eq.(3.25). Eq.(3.23) is then used to solve temperature differences. The maximum deflection is finally derived with respect to the average temperature of the micro beam as [48]

$$Y_{\max} = 4\beta\sqrt{/_{\cdot} - \varepsilon + \alpha_{\cdot} \quad - \mathrm{Ts}_{\cdot}} \qquad (3.26)$$

In the above analysis, theoretical electothermal –elastic behavior of clamped-clamped beam has been established. Computer simulation is used to obtain the complete solutions. The figure below gives the curve of the maximum displacement with respect to the average temperature of devices in family B. Device B4 that has longer beam of 792 μm shows more vertical deflection than B3 and B1, which has the beam of 500 μm in length.

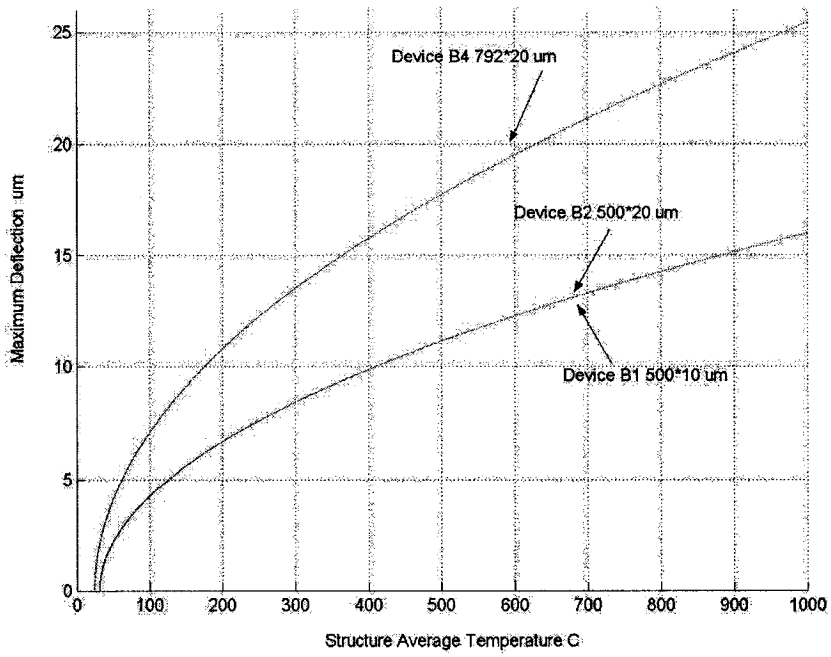

Figure 3.10 the maximum vertical deflection with respect to the structure average temperature of devices in family B

3.3 Thermal Time Constant

To model the thermal transient response, we choose to use electric circuit elements to represent the behavior of devices[50]. Actual devices, exist in a three-dimensional physical continuum. And their behavior is governed by the laws of physics, chemistry, and biology. We can extract simplified device representations that are readily expressible with equivalent electric circuits. In doing so, we gain access to an immensely powerful set of intellectual tools that have been developed for understanding electrical circuits. Circuit analogies permit efficient modeling of the interaction between the electronic and the non-electronic components of a micro system. A further advantage of circuit models is that they are intrinsically correct from an energy point of view.

There are many energy domains, and for each one, it is possible to define a set of conjugate power variables that can serve as the basis of lumped modeling with equivalent circuit elements. Table below identifies some of them.

Energy Domain	Effort	Flow	Momentum	Displacement
Mechanical translation	Force F	Velocity V	Momentum P	Position X
Electric circuits	Voltage V	Current I	N/A	Charge Q
Magnetic circuits	Magneto motive MMF	Flux rate ϕ	N/A	Fluxϕ
Incompressible fluid flow	Pressure P	Volumetric flow Q	Pressure momentumΓ	Volume V
Thermal	Temperature T	Entropy flow rate S	N/A	Entropy S

Table 3.2Example of conjugate power variables [51]

In addition the equivalences listed in the table below exist between the electrical and thermal variables. [52]

Thermal	$\Leftrightarrow$	Electrical	
Temperature	T in K	Voltage	U in V
Heat Flow	P in W	Current	I in A
Thermal resistance	R_{th} in K/W	Resistance	R in V/A
Thermal capacitance	C_{th} in Ws/K	Capacitance	C in As/V

Table 3.3 Corresponding physical variables[52]

To model the thermal transient response of our devices, we consider the whole actuator as a self-heating resistance. All resistors vary with temperature (except those carefully designed for zero TCR coefficient of resistance). We can use a linear variation of resistance with temperature

$$R(T)= R_0[1+ \xi(T-Ts)] \quad (3.27)$$

where R_0 is the resistance of polysilicon at reference temperature Ts. And R(T) is the resistance at temperature T. The temperature coefficient of resistance ξ is typically positive for metallic resistors, but can be either positive or negative for

semiconductors, depending on the region of operation and specific design of the resistor.

The joule heating that occurs when a current flows in a resistor can be represented with the aid of thermal circuit of Figure 3.11.

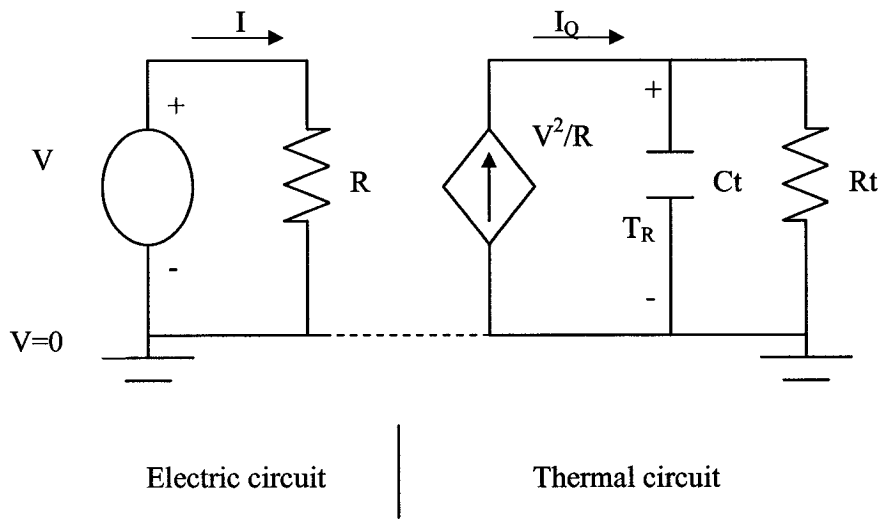

Figure 3.11 Circuit model for the self-heating structure drive from a voltage source.[51]

The electric circuit contains the resistor and a voltage source. The thermal circuit has three elements: a diamond-shaped voltage source that supplies the Joule heat power V^2/R .A thermal capacitor Ct representing the heat capacity of the structure, and a thermal resistor Rt representing the heat resistor, Rt representing the heat conduction from the structure to a thermal reservoir held at temperature Ts. The current variable in the thermal circuit has dimensions of power, and is denoted by I_Q . The ground symbol in the thermal circuit denotes the reference temperature Ts. The voltage across Ct is the temperature difference T_R –Ts. Two grounds are shown connected to each other with a dash line. This connection is not necessary; however, when using circuit simulators to analyze mixed electrical-thermal circuits, it is essential that there be a common ground for entire mixed –domain network.

This is a linear first-order system, but it is now nonlinear because the input term proportional to V^2 has the resistor value in the denominator:[51]

$$Ct\frac{d(T_R - T_s)}{dt} = -\frac{T_R - T_s}{Rt} + \frac{V^2}{R_s(1+\xi(T_R - T_s))} \quad (3.28)$$

If we assume that the total change in resistance is small, we can linearize the model by expanding the denominator to yield

$$\frac{V^2}{R_s(1+\xi(T_R - T_s))} \approx \frac{V^2}{R_s}(1-\xi(T_R - T_s)) \quad (3.29)$$

substituting and collecting terms yield

$$\frac{dT_R}{dt} = -\frac{1}{CtRt}(1+\frac{\xi V^2 Rt}{R_s})T_R + (\frac{V^2}{R_s Ct} + \frac{T_s}{R_t} + \frac{T_s \xi V^2}{R_s Ct}) \quad (3.30)$$

This is a first order system. The factor that occupies the usual place for the time constant of a first order system depends on V^2, which might be time vary. However if V is constant, the time constant τ for the system is [51]

$$\tau = -\frac{CtRt}{1+\frac{\xi V^2 Rt}{R_s}} \quad (3.31)$$

According to the equations above, heat conduction processes can therefore be modeled by an equivalent circuit .In the equation, thermal capacity is defined as the amount of heat required to raise (or lower) its temperature by 1 K. It is found from

$$Ct = \rho V C_m \quad (3.32)$$

Where ρ is the mass density of polysilicon and Cm is the specific heat per unit mass, V is the volume of the structure. Thermal resistance can be determined by

$$Rt = L/\lambda A \quad (3.33)$$

Where λ is thermal conductivity measured in $W \cdot K^{-1}$, A is area ,and L is length of the structure. This matches the relationship between electrical conductivity (A·m-1·V-1) and electrical conductance ($A \cdot V^{-1}$).

The material parameter values are going to use are shown in Table below:

Parameter	Symbol	Value	Unites
TCR	ξ	$2.5*10^{-3}$	k^{-1}
Density	ρ	2330	Kg/m^3
Specific heat	Cm	712	J/(kg-k)
Thermal conductivity	K	32	W/(K-m)

Table 3.4 Material property used in thermal time constant calculation

One serious complication here is that unlike electrical currents, which tend to stay rigorously confined to conductors, heat currents can leak out the sides of thermal resistors by conduction, convection, and radiation. Therefore, accurate modeling of the transient effects of electrical thermal actuator is a more complex task.

We already have all the elements to evaluate the thermal time constant of the device. The thermal frequency could be derived from the thermal time constant. More discussion about the thermal frequency and the device operational frequency will be carried out in chapter 4.

The displacement calculated by the thermal-elastic model will be compared with the experimental results in Chapter 4 also.

CHAPTAR 4: EXPERIMENTAL RESULT

Critical to the use of thermal micro actuator in optical switching applications is characterization of deflection, power consumption and frequency response. This chapter presents the results of the measurements, which were performed in the air and in vacuum ambient. The first section concerns the experiment setup as well as the hardware and software used in the measurement. The second section describes the measurement result of the devices in each of the five families. Device in family B are characterized in the most detail. Device performance in air and in vacuum is compared. The ANSYS simulation and theoretical model help to investigate the device performance in different ambient. The next section deals with the characterization of the dynamic response of the devices. The operational frequency and the fist observed resonance frequency is also documented.

4.1 Experimental Setup

In this section, the hardware and software tools that were used in the experiments are described. Their operation parameters are also reported. The hardware in this experiment includes Integrated Circuit (IC) Inspection Probe Station, HITACHI S-520 Scanning Electron Microscope and WESTBOND 7476E Wire Bonder. The layout design and 3D model generation are conducted by MEMS pro. ANSYS 6.1 is the finite element simulation tool that helps to carry out couple field simulation.

4.1.1 IC Probe Station

The probe station used in this experiment is Micro Manipulation's Model 6000 Integrated Circuit inspection station that consists of one stage with three degrees of freedom and one microscope subsystem supplied by Bausch&Lomb. The XY stage is driven by two lead screws with coarse and fine adjustment knobs. The vertical or Z drive comes from the rotation of an internal threaded stage. The stage rotation is accomplished by a thimble mounted on the stage. The microscope subsystem with two degrees of freedom is mounted on another stage. The drives have been coupled to the fine adjustment lead screws through flexible helical couplings supplied by Helical Products Inc. The system is very susceptible to vibrations from the external environment.

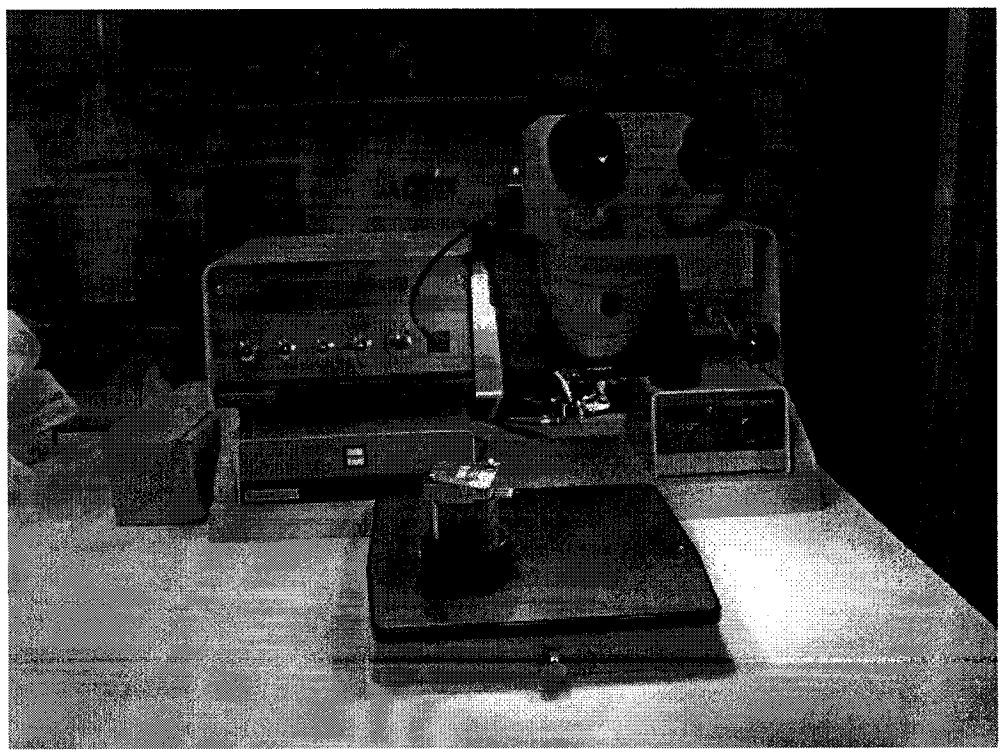

Figure4.1 WEST.BOND 7476E Wire Bonder

4.1.2Wire Bonding Machine

Before we tested the devices, Wire bonding was conducted by WESTBOND 7476E wire bounder. Two kinds of chip carrier, PGA68 and DIP40, were used in this process, and 5 dies were bonded. DIP 40 package will be used in the test carried out in the air. PGA68 package, which has smaller dimension and easy to be tilted or rotated in SEM chamber, is used in measurement conducted by SEM. Wire bonding is an electrical interconnection technique using thin wire and a combination of heat, pressure and/or ultrasonic energy [53]. Wire bonding is a solid phase welding process, where the two metallic materials (wire and pad surface) are brought into intimate contact. Once the surfaces are in intimate contact, electron sharing or inter- diffusion of atoms takes place, and forms formation of wire bond. Wire bonding process begins by firmly attaching the backside of a chip to a chip carrier using either an organic conductive adhesive or a solder (Die Attach). The wires then are welded using a special bonding tool (capillary or wedge). Gold and aluminum are the commonly used wire materials, in addition, copper and silver have also been used. In our system, aluminum wire is used. The figure below shows one of our chips after wire bonding.

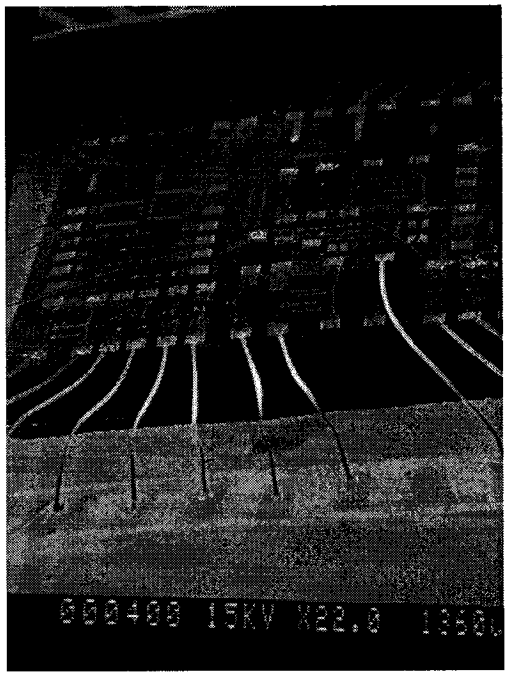

Figure 4.2 The chip after wire bonding

Operation parameter setting of the WESTBOND 7476E wire bounder is list in the table below

Ultrasonic Power	Ultrasonic Time	Free Furnace operating Temperature
300	30(ms)	140(^{0}C)

Table4.1 WESTBOND 7476E operation parameter setting

4.1.3 Scanning Electron Microscopy

HITACHI S-520 Scanning Electron Microscope was used in our experiment to test our devices.The Scanning Electron Microscope (SEM) is one of the most versatile and widely used tools of modern science . By scanning an electron probe across a specimen, high resolution images of the morphology or topography of a specimen, with great depth of field, at very low or very high magnifications can be obtained. Characterization of

fine particulate matter in terms of size, shape, and distribution as well as statistical analyses of these parameters, may be performed.

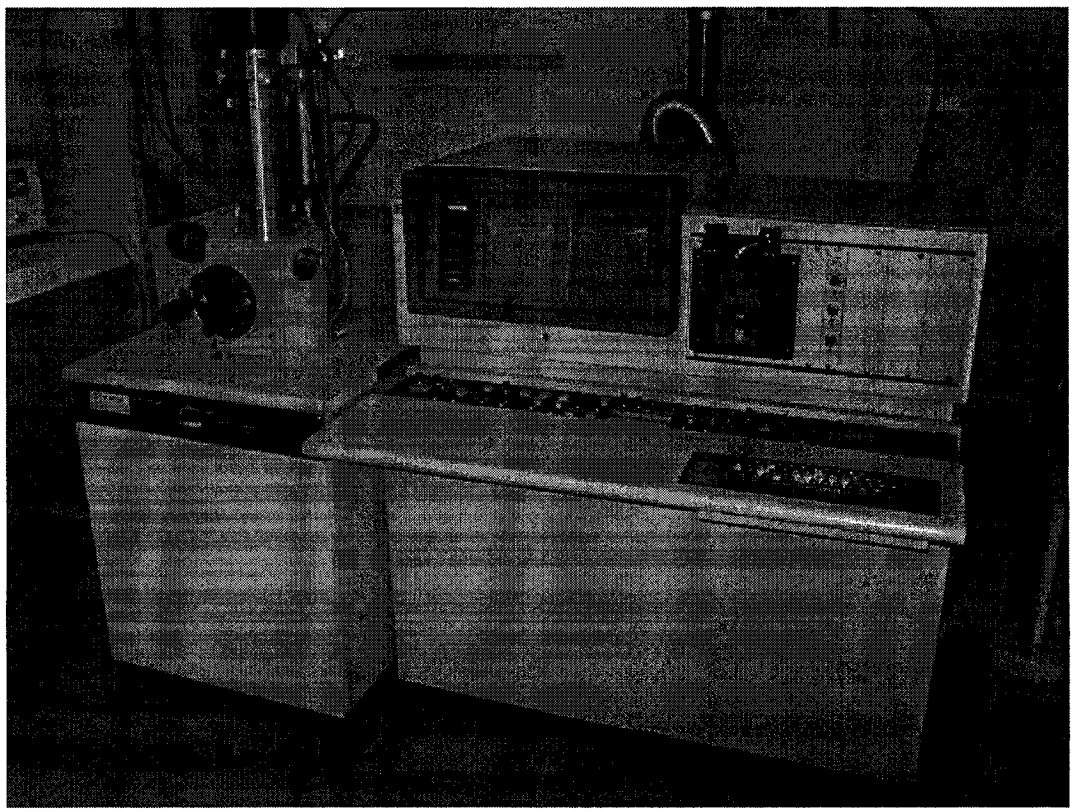

Figure4. 3 HITACHI S-520 SEM

The SEM uses electrons instead of light to form an image. The schematic diagram of SEM is shown in Figure 4.4 The "Virtual Source" at the top represents the electron gun, producing a stream of monochromatic electrons. The stream is condensed by the first condenser lens. (usually controlled by the "coarse probe current knob"). This lens is used to both form the beam and limit the amount of current in the beam. It works in conjunction with the condenser aperture to eliminate the high-angle electrons from the beam .The beam is then constricted by the condenser aperture (usually not user selectable), eliminating some high-angle electrons .The second condenser lens forms the electrons into a thin, tight, coherent beam and is usually controlled by the "fine probe

current knob" .A user selectable objective aperture further eliminates high-angle electrons from the beam .A set of coils then "scan" or "sweep" the beam in a grid fashion (like a television), dwelling on points for a period of time determined by the scan speed (usually in the microsecond range) . The final lens, the Objective, focuses the scanning beam onto the part of the specimen desired. When the beam strikes the sample (and dwells for a few microseconds) interactions occur inside the sample and are detected with various instruments. Before the beam moves to its next dwell point these instruments count the number of interactions and display a pixel on a CRT whose intensity is determined by this number (the more reactions the brighter the pixel). This process is repeated until the grid scan is finished and then repeated, the entire pattern can be scanned 30 times per second. [54]

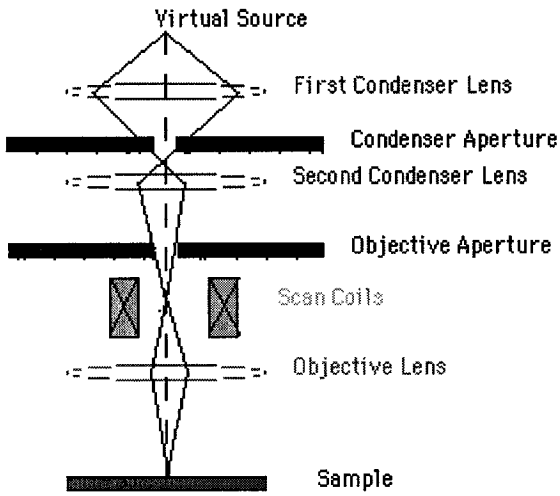

Figure4.4 Schematic diagram of Scanning Electron Microscope [54]

Our test was conducted by using HITACHI S-520 SEM. To obtain clear image of the polysilicon structure, adjustment of the system setting is performed before testing. The optimized operational parameters setting are listed in the table below:

Parameter	Value	Unit
Emission Current	30-50	uA
Accelerating Voltage	15	kv
Working Distance	30	mm

Table4.2 SEM operational parameter Setting

4.1.4 Simulation Tools

Couple field finite element analysis of our electro thermal actuator was carry out by ANSYS 6.1.The tools could perform the following tasks: Build computer models or transfer CAD models of structures. Apply operating loads or other design performance conditions. Study physical responses, such as stress levels, temperature distributions, or electromagnetic fields. Optimizes a design in early stage of development to reduce production costs. It performs prototype testing in environments where otherwise would be undesirable or impossible (for example, biomedical applications).

coupled-field analysis is an analysis that takes into account the interaction (coupling) between two or more disciplines (fields) of engineering. A piezoelectric analysis, for example, handles the interaction between the structural and electric fields: it solves for the voltage distribution due to applied displacements, or vice versa. Other examples of coupled-field analysis are thermal-stress analysis, thermal-electric analysis, and fluid-structure analysis.

Coupled-field problems can be solved using the direct method or the sequential method. The direct method performs the coupled-field analysis in one step using coupled-field elements. It usually involves just one analysis that uses a coupled-field element type containing all necessary degrees of freedom. Coupling is handled by calculating element matrices or element load vectors that contain all necessary terms. An example of coupled-field element is SOLID98 .The sequential method performs the coupled-field analysis in

multiple steps, where the results from one step are used as input to the next step. In a sequentially coupled physics analysis, you can couple the two fields by applying results from the first analysis as loads for the second analysis. The load transfer occurs external to the analysis, and you must explicitly transfer loads using the physics environment. An example of this type of analysis, is a sequential thermal-stress analysis where nodal temperatures from the thermal analysis are applied as "body force" loads in the subsequent stress analysis.

We used the sequential method to evaluate our actuator. The nonlinear thermal-electric problem was solved using SOILD98 elements with only the TEMP and VOLT degrees of freedom active, and the mechanical problem was solved using SOILD92 elements. The temperatures calculated in the thermal analysis were applied as loading to the mechanical model using the LDREAD command.

To define material properties for this analysis, we must convert the given units for Young's modulus, resistivity, and thermal conductivity to μ MKSV units. The units have been converted to μ MKSV, and are shown in the following table.

Material Properties	**Value**	**Unit**	**Material Properties for Polysilicon (μMKSV units)**
Young' Modulus E	$162X10^{9}$	Pa	160e3 MPa
Poisson' ration v	0.22		0.22
Thermal expansion coefficient K	$2.9X10^{-6}$	K^{-1}	2.9e-6/oK
Thermal conductivity of Polysilicon Kp	$32X10^{-6}$	$W\cdot \mu m^{-1}\cdot C^{-1}$	3.2e7 pW/μ moK
Resistivity of Polysilicon ρ_0	30	$\Omega\cdot \mu m$	3e-11 ohm-μ m

Table 4.3 Material Properties used in the ANSYS simulation

4.1.5 MEMSpro:

MEMS Pro is a PC based MEMS design tool originally developed by Tanner Research, Inc. In our project, most of our 3D model for the ANSYS simulation was generated by MEMS pro. Because of their many years experience in IC layout tools, the MEMSPro is very good in layout design and the device modeling. MEMSPro interfaces with ANSYS to supplement its lack of finite element simulation capability.

L-Edit is an interactive, graphical layout editor for MEMS and IC design.[55] This full-custom editor is easy-to-use, and fully hierarchical. Primitives include boxes, polygons, circles, lines, wires, labels, arcs, splines, and tori. Drawing modes include 90°, 45°, and all-angle layout. Shortcuts are also available for quickly laying out circles, tori, pie slices, splines, and "curved polygons" with true curved edges. The MEMS Pro Toolbar gives access to MEMS specific design features. MEMS Pro also includes access to the process definition graphical interface, 3D modeler and viewer, MEMS specific DRC, and MEMSLib (the MEMS library).

Accurate three-dimensional (3D) visualization of design-in-progress is crucial to successful fabrication. We can create 3D models of MEMS device layout geometry directly in L-Edit using one of the many foundry fabrication process descriptions, or by specifying our own custom process. The view of 3D model can be customized with features such as panning, zooming, cross-section modeling, and other viewing controls. 3D solid model geometry can be exported in a SAT format. And then we can import the 3D geometry to ANSYS, and carry out finite element simulation.

4.2 Experimental Result

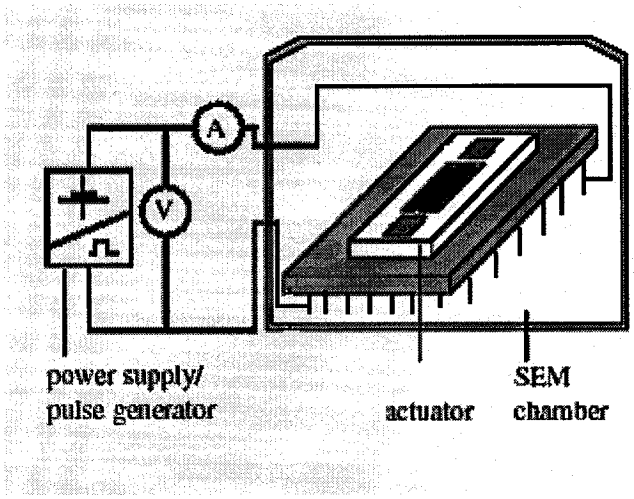

Figure 4. 5 Setup for testing the actuators

In this work, tests were carry out to characterize the device performance in deferent ambient. The devices were tested in air as well as in vacuum condition. The deflection in air was measured by optical microscope with focus/defocus method, which gave a measurement error about +/- 1μm. Before applying voltage, we focused the microscope to get the clear profile of the devices and record the scale on fine adjust knob. After devices move up, we focused again to get the clear image of the moved part. By reading the difference on the fine adjust knob scale, the vertical displacement was obtained

To test the device's performance in vacuum, the chips were put into SEM chamber. Figure 4.5 shows the setup for testing the devices. A power supply provided the input power to heat the actuators. For pulsed input, which would be used in the frequency response test, a function generator was used instead. The current through the device and the applied voltage were used to calculate the electrical input power. The SEM chamber, where accurate measurement of the lateral displacement (Z-direction) can be performed,

provided a vacuum environment to eliminate any influences from the ambient. To clearly observe the vertical displacement, the chip was tilted 80° to 85° from the horizontal position by the tilt control knob on the specimen goniometer stage of the SEM. $5*10^{-6}$T vacuum was reached before conducting the tests. It should be pointed out that when actuators work in SEM chamber and at relative low working temperature, heat convection and radiation become weak; and conduction is the dominant heat loss mechanism. Therefore, in the ANSYS simulation, we only considered the heat conduction and ignored the other two heat loss mechanisms. For each family, at lease one device was tested.

4.2.1 Device In Family A

Devices in family A employed a microbridge actuator to lift up a mirror plane. The bridge structure is composed of a central beam, two side arms and two rectangular connections. The micro mirror is connected to the bridge structure by a central cantilever arm. The other end of the central cantilever arm is fixed to the substrate. (Figure 2.79a)

Devices were tested in air. The geometry and measured resistance are given in table 4.4. Both of devices were the same in total device length. But the length of central beam and side arm were different. The device with longer central beam shown more vertical displacement that was consistent with the theoretical model.

	Total length	Central Beam	Central Cantilever Arm	Side Arm	Resistance
Device A1	737μm	130μm *10μm	48μm *8μm	268μm *10μm	924 Ω
Device A2	737μm	320μm *10μm	48μm *8μm	173μm *10μm	1266 Ω

Table 4.4 Device geometric data and measured resistance of devices in Family A.

For the device with 320μm length of central beam, a maximum vertical displacement of 12.6 μm was achieved by applying 10.24 mA input current and 8.5V input voltage. Figure 4.6 shows the measured vertical displacement as a function of input power. Each measurement was repeated 3 times, and the average values were plotted.

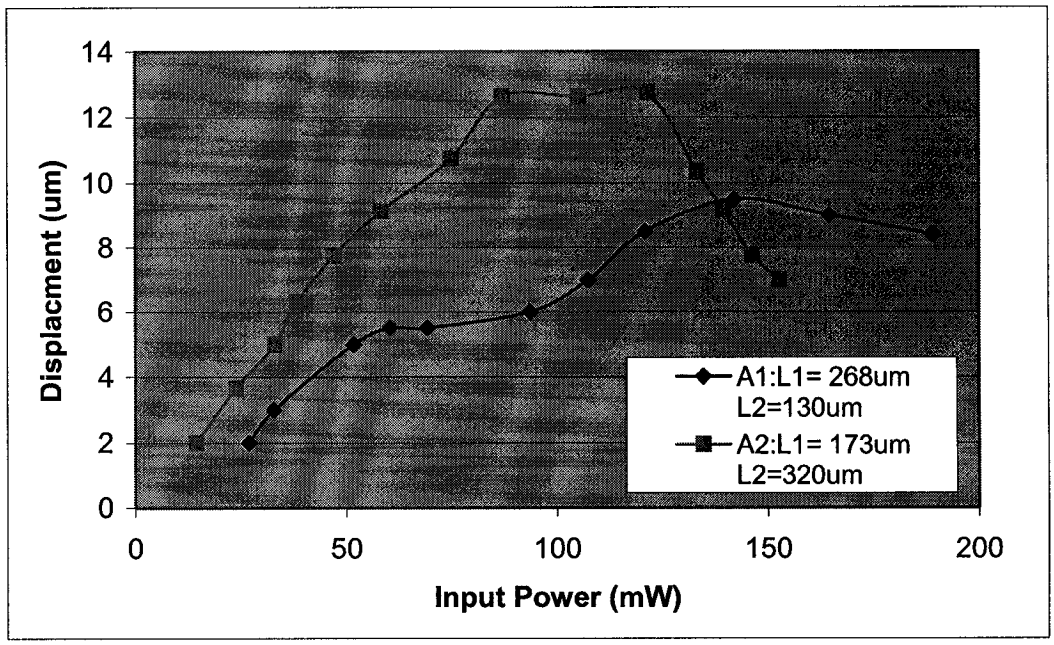

Figure 4.6 Experiment measurement of the micromirror vertical displacement with respect to input power

Experimentally, the microbridge structure does not deflect under low input currents until a certain current is reached to generate a large enough compressive stress for buckling. To avoid a high temperature melting effect, the experiments confine to currents below 15mA. It was observed that after the input current reached a critical value, increasing input current will not improve the vertical deflection any more.

For the device with 320 μm long central beam, when we continued to raise the input power up to 146 mW, only 7μm vertical displacement was obtain, which was lower than 12.6 μm when 87mW input was applied. We found that when 12 mA ,8.8 V (105

mW)input was applied, the central beam began to turn to red color. At the temperature above this (higher current), the mechanical properties of the poly silicon changes, causes that vertical displacement drops down. From experimental results, we also found that the ideal operational current was below 11 mA for the device with 320 μm central beam. The actuator was drove up to the maximum displacement at this current. According to the theoretical calculation the maximum temperature of the structure was about 750 ^{o}C at this input condition.

4.2.2 Device in Family B

To test the basic mechanical properties of the bridge structure, the designs in Family B are series of basic bridge structures.(Figure2.8) Different geometry with variety length width is implemented. Device in this family are characterized in the most detail. Device performance in air and in vacuum is compared. The ANSYS simulation and theoretical model help to investigate the device performance in different ambient.

4.2.2.1 Device B2 in Vacuum

Figure 4.7 depicts measurement data of vertical displacement against the input power for a simple microbridge actuator B2 with the following dimensions: length, 500 μm; width 20 μm; and beam thickness 1.5 μm. Displacement means the deflection of the middle of the bridge in the upward direction (Figure 4.8) with respect to the unheated state. It should be noted that in the unheated state the central part of the beam curved up with a deflection of about 5 μm above the poly0 support (Figure 4.8). A poly 2 temporary support structure, which was removed during release process helpes to form this

curvature during the fabrication. The magnification of SEM was set at 500, before carrying out measurement.

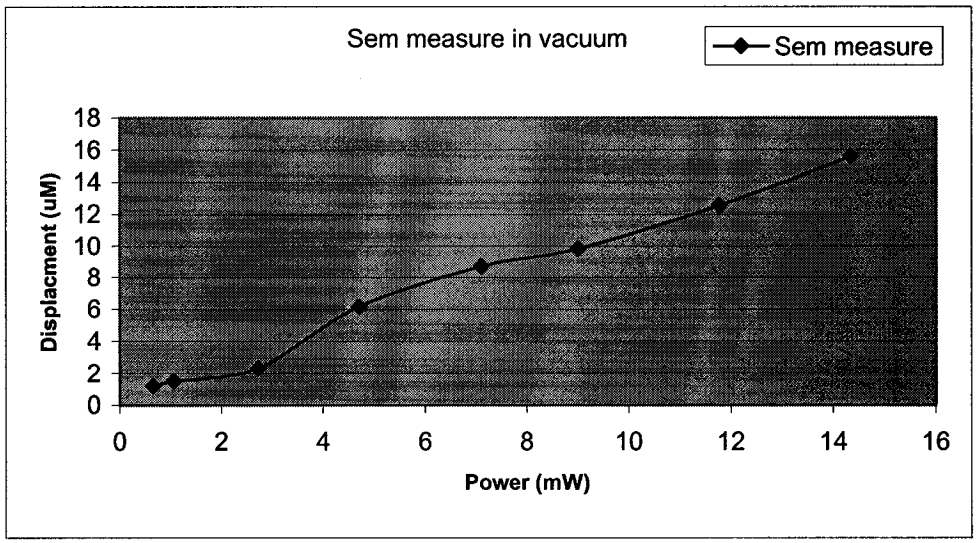

Figure 4.7 Vertical displacement with respect to input power of device B2 in vacuum ambient.

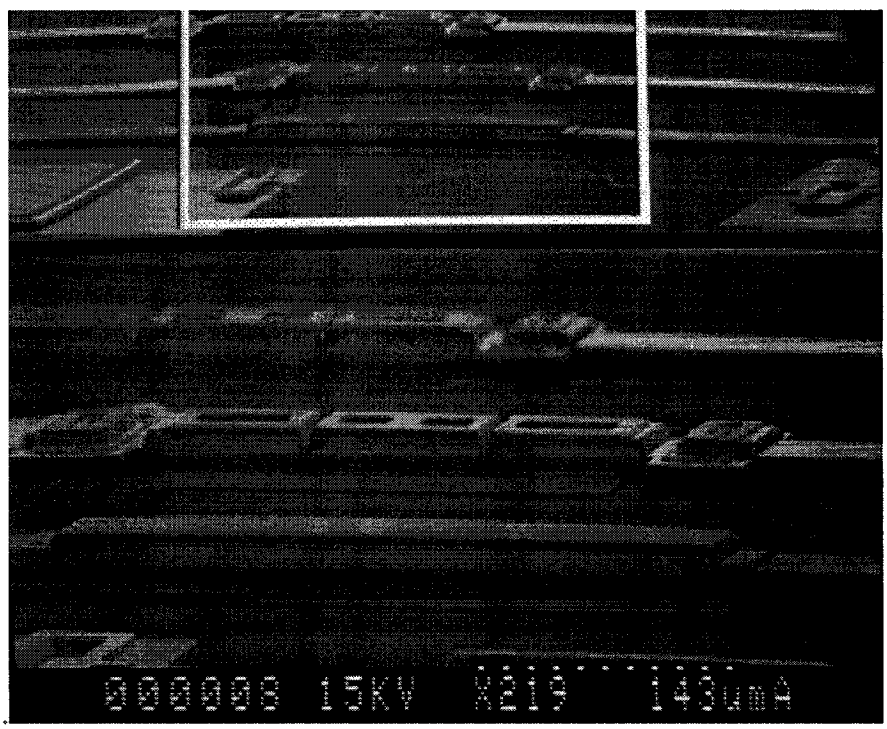

(a)

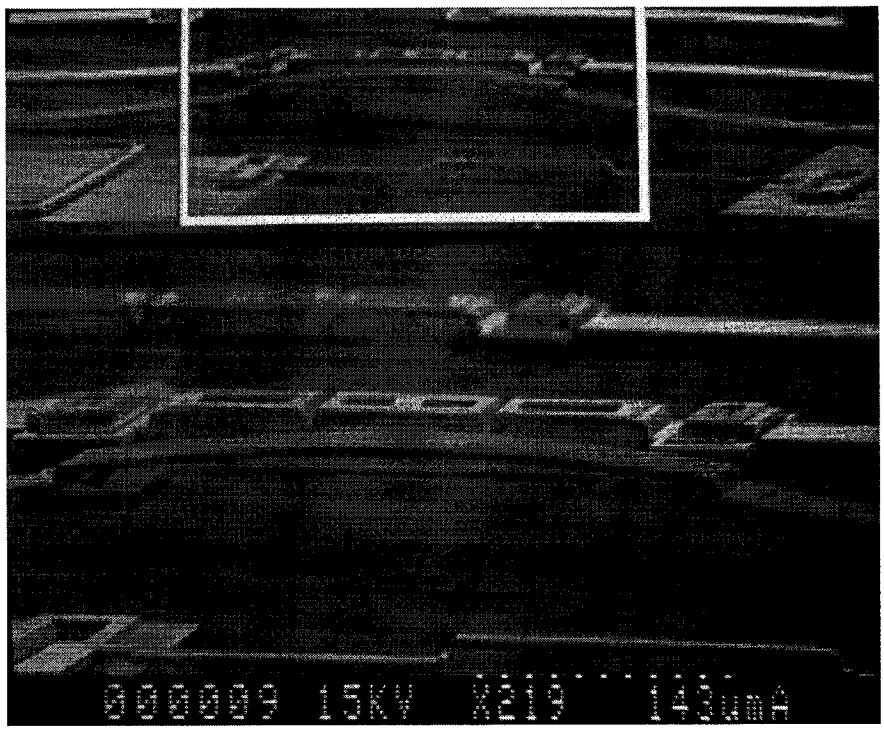

(b)

Figure4.8 (a) Device B2 in unheated state (b) Device B2 buckle up at 4.1V , 3.5mA input power

Input Voltage (V)	Measured Displacement (μm)	Simulated Maximum Temperature (K)	Simulated Displacement (μm)
2.01	6.15	532.8	9.5
3	9.8	766	12.1
3.57	12.54	916	15
4.1	15.6	1034	17.5

Table4.5 ANSYS Simulated maximum temperature and displacement compare with experimental result.

To avoid high temperature melting, the test was stopped at 4.1V, 3.5 mA. At 4.1V, a displacement of about 15.6 μm was observed. The comparison of the experimental result with those obtained by ANSYS simulation is shown in table 4.5. The simulation result

shows that the maximum temperature is 1034k, and the maximum deflection is 17.5 μm at 4.1v input. All the simulated displacement is higher than the experimental result. In ANSYS simulation only consider the heat conduction as the heat loss mechanism, and ignore the other effects. This will result in over estimated of the temperature distribution and vertical displacement of the actuator. Figure4.9 and Figure 4.10 give the temperature distribution and structure deflection of the actuator simulated by ANSYS at 4.1V input

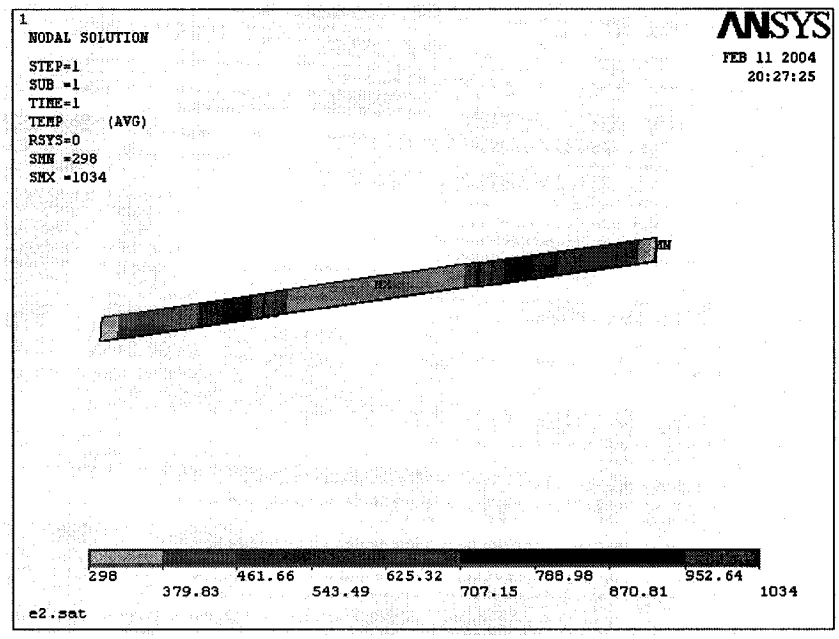

Figure 4.9 Temperature distribution of device B2 at 4.1V input

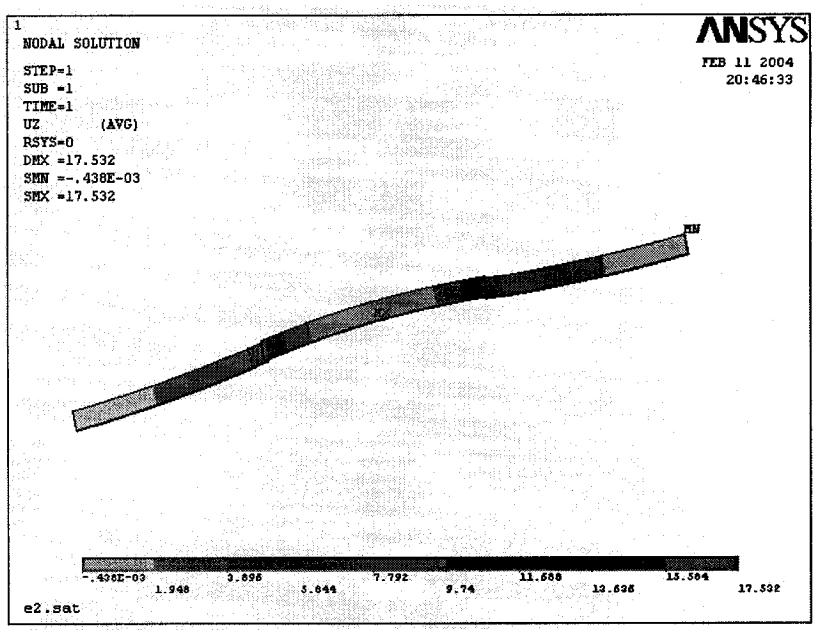

Figure 4.10 Structure deflection of device B2 at 4.1V input

4.2.2.2 Device B2 in Air

To characterize the devices in air, the devices were tested using an optical microscope. The vertical displacement of the actuator was measured by focus/defocus method. Figure 4.11 shows the displacement against the input power for device B2 .At an input power of 66 mW a vertical deflection of 12μm was reached. The theoretical calculation of the displacement, which we discussed in chapter 3 is compared with the experimental result. Since the actuator work in the air, the heat loss by the conduction of the air was considered. Form the curve, we find about 20% error exists between theoretical calculation and the experimental result. In the theoretical model we consider the microbridge actuator as a uniform straight beam. However for the real device, the middle part of the micro bridge, under which the poly2 temporary support was placed was curved up. In this way the microbridge was not exactly a straight beam, and a pre-curvature existed. This can explain why more vertical deflections are produced by the real device compare to the theoretical calculation.

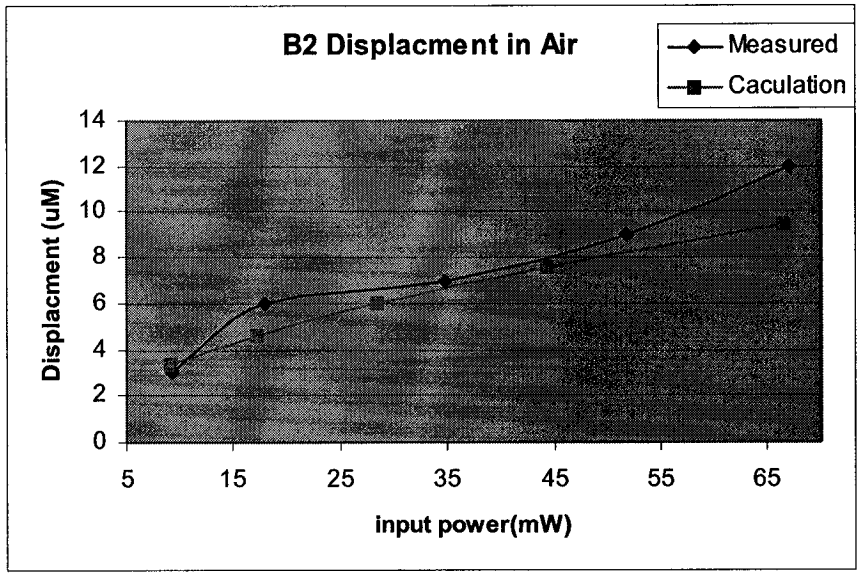

Figure 4.11 Vertical displacement with respect to input power of device B2 in air

Table below lists the theoretical calculation result of the average structure temperate, maximum temperature and vertical deflection at different input voltage.

Voltage (V)	Current(mA)	Displacement (um)	Average Temperature (C°)	Maximum Temperature(C°)
3.07	3	3.318	63	75
4.28	4	4.62	101.81	122
5.68	5	6	156	191
7.38	6	7.6	234	295
9.5	7	9.4	347	445

Table4.6 Theoretical calculation of average structure temperate, maximum temperature and vertical deflection at different input voltage

Vertical displacement of device B2 in vacuum and in air is compared in Figure 4.12. The influences of the ambience are eliminated in vacuum environment. Less heat loss will happen. Therefore, at the same input condition higher temperature will obtain in vacuum than in air, and more vertical displacement is observed. It is found that to reach the same displacement, 3 to 6 times more power will be consumed in air than in the

vacuum. In vacuum the microbridge started to buckling up when 0.79V 0.83mA power was applied, while in air, upward movement happened at 2.5V, 3.03mA input applied.

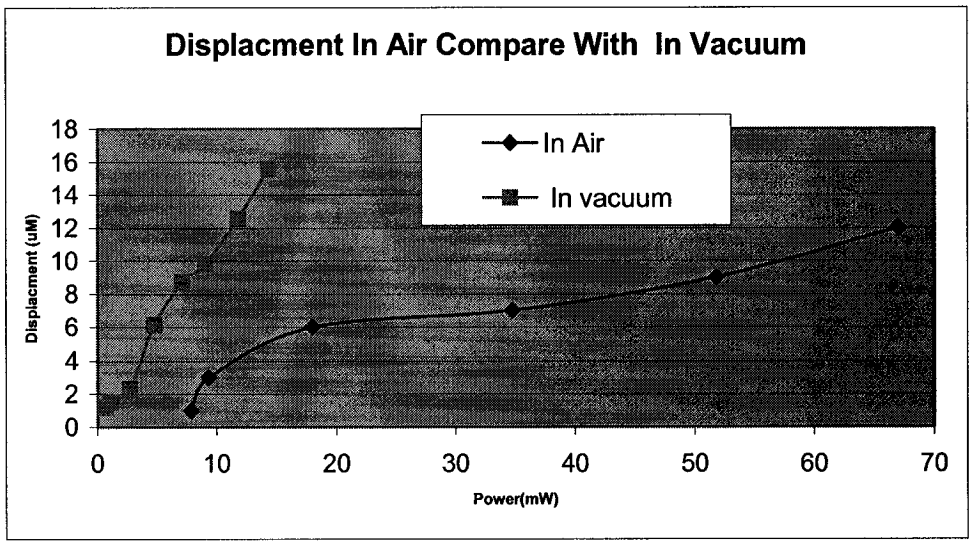

Figure 4.12 Vertical displacement of device B2 in the air compare to that in vacuum

4.2.2.3 Other Device in Family B

To show how the geometry affects the device performance, three more devices were tested in family B. The plot of displacement versus input power is given in Figure 4.13. The geometry and measure resistance of each device are listed in the table blow.

Device	length (μm)	Width(μm)	Resistance(Ω)
B1	500	10	1396
B2	500	20	910
B3	500	30	554
B4	792	20	980

Table 4.7 Geometric data and resistance of other devices in family B

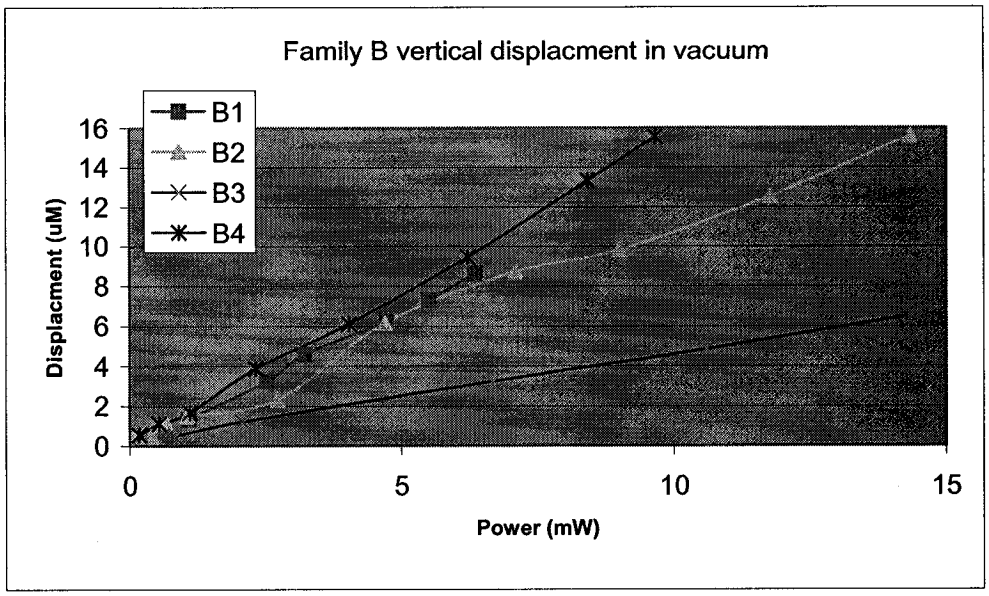

Figure 4.13 Vertical displacement of some devices in family B versus input power in vacuum

Devices B1, B2, and B3 have the same length of 500μm but different width. B3 has the widest beam of 30μm, and B1 has the narrowest beam of 10μm. From the plot, B1 shows more vertical displacement than the other two devices. Devices B4 and B2 have the same width of 20 μm, but different length. Device B4 with longer beam gives more vertical deflection than device B3. To achieve same vertical deflection, a design with longer and narrower bridge structure will consume less power than shorter and wider one. So a long and narrow microbirdge design should give more vertical deflection and consume less power. However, a slim beam is not always a robust structure in the micro actuator design.

Device B4 was broken by high temperature when a 4 V input was applied on the device. The maximum observed displacement of B4 was 15.56μm at 3.5V 2.76mA input. Figure below shows the SEM image of the device B4 after broken. The structure broke at

the narrowest part of the poly2 beam, where an etching hole was placed. The beam width at that part was only 5 μm .The narrow beam has higher resistance than the other part of the bridge structure. When voltage is applied, more joule heat will generate by the higher resistance. Therefore, the narrow poly2 beam suffers from the higher temperature, and broke.

Here is one thing need to be noted. Since a 20μm by 500 μm beam structure without any etching hole employed is released successfully by CMC in the design of B2. Furthermore, in the rest of 14 dies, all of this structure has been released successfully. In the future design, the etching holes will not necessary for the beam narrow than 20μm.

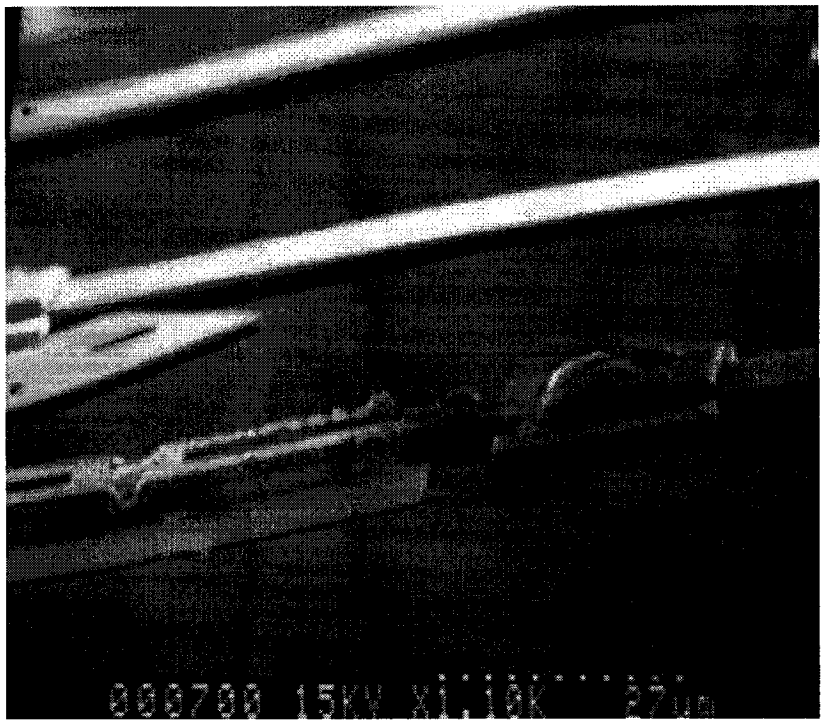

Figure 4.14 Device B4 melted by high temperature at 4V input

The resistance of the pollysilicon structure increases with the input power. Figure 4.15 displays the plot of the device B3's resistance versus input power. The B3 's resistance increases from 554Ω to 648Ω with the power rising from 0.48 mW to 14mW.

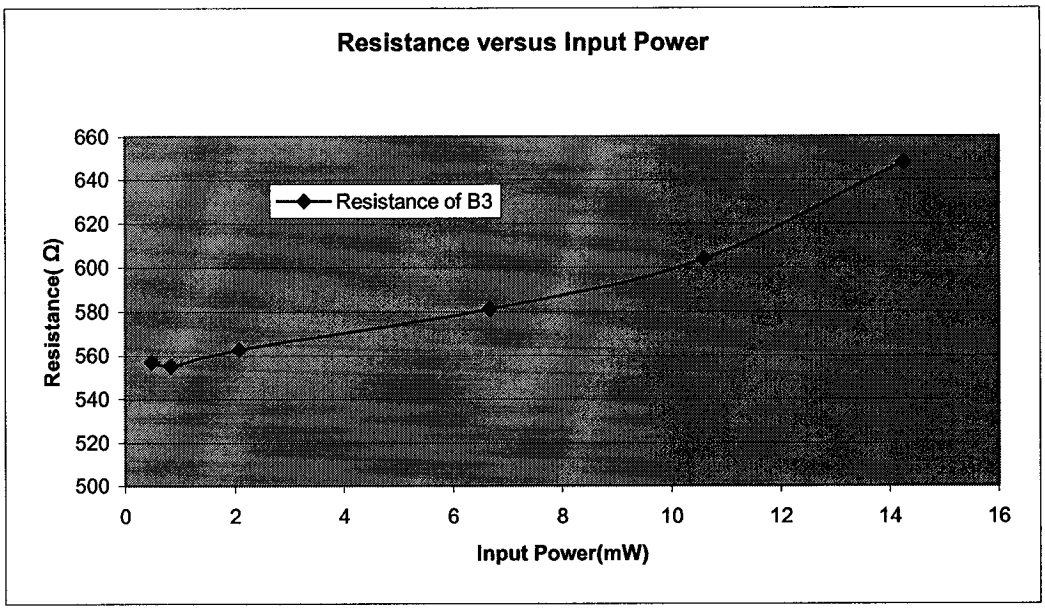

Figure 4.15 Resistance of device B3 increases with power input

4.2.3 Device in Family C

Devices in family C are some optical switch designs. They originate from the design in family A, but have simpler bridge structure. The cantilever arm with a micromirror is placed at the middle of the bridge. The Figure 2.11 shows the layout design, and the SEM picture of device C4. For testing purpose some device without mirror plane, device C2 and C3, are fabricated also. By measuring the deflection of the central cantilever beam, the actuation force could be obtained.

The test of devices in other family was conducted with the same experiment setup. Two devices, C4 and C2, were tested in family C. These devices were tested in vacuum. The geometric data and measured static state resistances of these devices are listed in Table 4.8. Figure 4.16(b) shows a 25 μm by 25 μm micro mirror raised by the microbridge actuator of device C4 when 4.5 V, 2.01 mA input power was applied.

Device	Total Device Length(μm)	Width(μm)	Cantilever Arm Length(μm)	Cantilever Arm Width(μm)	Poly 0 Support Length(μm)	Poly1 Support Length(μm)	Resistance (Ω)
C2	300	5	85	5	108	100	1891
C3	400	6	113	5	108	100	1971
C4	400	8	77	5	108	100	1490

Table 4.8 Geometric data and static state resistances of devices in family C

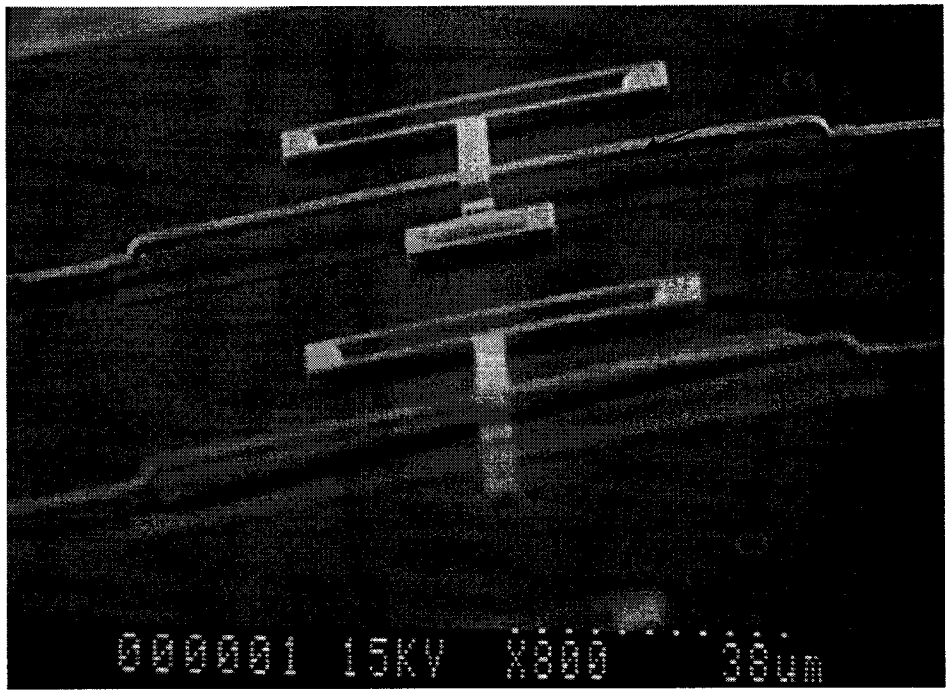

(a)

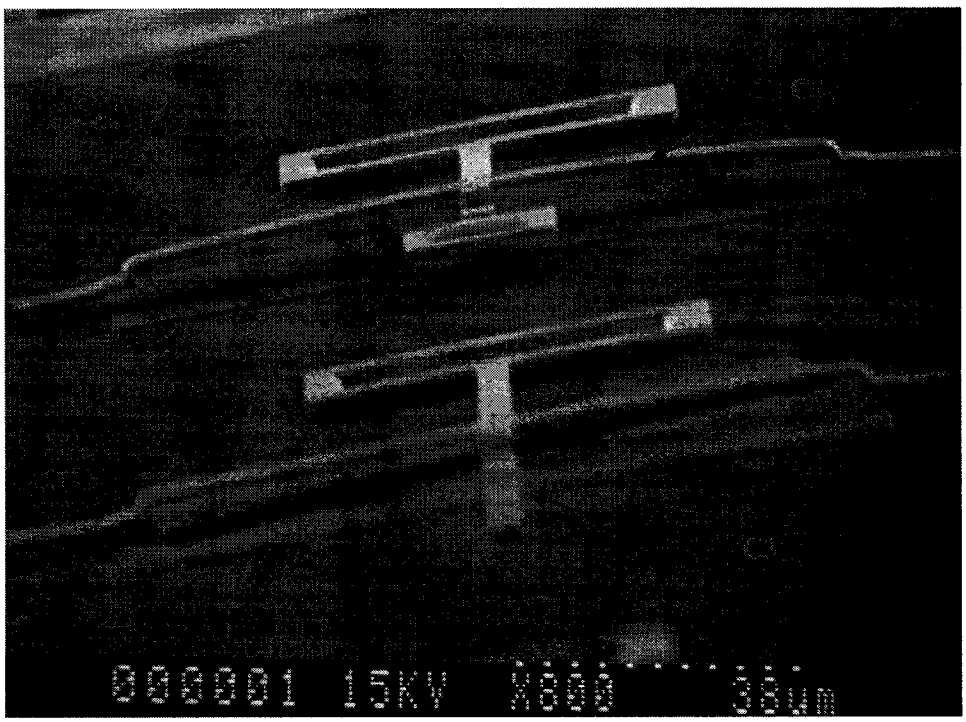

(b)

Figure 4.16 SEM picture of device C4 (a) Device in unheated condition (b) Device left up after 4.5 V, 2.01 mA input power applied

The magnification of SEM was set at 5K for C4 and 4K for C2 before the measurements. Measured vertical displacement of device C2 and C4 are shown in Figure 4.17. Displacement means the deflection of the middle of the bridge in the upward direction with respect to the unheated state. This test was stopped at 4.6V to avoid high temperature melting of the structures. Device C4 started moving up at 0.9v, 0.6mA, and device C2 started moving up at 2.19V 1.08mA. The maximum vertical deflection is 4.65 μm for C4 at 9.31mW power input, and 3.24μm for C2 at 7.75 mW power input. The measured curves shows that device C4, with a longer beam, is deflected larger comparer to device C2 with shorter beam. Both devices show good yield about 90% by MUMPS process.

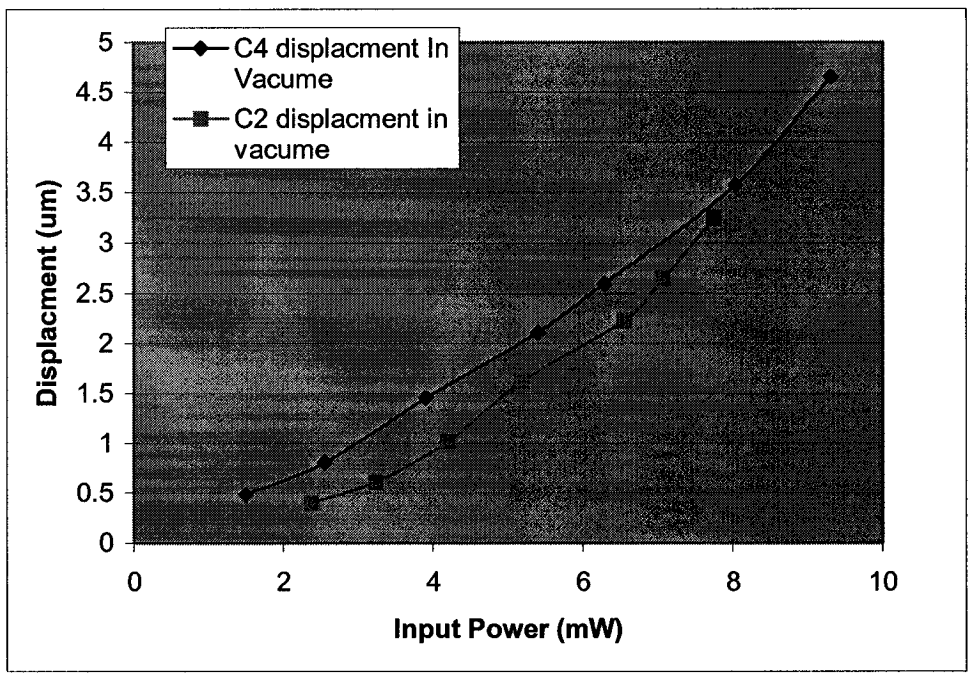

Figure 4.17 Measured vertical displacement of C4 and C2 with respect to input power

The central cantilever beam of C3 was found stick down to the substrate. So no more tests were carried out on this device. The geometry of this cantilever beam is 113μm by 5μm. Figure 4.16 shows the stiction situation.

4.2.3.1 Actuation Force Generated by Microbridge

Actuation force produced by the actuator is an important parameter for actuators. But it is very hard to measure the actuation force directly. In the device C2 and C4, a central cantilever arm is placed at the middle of the microbridge actuator. By measuring the vertical displacement of the microbridge (central cantilever arm), the actuation force generated by actuator is easily calculated by the equation.

$$F=KX \quad \text{where } K=\frac{EWH^3}{4L^3} \text{ [56]}$$

K is spring constant of cantilever beam, W is the width of the cantilever beam, H is the thickness and L is the length. E is Young' Modulus of polysilicon, and is chosen as 160GP. Figure 4.18 shows the curve of actuation force against power input of the device C4 and C2.

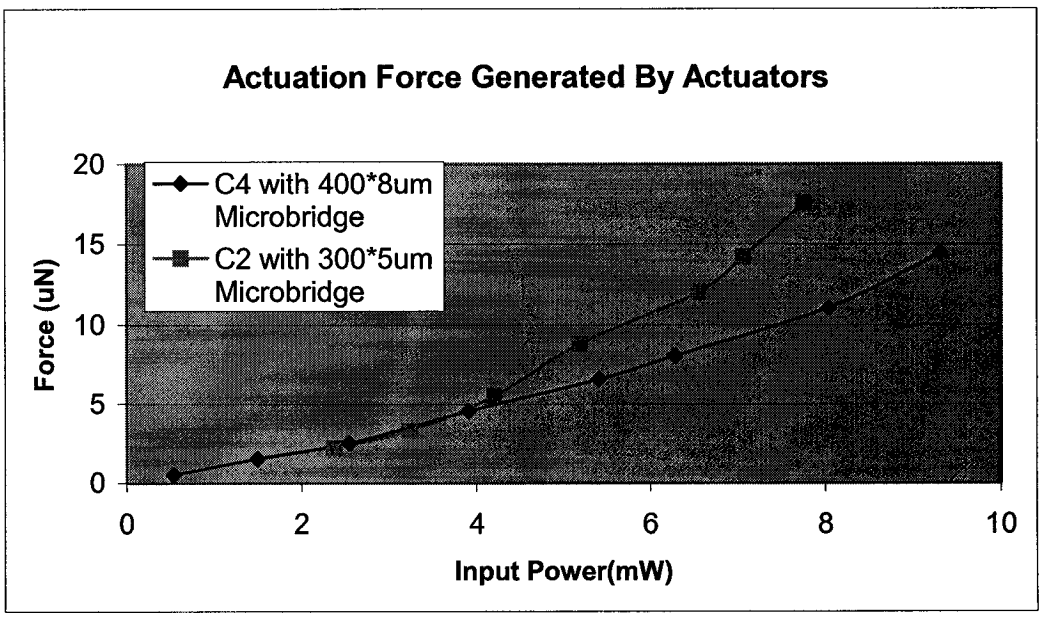

Figure 4.18 Actuation force generated by microbridge actuator versus power input

Even though C4 shows more vertical deflection than C2, we still find that higher forces generated by the shorter and thinner actuator in C2. The reason is that C2 has a

shorter central cantilever arm of 50 μm by 5μm. The spring constant of this beam is about two times of C4 's central cantilever arm. Therefore, to reach the same deflection, more upward forces are needed for device C2.

4.2.3 .2 Metal Layer Deformation

In device C4, a micromirror plane was placed at the free end of the central cantilever arm to reflect light. A 25 μm by 25μm poly2 square covered by metal layer is employed in device C4. During the test we found that the golden metal layer was buckled at certain input condition. The SEM picture below shows this deformation when 4.5V, 2.07 mA input is applied. The ANSYS simulation result shows that the micromirror 's temperature is 844.9K at this condition. Even through this temperature was far lower than the melting point of gold, which is about 1337K, it still causes the gold mirror to deform. The temperature distribution from ANSYS simulation is illustrated in Figure 4.20. To maintain the good reflectivity of the mirror surface, the operation voltage of device C4 should not over 4.5V.

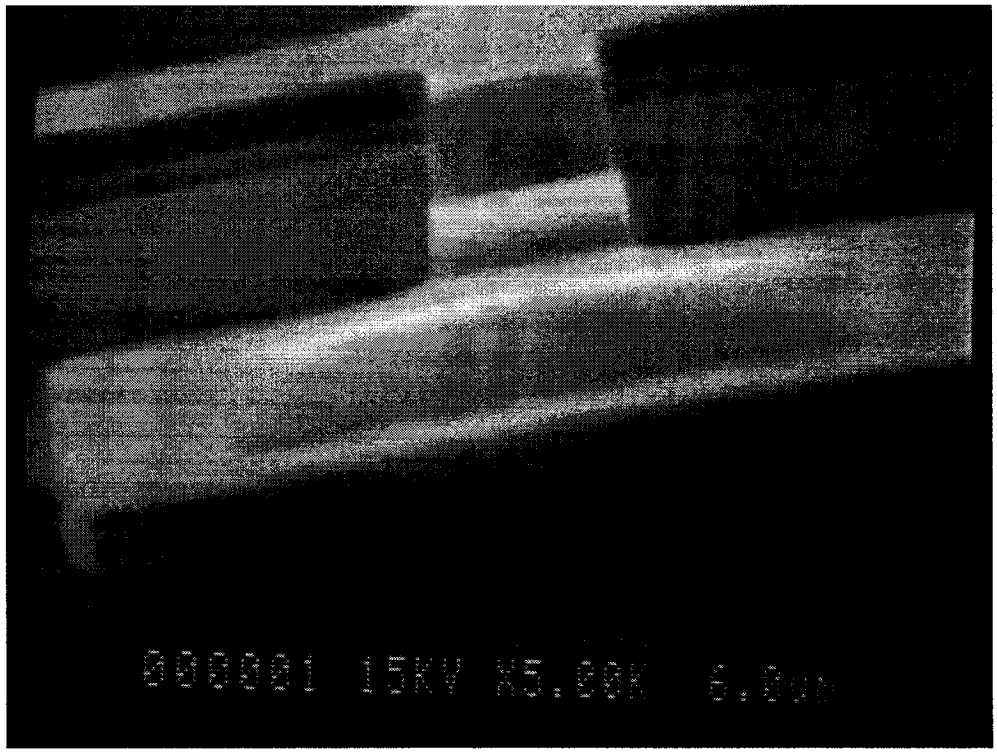

Figure 4.19 The metal layer in device C4 buckled at 4.5V, 2.07 mA input

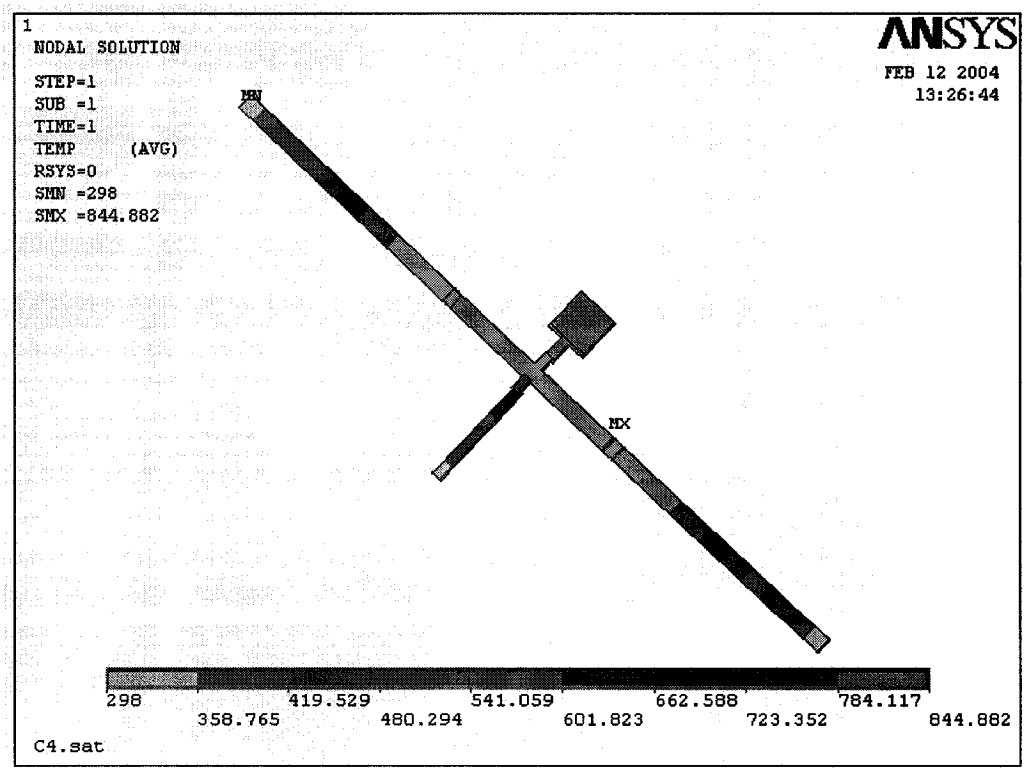

Figure 4.20 Temperature distribution of C4 generated by ANSYS simulation

4.2.4 Device in Family D

In family D, a Poly2 central arm covered by metal layer takes the place of the simple Poly2 cantilever arm at the middle of the bridge structure. This stress induced composite beam would bring more initial upward curvature for the microbridge actuator. Figure 4.21 shows the SEM picture of the device D1.

Only one device in family D, device D1, was tested by SEM with 2K magnification. It should be noted that in the unheated state the central part of the beam curved up with a deflection of about 6.8 μm above the poly0 support. Displacement means the deflection of the middle of the bridge in the upward direction with respect to the unheated state. The SEM picture in Figure 4.21 (b) was taken when 5.04V, 3.79mA input power was applied. The measured static state resistance of D1 was 948Ω. Figure 4.22 depicts measurement result of vertical displacement against the input power. The device was observed 0.4 μm out of plane deflection at 1.56mW input power. At 19mW input, the device obtained the maximum vertical deflection of 8.1μm. The measurement was stopped at 4.01V to avoid high temperate. Device B2 and D1 have the same geometry of microbridge actuator. However, D1 has a composite central arm connected at the middle of the microbridge to obtain more initial curvature. The vertical displacement of these two devices is compared in the Figure 4.23. The curves show that the existence of central cantilever arm reduces about 2 to 3 times of the vertical deflection of actuator. The minimum power to drive the device was 0.4 mW for B2 and 1.55 mW for D1 .Both of the devices were observed 0.5 μm vertical displacement under the minimum power.

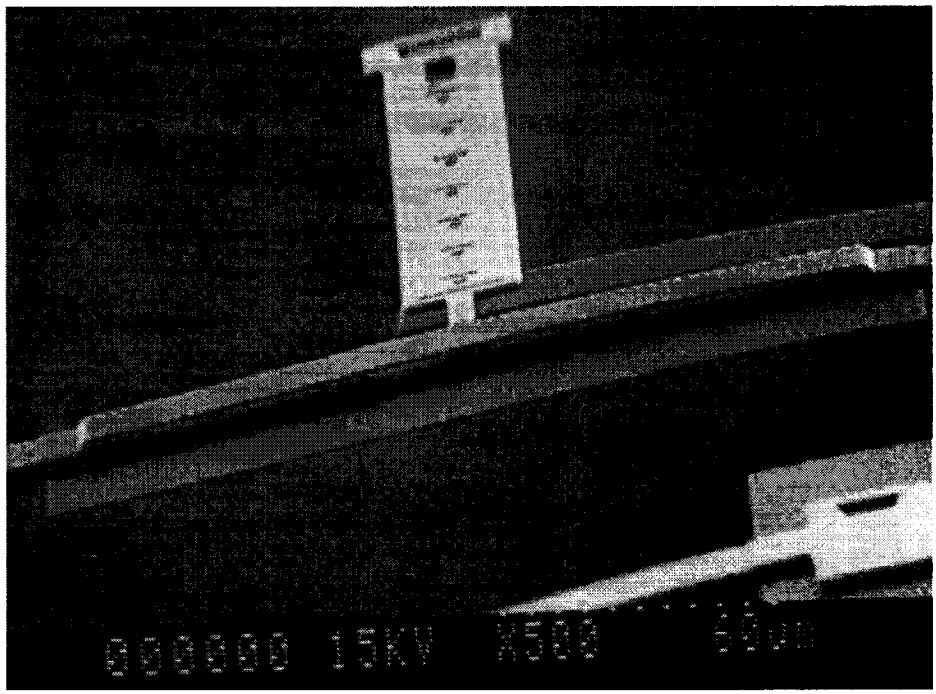

(a)

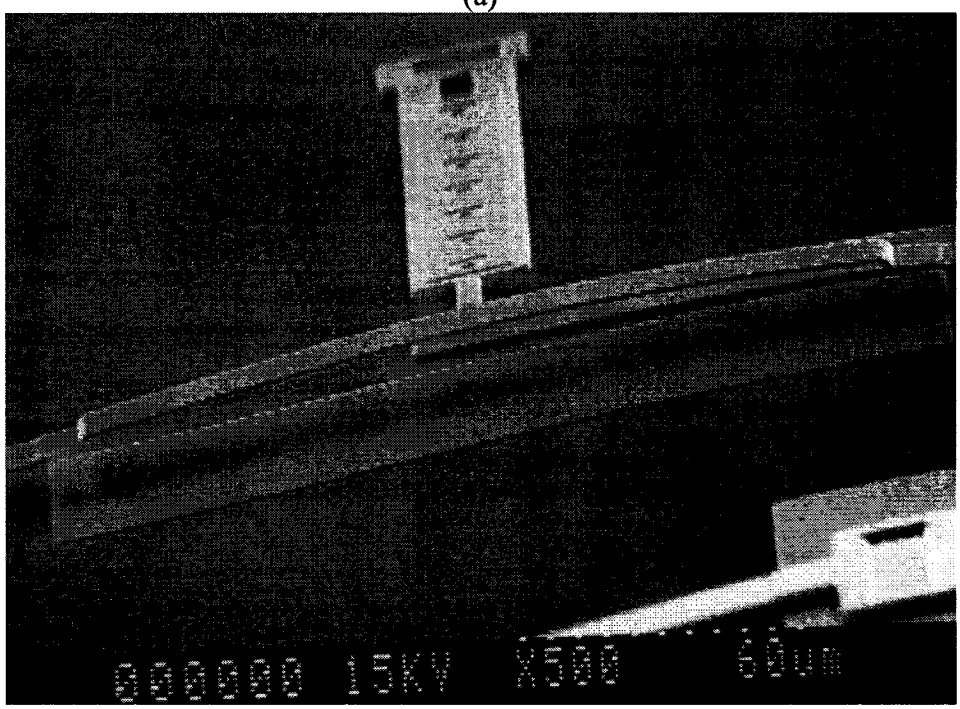

(b)

Figure 4.21 SEM picture of device D1(a) Device in unheated condition (b) Device left up after 5V 3.79mA input power applied

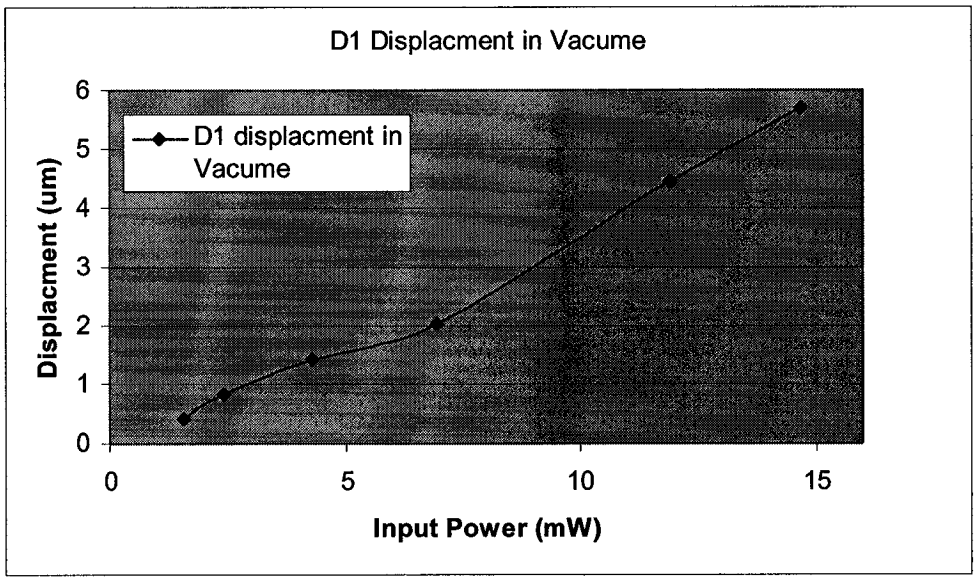

Figure 4.22 Vertical displacement with respect to input power of device D1 in vacuum ambient

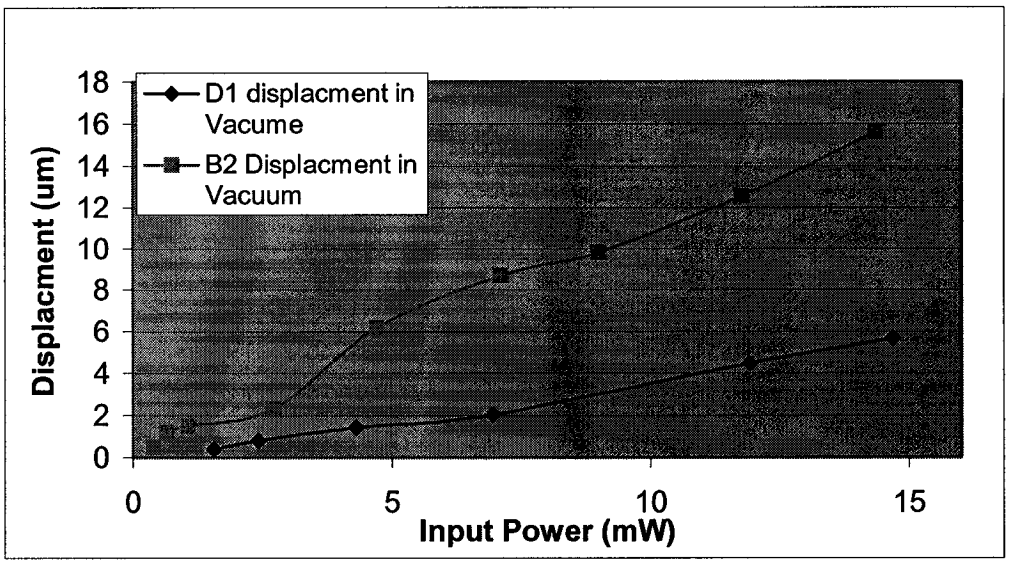

Figure 4.23 Vertical displacement of B2 compare with D1 respect to input power in vacuum ambient

4.2.5 Device in Family E

The designs in family E convert the in-plane displacement to out-of-plane motion. The stress induced composite central arm is implanted into this design. In order to provide enough force to rise up the composite arm, double V shaped structures are utilized. They are parallel to each other. Figure 2.13 shows the layout design of device E1.

Only one device, device E1 was tested. The measurement of device E1 was conducted in air by optical microscope. Figure 4.24 shows the curve of vertical displacement versus input power. Here, displacement means the deflection of the free end of the composite beam. The measured resistance of E1 was 717Ω. And the observed maximum displacement is 12 μm at 73.5mW (9.8 V 7.5 mA)input.

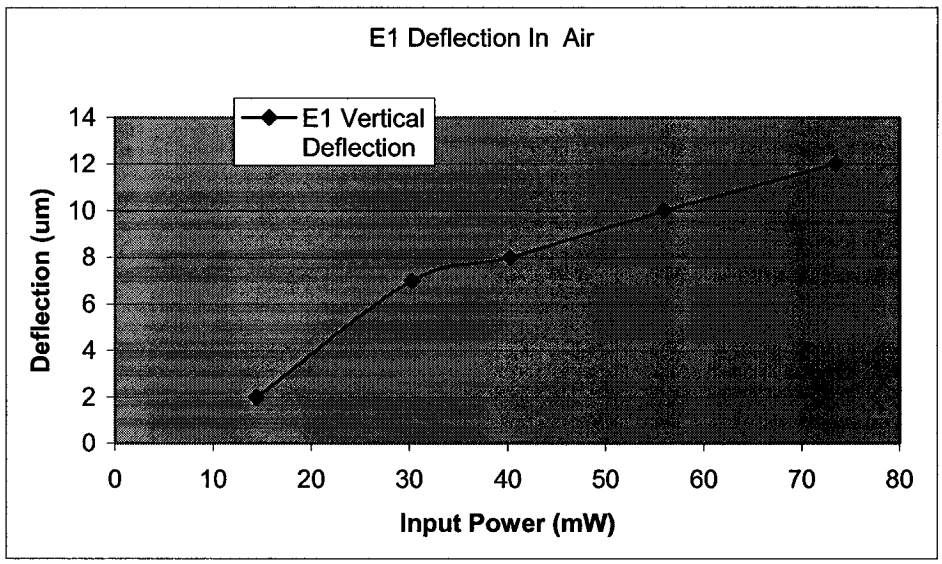

Figure 4.24 Device E1 vertical deflection versus input power

One of the devices E1 was found stick down to the substrate after being released. Figure 4.25 shows this situation. The junction of V-shaped actuator and composite central arm was stick down to the substrate. From the picture we could find that there was a gap between the composite arm and the substrate; but this gap diminished along with the

connection beam from the composite arm to the V-shaped actuator. Close to device E1, there is a composite arm curved up from the substrate. It is a test structure that has the exactly same geometry as E1 's central composite arm. This composite arm demonstrated a 3.75 μm curl-up from substrate after releasing. Therefore, it is the V-shape actuator that cause the stiction .

In order to avoid stiction and improve the yield, in the future design, a dimple layer should be employed underneath the poly1 V-shaped actuator. In addition, a longer and wider composite central arm would also help by providing more stress-induced curling.

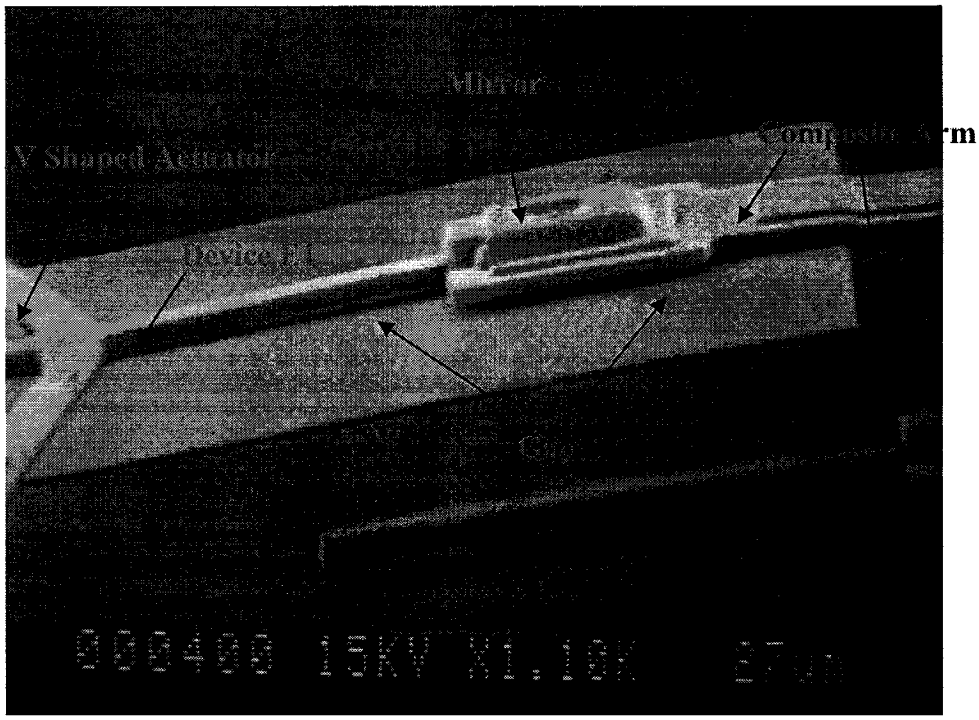

Figure 4.25 SEM picture of E1 which is found stick to the substrate

In vacuum, we tried to applied higher power to drive the actuator overcome capillary force and move up. But after applying 6.67V 7.8mA power, one of the legs was broken by high temperature. The actuator still couldn't be lift up from the substrate. The destroyed structure is shown in Figure 4.26.

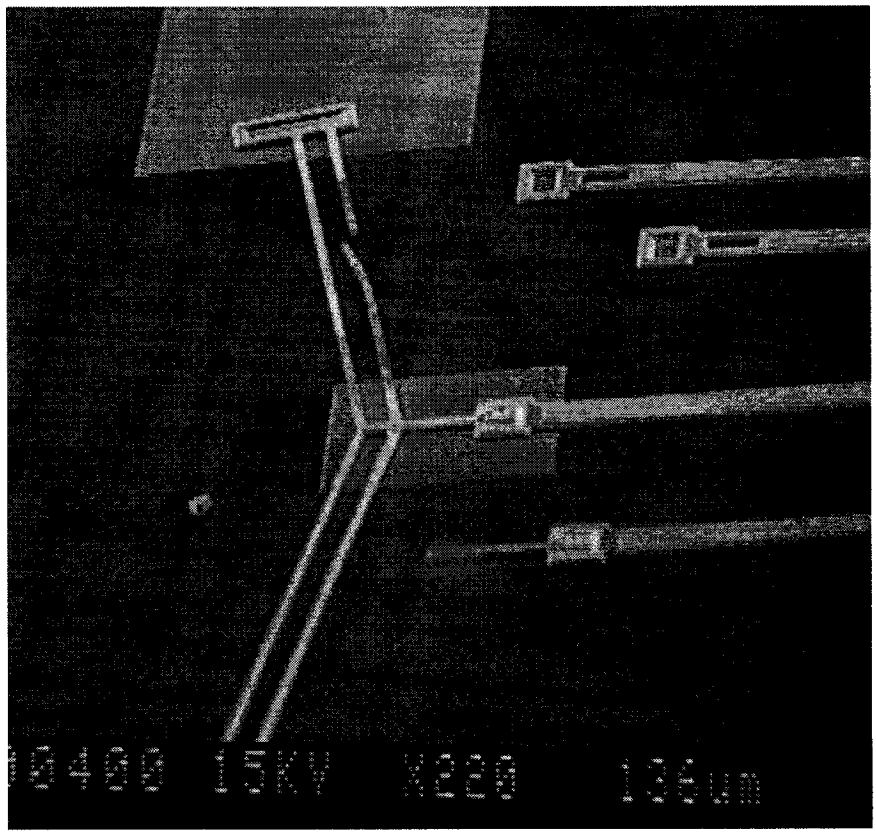

Figure 4.26 SEM picture of E1, one of the side arm melted after 67V 7.8mA power applied.

4.3 The Measurement of Operational Frequency

The operational frequency is an important criterion in actuator applications such as micro positioning and switching and is the motivation of the characterization described here. Two time periods decide the operational frequency of the devices. One is device raise time, in which the device moves up and reaches maximum vertical deflection at a given input power; the other is reset time that the raised device falls down to the static state position after the power off.

The raise time and reset time can be determined by applying a Joule heating voltage pulse and measure the deflection amplitude for different pulse and pause widths. To obtain the response to a positive edge (switching on the power), a pulsed input signal,

where the pulse time is much shorter than the pause time, is applied to the actuator and the corresponding deflection amplitude is measured. Gradually increasing the pulse width increases the deflection amplitude until the maximum deflection is reached as illustrated in Figure 4.27. The maximum deflection has the same magnitude as the static deflection obtained by applying a dc input of the same power. Similarly, using an input signal, where the pause time is much shorter than the pulse time, the deflection response for a negative edge (switching off the power) is obtained. The pause width is increased gradually and the corresponding deflection amplitude is measured. To facilitate deflection measurements on an SEM screen, the frequency of the pulse generator is set at 30 Hz , which is half of scanning frequency of the SEM (60 Hz) to obtain a stationary picture.

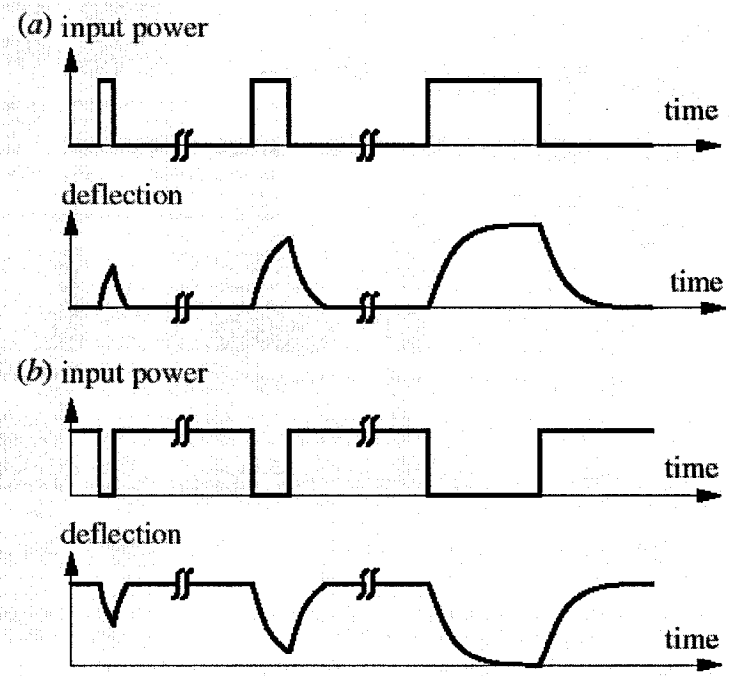

Figure 4.27 Pulsed input signal and deflection response for measurement of deflection response (*a*) to a positive edge, (*b*) to a negative edge [57].

With this method, device B2 had been tested, and deflection amplitude versus elapsed time plots was obtained. It is shown in Figure 4.28. The input power was 4.5 mw during the pulse. (Voltage V=2 Vcurrent I =2.25 mA). The raise time of device B2 was 4.8ms and reset time was 4.9 ms. The highest operational frequency, at which the full defection was reached was 103Hz.

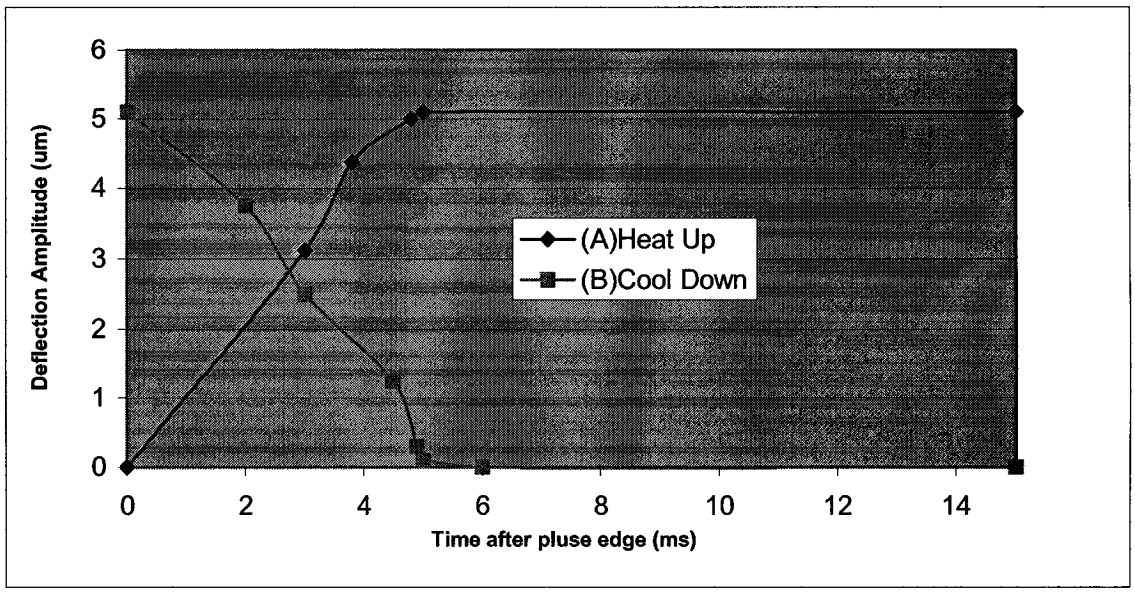

Figure 4.28 Measure deflection versus elapsed time after (A) positive edge and (B) negative edge of device B2. Input power is 4.5mW.

4.3.1 Thermal Frequency And Operational Frequency

In chapter 2 thermal time constant (τ) of self-heated resistance was discussed. The thermal time constant describes the rate at which the structure reaches its static state temperature distribution with a given input power. Assume that a time period of 5τ is necessary to heat up the structure and to cool down again. Then the thermal frequency can be derived from the thermal constant.

Some researchers use the thermal time constant and thermal frequency to predict device operational frequency.[57] They based on an assumption that the actuator achieves the maximum deflection, when the static state temperature is reached. However, it did not applicable for all of our devices. Table 4.9 gives the measured raise time, reset time, and operational frequencies of some devices. They are compared with the thermal frequency that was calculated from thermal time constant. For the devices in family B, thermal frequency shows reasonable agreement with the measured operational frequency. The operational frequency of device B3 was 84.7Hz, and the thermal frequency was 94.3 Hz. Device B2 has 100 Hz thermal frequency, and 103.1Hz operational frequency. However, for the devices in family C and family D, large disagreement exists between theoretical calculation and measurement result. Experimental result of C2 shows that the operational frequency was 86.2Hz , but the thermal frequency was 507.6Hz. These errors may come from the structure design. Device in family B is a simple bridge structure, but devices in family C and D have a central arm connected at the middle of bridge. These central arms affect the performance of the actuator.

Device	B2	B3	C2	C4	D1
Voltage Applied(V)	2	2.2	3.4	2.84	3
Bridge Length (um)	500	500	300	400	508
Bridge Width (um)	20	30	5	8	20
Measured Rise Up Time (ms)	4.8	5	6	6.6	6.5
Measured Reset Time (ms)	4.9	6.8	5.6	6.2	5
Calculated Thermal Time Constant(ms)	0.997	1.06	0.197	0.44	0.7785
Measured Operational Frequency(Hz)	103.1	84.7	86.2	78.1	86.9
Calculated Thermal Frequency(Hz)	100.3009	94.339623	507.6142	227.2727	128.4522

Table 4.9 Measured operational frequency compare with thermal frequency

The elastic force generated by the central arm always turns to eliminate the deflection of the actuator. It affects the dynamic performance of the actuator, and extends the device response time. The thermal time constant could not successfully estimate the operational frequency for all the thermal actuator. In the future work, an accurate model to investigate the transient behaviors of the device in family C and D is expected.

4.4 The Measurement of Resonant Frequency

In this section, the measurement of device resonate frequency is reported. No theoretical modeling work has done till now.

For the resonance measurement we used frequencies significantly exceeding the operational frequency of the actuator, which means that the actuators could not cool off to the bulk temperature. Therefore, the input signal caused a static deflection upon which a vibration was superimposed. The actuator was driven with an ac input. The driving frequency was manually swept from 1kHz to 200kHz and then was decreased again. The vibration amplitude was measured with the SEM.

Although the frequency of the resonating beam is significantly higher than the refresh rate of the SEM screen, the minimum and maximum deflection can be clearly seen by the lines in the blurred image occurring on the SEM screen. This is due to the repetitive and reproducible character of the vibration. Thus, the deflection amplitude can be measured. This method is a very straightforward approach for measuring the movement without a great instrumental complexity as required by interference techniques [58].

Figure 4.29 shows an amplitude versus frequency plot for Device B2 with the following dimensions: length = 500 μm, width=20μm. The input voltage is 3 V Pk-Pk,

The resonant frequency is found to be 37.2 kHz, The static deflection of the beam is measured to be 3.2 μm.

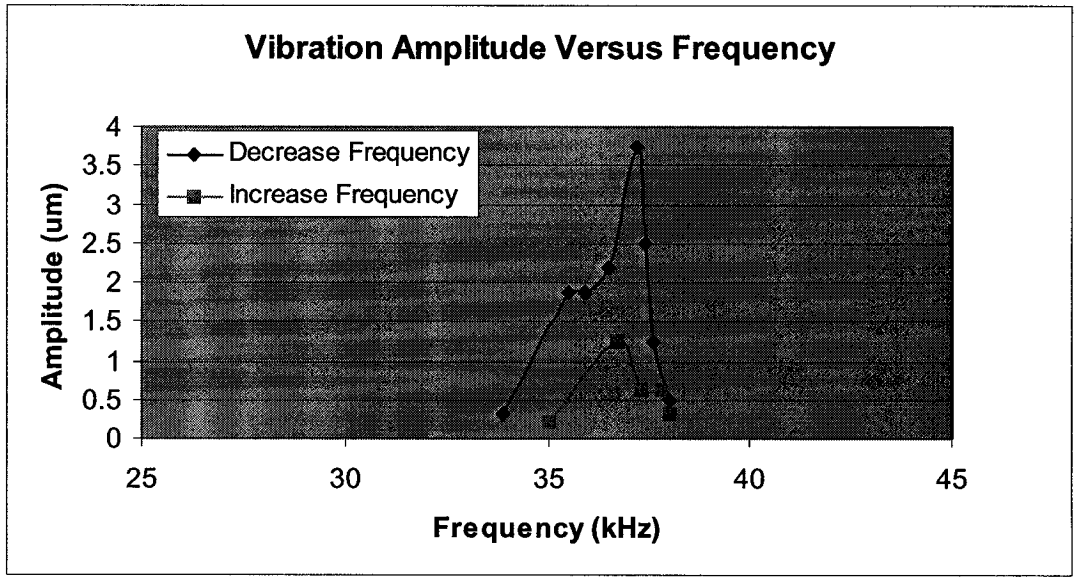

Figure 4 .29 The vibration amplitude values with respect to the frequency of device B2

The same test was carried out on devices B3,C4 and D1. The first observed resonated frequency was recorded and listed in the table below. Figure 4.30 shows the vibration of device B3 at 32.1 KHz and at 32.7KHz. Lower vibration amplitude was observed at 32.7KHz, which is higher than resonant frequency. The maximum amplitude was observed at the resonant frequency of 32.1 KHz.

Device	Applied Voltage Pk to Pk	The First Observed Resonate Frequency
B2	3V	37.2KHz
B3	2.2V	32.1Khz
C4	2.84V	39.4kHz
D1	3V	54.5KHz

Table 4.10 First observed resonate frequency

(a)

(b)

Figure 4.30 The vibration of device B3 (a) At 32.1KHz (resonate frequency) (b) At 32.7KHz

As has been mentioned, five sets of the out-of-plane thermal actuators have been realized and tested. The measurement results of the devices in each family are reported. The ANSYS simulation and theoretical model help to investigate the device performance in different ambient. In next chapter, the key findings and the conclusions will be summarized.

CHAPTER 5 CONCLUSIONS AND FUTURE WORK

5.1 Conclusions

The goal of this thesis was to design, fabricate and test an out-plane motion electro-thermal actuated MEMS actuator to fit a variety of different applicants such as adaptive optics, and optical switching. In this thesis, five sets of designs of electro-thermal actuators are prototyped using the MUMPs process technology. These families of designs are chosen specifically to explore a number of different parameters, including actuation scheme, structure geometry, and type of motion.

Critical to the use of thermal micro actuator in optical purpose applications is characterization of deflection, power consumption and frequency response. Devices in each set were tested. Test results indicate that the microbridge thermal actuators might be an attractive alternative to the more common electrostatic designs.

Intensive tests are performed on the devices in family B and C. SEM is employed to carry out accurate measurement of vertical deflection. Device B2 with total length of 500μm, and beams width of 20 μm, demonstrated 15.6 μm vertical displacement in vacuum ambient when 3.5 mA input current (4.1V voltage) applied. The vertical deflections of devices B1, B3, and B4 are tested and compared to each other to study how the geometry parameters affect the devices performance. The upward actuation force generated by the microbridge actuator is measured. The maximum value of 17.5 μN is measured from device C4 at 7.75 mW input. Devices performance in air condition is also investigated. In air, 3 to 6 times more power was needed for the same performance compare to theirs in vacuum.

Finite element simulation software, ANSYS 6.1, is used to analysis device deflection and temperature distribution in vacuum. Theoretical model discussed in chapter 2 was used to investigate the devices performance in air. Experimental results are compared with the analytical results, and a good agreement is achieved.

Frequency response of the devices was tested. The observed operational frequency of all devices does not exceed 103 Hz. The first observed resonated frequency of the devices B2, B3, C4 and D1 is reported.

Poly 0 permanent support and Poly1 temporary support are successfully implemented in our designs. These support structures not only help the microbidge to survive from the capillary forces during the release process, but also help to form the shape of the bridge structure, which ensure the actuator will raise up rather than buckle down to the substrate after thermal expansion. A microbridge with 792 μm in length and 20 μm in width is successfully fabricated, and realize the out-of plane motion.

Although almost all the designs seem to work as expected. Some manufacturing problems are observed with specific type of devices, such as device C3 and device B1. These observations are used to develop a set of guidelines outlining possible design strategies that could be used to improve the production yield of future designs. For example, the use of dimple layer under the Poly1 V-shape actuator to prevent stiction, or avoiding use of etching hole with the beams smaller than 500 μm * 20 μm to obtain a robust structure, are recommended.

5.2 Publication Related to This Work

"Thermally Actuated Piston Motion Optical Switch" Eleventh Canadian Semiconductor Technology Conference, 2003

5.3 Future Work

One of the goals for the next stage of investigations of thermal actuator are to design and implement more devices based on the structure of family B and family D. A mirror plane could implant to the new devices and the optical property of the mirror should be tested. Further investigations on theoretical analysis, simulation of the devices in family E and family D are expected.

Another focus for future work is in the area of device characterization. Although several tests have conducted to characterize the static behavior of MEMS device, none is carried out to figure out the device lifetime and repeatability, which are the important parameters in industry application. Thus, a new experimental setup would need to measure both the device lifetime and their repeatability.

A new characterization technique with higher accuracy for testing the device vertical deflection in air should be developed. And an accurate model to study the dynamic behavior of the devices is also expected.

References

[1] E.Lin Julianna "Design and Characterization of MEMS Micromirror Devices"

[2] G.E Moore, "Cramming More Components onto Integrated Circuits," Proceedings of the IEEE, Vol. 86, No.1 January 1998.

[3]J.M Rabaey," A historical Perspective," in Digital Integrated Circuits: A design Perspective, Prentice Hall Electronics And VLSI Series, Charles G. Sodini, Series Ed. New jersey: Prentice-Hall, pp.1-14

[4]H.C.Nathanson, W.E.Newell, R.Awickstrom, and J.Rdavis, Jr., "The Resonant Gate Transistor," IEEE Transactions on Electron Devices, Vol .ED-14,No.3, pp.117-133,march 1967.

[5] M.A.Michalicek ,"Introduction to Microelectonmechincal system: A Brief history and overview of Mems Technology and Applications," in MEMS short course, Air force Research laboratory, Space Vehicles Directorate, Kirtland AFB ,New Mexico , 18 may 2000

[6] K.E.Bean , " Anisotropic Etching of Silicon," IEEE Transactions on Electron Devices, Vol. ED-25 ,No.10 pp.1185, October 1978.

[7]A.C.M Gieles, And GH..J. Somers," Miniature Pressure Transducers with silicon Diaphragm," Phillips Tech.Rev., Vol. 33,p,1973.

[8] W.D Frobenius,A.C Sanderson, and H.C.Nathanson," A microminiature Solid Stat Capacitive Blood Pressure Transducer with improved sensitivity ,"IEEE Tans. Biomed .Eng, Vol BME-20,p.312,1973.

[9]S.k.Calrk and K.D wise," Pressure Sensitivity in Anisotropically Etched Thin Diaphragm Pressure Sensors" IEEE Trans. Électron Devices , Vol .ED-26 , p.1887,1979.

[10] C. Beatty, "A chronology of Thermal Ink-Jet Structures, " Tech. Digest 1996 Solid State Sensor and Actuator Workshop ,pp,200-2004,1996

[11] Special Issue on Ink Jet Printing , IBM j. Res. Develop., Vol 21,1977.

[12] J .B. Angell, S,C. Terry , and P.W.Barth, " Silicon Micromechanical Devices," Scientific American Journal, Vol 248, pp 44-55. April 1983.

[13] J.S. Harper and P. F. Heidrich, "High Density Multichannel Optical Waveguides with Integrated Couplers," Wave Electron Vol. 2,p. 396.1976.

[14] J.T.Boyd and S.Sriram, "Optical Coupling from Fibers to channel waveguides formed on silicon," Applied Optics, Vol. 17,p. 895,1978.

[15] K. E. Peterson, "Silicon as a mechanical material," in Proc. IEEE, 70 (982), pp. 420—457.

[16] R. T. Howe and R. S. Muller, "Polycrystalline silicon micromechanical beams," in Spring meeting of the electrochemical society, Montreal, Canada, Extended abstracts 82-1. May 9-14, 1982.

[17] R. T. Howe and R. S. Muller, "Resonant microbridge vapor sensor," in IEEE Trans. Electr. Devices, ED-33, pp. 499—507. 1986.

[18] Richard S. Muller, "Mems: Quo vadis in century xxi?," Microelectronic engineering, vol. 53, pp. 47—54, 2000.

[19]Meng Fai Tung An Introduction to MEMS Optical Switches

[20] Husain, A. 2001. MEMS-Based Photonic Switching in Communications Networks. In: *Optical Fiber Communication Conference and Exhibit.* Vol. 3.

[21] Barthel, J. and Chuh, T. 2001. Optical Switches Enable Dynamic Optical Add/Drop Modules. *WDM Solutions.* Vol. 3, No. 8: 93-96.

[22] Hecht, J. 2001. Many Approaches Taken for All-Optical Switching. *Laser Focus World.* Vol. 37, No. 8: 125-130.

[23] http://cfao.ucolick.org/ao/why.php

[24] Marxer, C., Thio, C., Grétillat, M., de Rooji, F., Bättig, R., Anthamatten, O., Valk, B. and Vogel, P. 1997. Vertical Mirrors Fabricated by Deep Reactive Ion Etching for Fiber-Optic Switching Applications. Journal of Microelectromechanical Systems. Vol. 6, No. 3: 277-285.

[25] L.J Hornbeck, 128*128 deformable mirror device, IEEE Tans. Electron Devices ED-30 (1983) 539-545. sadf

[26] L.S fan. Y.C Tai, R.S Muller, IC-processed micromotors, IEDM, 1988, pp.666-669.

[27] W.C.Tang ,C.T-C,Nguyen, R,T.Howe, Laterally driven polysillicon resonant microstructure, Sensors and Actuators A 20(1989) 25-32.

[28] Brown, M. P., and Austin, K., Appl. Phys. Letters 65, 2503-2504 (1994).

[29] J. M. Gere and S. P. Timoshenko, *Mechanics of Materials,* 3rd ed.
Boston, MA: PWS-Kent, 1990.

[30] Y. B. Gianchandani and K. Najafi, "A bulk silicon dissolved wafer process for microelectromechanical devices," *IEEE J. Microelectromech. Syst.,* vol. 1, no. 2, pp. 77–85, 1992.

[31] T. Akiyama and H. Fujita, "A quantitative analysis of scratch drive actuator using buckling motion", *Proc. 8th IEEE International MEMS Workshop*, pp. 310-315, Amsterdam, Netherlands,
January 29- February 2, 1995.

[32] Xiaoning Jiang Vijay K. Varadan and Vasundara V. Varadan, Microstereolithography andother fabrication technologies for 3D MEMS, John Wiley and Sons. Ltd, Ba.ns Lane, Chichester West Sussex, PO19 1UD, England, 2001.

[33] Smith, C. D., and Jones, E. F., "Load-Cycling in Cubic Press" in Shock Compression in Condensed Matter-1997, edited by S. C. Schmidt et al., AIP Conference Proceedings 429, New York: American Institute of Physics, 1998, pp. 651-654.

[34] PolyMUMPs Design Handbook a MUMPs® process Revision 9.0 by David Koester, Allen Cowen, Ramaswamy Mahadevan, Mark Stonefield, and Busbee Hardy MEMSCAP

[35] W.D.Cowan and V.M.Bright, "Thermally Actuated Piston Micromirror Arrays." Proc. SPIE, Vol.3131, pp. 260- 271, 1997.

[36] Guckel H, Sniegowski J J, Christenson T R, Mohney S and Kelly T F 1989 Fabrication of micromechanical devices from Polysilicon films with smooth surfaces Sensors Actuators 20 117–22

[37] Mastrangelo C H and Hsu C H 1993 Mechanical stability and adhesion of microstructures under capillary forces—part I: basic theory J. Microelectromech. Syst. 2 33–43

[38] N. Tas, T. Sonnenberg, H. Jansen, R. Legtenberg, and M. Elwenspoek, "Stiction in Surface Micromachining," Journal of Micromechanics and Microengineering, Vol. 6, pp. 385-397, 1996.

[39] Mastrangelo C H and Hsu C H 1993 Mechanical stability and adhesion of microstructures under capillary forces—part II: experiments J. Microelectromech. Syst. 2

44–55 Int. Conf. on Solid-State Sensors and Actuators (Transducers '95) (Stockholm, 1995) pp 214–7

[40] Gogoi B P and Mastrangelo C H 1995 Post-processing release of microstructures by electromagnetic pulses 8th Int. Conf. on Solid-State Sensors and Actuators (Transducers '95) (Stockholm, 1995) pp 214–7

[41] Senturia, Steohen D., "Microfabricated Structures for the Measurement of Mechanical Properties and Adhesion of Thin Films," Transducers '87 Rec. of the 4th Int. Conf. on Solid-State Sensors and Actuators, 1987, pp 11-16.

[42] Que L, Park J-S and Gianchandani Y B 2001 Bent-beam electrothermal actuators: Part I. Single beam and cascaded devices IEEE/ASME J. Microelectromech. Syst. 10 247-54

[43] Qing-An Huang, N.K.S. Lee "Analysis and design of polysilicon thermal flexure actuator" J Micromech Microeng 9 (1999) 64-70

[44] Qing-An Huang, N.K.S. Lee "Numerical simulation of a polysilicon thermal flexure actuator" Microsystem technologies 8 (2002) 17-21

[45] L. Lin and M. Chiao, "Electro, thermal and elastic characterization of suspended micro beams," Microelectron. J., vol. 29, no. 4–5, pp. 269–276, 1998.

[46] Dong Yan "Mechanical Design and Modeling of MEMS Thermal Actuators for RF Applications" University of Waterloo

[47]L,lin and M.Chiao, "Electrothermal responses of lineshape microstructures," Sens. Actuators,vol.A55,pp.35-41,1996.

[48]M.Chiao and L,lin" Self-buckling of Micromachined Beams Under Resistive Heating" J of Micro-electromechanical systems, Vol 9,No1 March 2000

[49] Liwei Lin,Shiao-Hong L "Vertically driven microactuaors by eletrothermal buckling effects" Sensors and Actuators A71(1998) 35-39

[50] Y.C Fung, Foundations of Solid Mechanics. Englewood Cliffs , NJ: Prentice-Hall , 1965.

[51] Stephen D.Senturia "Microsystem Design" Massachusetts Institute of Technology

[52] Dr. Martin Marz, Paul Nance "Thermal Modeling of Power-electronic Systems" Infineon Technologies AG, Munich

[53] http://extra.ivf.se/ngl/A-WireBonding/ChapterA2.htm#A2.1

[54] http://www.unl.edu/CMRAcfem/semoptic.htm

[55] MEMS pro User Guide

[56] Stephen D.Senturia "Microsystem Design "

[57] Time constant and lateral resonances of thermal vertical bimorph actuators H Sehr, I S Tomlin, B Huang, S P Beeby, A G R Evans, A Brunnschweiler, G J Ensell, C G J Schabmueller and T E G Niblock 2002 J. Micromech. Microeng. 12 410-413

[58] Hart MR,Conant R A,Lau K Y and Muller R S 2000 J.Microelectromech. Syst.9 409-18

APPENDIX

A Feed Hole Problem In The Wire Bonding

Ball bond and wedge bond are two basic wire bond forms. (Figure A.1) Wedge bond is named by the shape of its bonding tool. WESTBOND 7476E used in this experiment is a kind of wedge bonder. First, the wire is fed at an angle usually 30-60° from the horizontal bonding surface through a hole in the back of a bonding wedge. By descending the wedge onto the IC bond pad, the wire is pinned against the pad surface and a bond is performed. Next, the wedge rises and executes a move to create a desired loop shape. At the second bond location, the wedge descends and makes a second bond. During the loop formation, the movement of the axis of the bonding wedge feed hole must be aligned with the center line of the first bond so that the wire can be fed freely through the hole in the wedge. (See figure A.2)

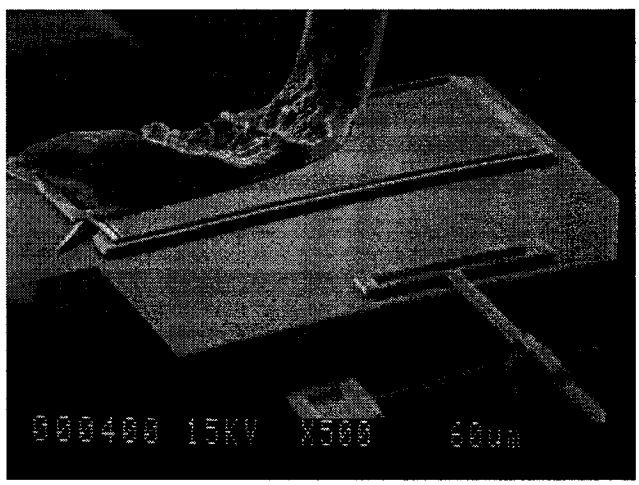

Figure A.1 Wedge Bond

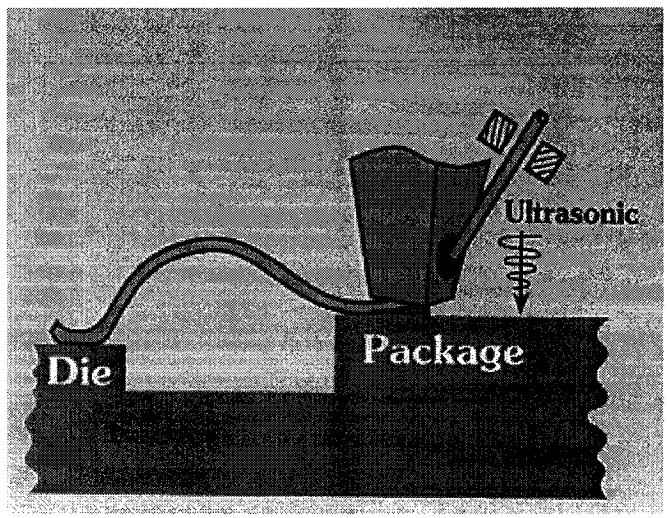

FigureA.2. Ultrasonic wedge bonding

The feedhole on the bonding wedge is likely the most critical aspect of the wedge configuration. The feedhole has the responsibility of guiding the wire accurately to the center of the bond foot. It plays such a critical role that it can also be the cause of many performance problems. These problems include poor wire feeding, poor looping, wire damage, poor wire termination and difficulty threading the wire.

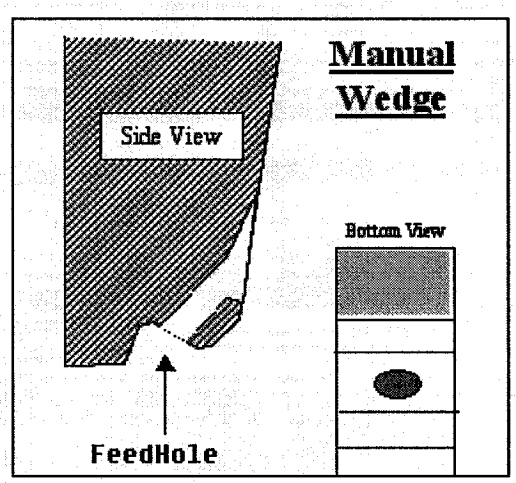

Figure A.3Feedhold on the bonding wedge.

Once, when we operated the wire bounder, we find that aluminum wire lost, and it was very hard to put the wire back into the feedhole again. Inspecting the bounding wedge by the microscope, we found the feed hold was block by a small part of aluminum wire. Then we took following procedure to clean the bonding wedge.

Step (1) - Load the bounding wedge in a tool tray with point of wedge up. Mix cleaning solution using water and sodium hydroxide. Mix five parts water to one part sodium hydroxide.

Step (2) - Place tool tray in 400ml beaker with enough Sodium Hydroxide cleaning solution to cover all tools completely. Place the beaker into the ultrasonic cleaner for approximately three to five minutes.

Step (3) - Transfer tool tray from cleaning solution beaker to 400ml beaker of hot water. Place beaker in ultrasonic cleaner for three to five minutes. Repeat this procedure with fresh hot water.

Step (4) - Complete the cleaning sequence with an alcohol rinse. Submerge the tool tray two or times in alcohol solution and then blow-dry with clean dry air.

The picture blow compares the bonding wedge before and after the cleaning process.

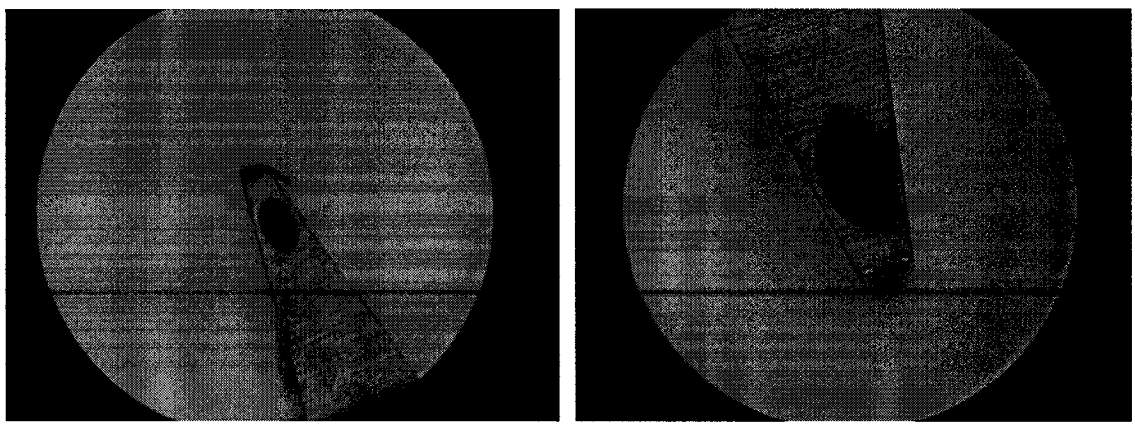

Figure A.4 Bonding wedge before and after cleaning process

B The Measurement Of The Raise Up Time In Air

To test the device response time in air, a direct touching measurement was carried out, and IC probe station was used in this measurement. The experimental setup is shown in the figure below. Three probes were employed in this measurement. Probe 1,and Prob2 touched the electoral pad of the device. The input excitation signal generated by the function generator was connected to these probes and drove the device. The third probe was suspend above the device, and did not touch the structure at static state. Probe 3 was connected to the channel 1 of the digital oscilloscope together with probe 1,which was coupled to the ground. When the device was heated and lift up, it would touch with probe 3. The oscilloscope would record a pulse signal after each touching. The signal generated by the function generator was sent to the digital oscilloscope through channel 2. Digital oscilloscope compares the signal from the channel 1 and channel 2. The time delay of this two signal was the raise time of the actuator. To avoid probe3 broke the actuator structure during the test, a probe with very fine and flexible tip was used.

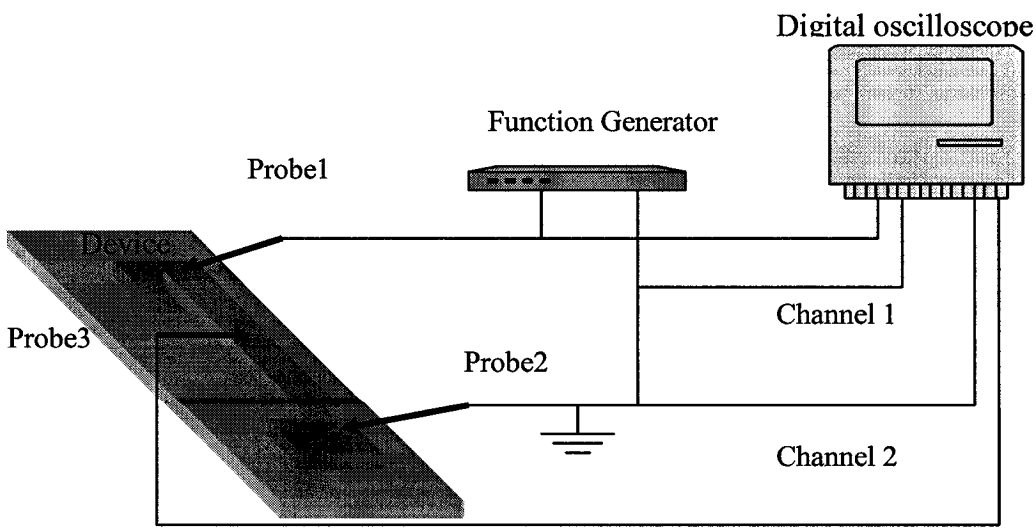

Figure A.5 The experimental setup of measuring device raise time in the air.

Device E1 was tested by this method. When 1Hz ,4.4 V Pk to Pk input signal was applied ,1.4ms time delay was observed .The Figure A.6 below shows the wave form captured by oscilloscope. No more devices were tested with this method because of two main drawback was founded during the test.

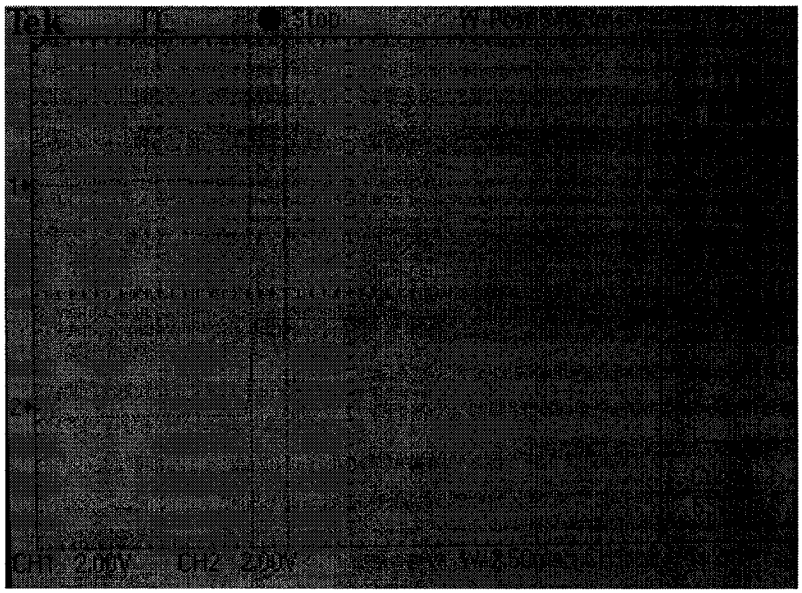

Figure A.6 The Digital oscilloscope display of device E1 , When 1Hz 4.4V Pk-Pk input signal applied ,1.4 ms time delay was observed.

1. The distance between probe 3 and device is very hard to be set accurately by the control knob on the probe. A poor connection between the probe3 and the micro actuator always happens. Serious noise of the input signal was founded. This comes from the vibration when the tip of the probe touches with the actuator. Figure A.7 shows the noise observed when 5v 10Hz input signal applied.

2. With this method only the raise time can be measured, the reset time of the device cannot be characterized.

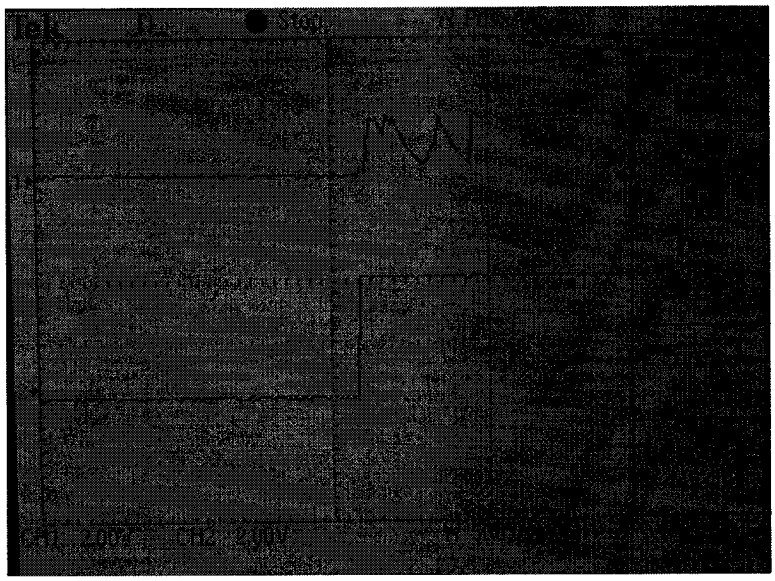

Figure A.7 The Digital oscilloscope display of device E1 , Noise was observed when10Hz 5V Pk-Pk input signal applied.